INTERFACE BROADENING AND RADIATION ENHANCED DIFFUSION DURING SPUTTER DEPTH PROFILING

by

George Paul Chambers III

Dissertation submitted to the Faculty of the Graduate School
of the University of Maryland in partial fulfillment
of the requirements for the degree of
Doctor of Philosophy
1988

Advisory Committee:

Professor Marvin L. Roush
Dr. Joseph Fine
Dr. Denes Marton
Professor Joseph Silverman
Professor James W. Gentry

ABSTRACT

Title of Dissertation: Interface Broadening and Radiation Enhanced Diffusion During Sputter Depth Profiling

George Paul Chambers, Doctor of Philosophy, 1988

Dissertation directed by: Dr. Marvin Roush
Chairman, Department of Chemical and Nuclear Engineering
Dr. Joseph Fine
Surface Science Division
National Bureau of Standards

The process of ion bombardment of solids has been investigated using Monte Carlo Computer Code simulation in conjunction with ultra-high vacuum experimental techniques. The computer code EVOLVE has been used to study the shape of the resultant collision cascade as well as the origins of sputtered particles while experimental studies of interface regions have been performed to elucidate the physical processes occuring during sputtering.

The EVOLVE code models the target as an amorphous multicomponent semi-infinite solid. The target composition during ion bombardment is simulated. The study concludes that recoil activity grows in size and tends to move away from the target surface with increasing time. It is further concluded that the majority of sputtered atoms origiate from early generations and are produced from sites near the entry point of the bombarding ion.

Low energy noble gas ion bombardment of thin-film Cr/Ni multilayered structures has been performed in conjunction with Auger electron spectroscopy under UHV conditions. An accurate, reliable, and systematic parameterization of the interface region between metallic layers is presented. It is concluded from this study that the extent of the distortion of the interface region due to ion induced broadening is dependent not only on the material system used but on the experimental conditions employed as well.

Lastly, radiation enhanced diffusion (RED) has been studied using Ag/Ni thin-film multilayered structures. A physical mathematical model of the radiation broadened Ag layer, capable of successfully deconvoluting the contributions to interface broadening due to RED from those due to cascade mixing and microstructure development, is presented and shown to be an accurate characterization of the interface region. It is concluded from the application of this model that RED can contribute substantially to interface broadening in multicomponent systems with low activation energies of diffusion. It is further concluded from this study that elevated temperatures, sustained during the depth profiling process, can cause the effects of RED to subside dramatically. This phenomenon is most probably due to the dispersion of complex defects responsible for the RED process.

To my parents,

Gus and Margaret

ACKNOWLEDGEMENT

Completion of the requirements for the degree of Doctor of Philosophy represents an important milestone in the author's life. This goal has been achieved with the help and guidance of a number of people with whom the author has been fortunate to associate.

The author wishes to express his sincere gratitude to Dr. Joseph Fine of the National Bureau of Standards for his patient guidance in the experimental aspects presented in this thesis and for the many illuminating discussions on the effects of ion bombardment. Dr. Fine has consistently provided expert direction for the various projects described in this work. In addition, Dr. Fine has made financial support available to the author through the National Bureau of Standards. The author is extremely grateful for the tremendous concern and support of Dr. Fine.

The author wishes to express deep appreciation to Dr. Marvin Roush for his encouragement, concern and guidance. Dr. Roush, together with Dr. Farhad Davarya and Dr. Tim Andreadis, guided the author in the computer code simulation studies presented in this thesis. Moreover, despite his considerable duties as departmant chairman, Dr. Roush has always been available for counsel, advice, and guidance throughout the author's graduate program and research career. The author is

indeed grateful for the many opportunities and financial support consistently made available to him by Dr. Roush.

The author wishes to acknowledge, with pleasure, Dr. William Kirchhoff of the National Bureau of Standards for writing the original version of the code LOGIT and Dr. Denes Marton of the Technical University, Budapest, for sharing with the author his extensive knowledge of surface physics and vacuum technology. The author has spent many pleasant hours working with Dr. Kirchhoff and Dr. Marton on a number of prolific research projects. The collaborations with Dr. Kirchhoff and Dr. Marton have been the most productive and enjoyable of the author's life.

Gratitude is expressed to the National Bureau of Standards for the financial support which made it possible to work with Dr. Fine at the Bureau. The University of Maryland Computer Science Center is acknowledged for making available the computer time for the simulation calculations reported here. In addition, the author wishes to acknowledge Dr. Omer Goktepe for writing the original version of the code EVOLVE, used in this study.

Appreciation is extended to Linda Alvey for help with the figures and production. Thanks is extended also to Dr. Roger Stockbauer for his patient technical assistance during the author's early years at the Bureau of Standards. Special thanks is extended to Margaret Chambers who graciously and expeditiously typed the manuscript.

Finally, the author wishes to express his heartfelt appreciation to his parents for their efforts to educate their children. Their support and encouragement as well as that of the author's family have been instrumental to the completion of this thesis.

TABLE OF CONTENTS

LIST OF TABLES

LIST OF FIGURES

I. INTRODUCTION

A. Overview of the Topics to be Discussed

There is a great deal of current interest in the study of interfaces between dissimilar materials. For instance, in semiconductor devices it is essential to obtain extremely well defined interfaces between deposited thin films to avoid degradation in the device performance. Moreover, interface regions provide model systems for the study of both destructive and nondestructive surface analysis techniques. Auger sputter depth profiling, for example, is a destructive analytical tool that combines the process of systematic atom removal through energetic ion bombardment, sputtering, with a surface sensitive analytical technique, Auger electron spectroscopy. Auger electron spectra, characteristic of each element, can be recorded as as a solid surface is progressively and uniformly eroded to generate a profile of the material composition versus depth of a multicomponent sample. Unfortunately, the process of sputtering tends to distort the material system that one is attempting to analyze.

When this technique is applied to multilayered thin film systems, interface broadening often results as a consequence of the sputter profiling process, making it difficult to assess the original structure of the interface. There are a number of

factors involved in this broadening which are associated with the details of the ion bombardment and which have not previously been evaluated. These factors arise due to effects caused by the incident ions and consist mainly of surface roughening, amorphyzation, recoil implantation, cascade mixing, and radiation enhanced diffusion. It is the intent of this study to elucidate these processes as well as to determine the extent and regimes of their effects on interface resolution.

Sputter profile measurements carried out on a set of similarly fabricated Ni/Cr multilayered thin-film structures have shown that it is practical to systematically examine this interface broadening dependence on ion beam energy, ion current density, and angle of incidence. These measurements are all made as a function of sputtered depth. Results are presented of such a set of Auger sputter depth profile measurements and indicate that there can be dramatic changes in sputtered interface widths depending on the parameters characterizing the ion bombardment.

During the course of this study, it became obvious that it was necessary to develop a systematic, reliable, and unambiguous method of characterizing the interface region. A modified form of the logistic function, presented in this Thesis, is found to accurately model the composition versus depth distribution of a solid/solid interface as determined by Auger sputter depth profiling. The important parameters of

this model are T_o , the midpoint of the interface region and D, a scaling factor characteristic of the time for sputtering through the interface region. All conventional measures of the interface width are found to be proportional to D. Asymmetry in the depth profile is accommodated by allowing D to vary with time. A least squares fitting program was developed to fit measured Auger spectral intensities to the above equation to within measurement error (approximately 1%). The statistics associated with the least squares fit allow confidence limits to be placed on the measured widths of interface regions and on the asymmetry associated with each such region.

Radiation enhanced diffusion (RED), known to be a cause of interface broadening during sputter depth profiling, has been investigated specifically in this Thesis as a separate and distinct study. A layered Ag/Ni system, consisting of 5 thin (4 nm) Ag layers and 6 (50 nm) Ni layers was studied using Auger sputter-depth profiling techniques in conjunction with optical light scattering measurements of the surface roughening. The depth profile of each Ag layer is described by taking into account surface roughening and RED, both of which occur during the time of sputtering, by an asymmetric Guassian equation of the form :

$$c = c_o \, (4Dt+\Delta z_R 2/2)^{-1/2} \exp \, [\, -(St-z_o)^{\,2} \, (4Dt+\Delta z_R^{\,2/2})-1 \,]$$

This equation allows the separation of symmetrical interface broadening, due presumably to the development of surface roughness, from the asymmetrical profile skewing due to RED.

A detailed, microscopic investigation of the sputtering process using the Monte Carlo code EVOLVE is also presented. Basically, sputtering can be described as the ejection into the vacuum of target atoms from the near surface layers. Sputtered atoms leave the target in the vicinity of the point where an incident ion strikes the surface. Moreover, each incident beam ion and the recoil cascade it initiates dislodge target atoms in a volume of target situated about an extension into the solid of the path of the incident ion. The dependence of the above phenomena on the angle of incidence and the energy of the ion beam is examined using the Monte Carlo computer program EVOLVE.

Results are further presented concerning the distribution of the origins of the particles which sputter in addition to information bearing on the manner in which the recoil cascade grows in size and shape for the bombardment of a Si target with Ar ions. Lastly, sputtering yield angular distributions are provided for Ar ions incident on a eutectic In/Ga target.

B. Importance of Studying Interface Resolution and Ion Bombardment Effects

Ion bombardment of solid surfaces has gained considerable importance in recent years both as an experimental technique as well as an analytical tool. Sputter depth profiling plays a central role in the investigation of surface problems such as corrosion and adhesion[1] where it is essential to have a precise knowledge of the outer layers of a material sample. Typically, analytical surface techniques such as Auger Electron Spectroscopy (AES) and Secondary Ion Mass (SIMS) are used in conjunction with ion bombardment to determine the concentration versus depth elemental distribution within a solid. Interest in sputtering processes associated with energetic ion bombardment also stems from the nuclear fusion community where there is concern over the substantial number of atoms sputtered from the first wall of a fusion chamber due to the impingement of energetic plasma particles[2]. This process results in the erosion of the surrounding wall as well as in contamination of the fusion plasma.

Another area in which ion bombardment has recently gained importance is in the characterization of interface regions of thin films through sputter depth profiling. Interface regions are often of critical importance in thin films, microelectronics, and coatings applications amongst many others since they determine the physical properties and chemical stability of the device. Information on interface composition is frequently obtained by measuring surface

composition while the specimen material is gradually removed by ion bombardment. In this way, interfaces are revealed and characterized by the measurement of composition versus depth, ie. a sputter depth profile.

No general physical model currently exists for describing the shape of sputter depth profiles. Though proprietary interface-analysis software is avalaible for use with specific surface analysis instruments, none of this software attempts to parameterize the interface region systematically and statistically. Rather, use is made of various smoothing procedures and straight line approximations which do not result in an analytic function to describe the profile shape. Other attempts to characterize interface profiles with general functions (such as polynomials or error functions) have suffered from instabilities and an inability to handle poorly structured data. Moreover, they are characteristically cumbersome and expensive in the time required for their use.

The interface-analysis program LOGIT, however, described in this Thesis, provides a complete and accurate characterization of the interface region. Use of this algorithm results in a simple, convenient, rapid, and reliable analysis. The choice of the logistic function along with a specifically written least-squares procedure provides statistically evaluated parameters describing the asymmetry,

width, and midpoints of interface profiles in a reproducible and unambiguous way.

There is a great deal of current interest in radiation enhanced diffusion because it contributes to broadening of the interface region during depth profiling, consequently leading to degradation in the ability with which a buried interface region can be resolved. Few specific studies have been made of this effect and none of a Ag/Ni system which has been known to exhibit surface segregation when profiled. A study of the effect of experimental conditions as well as of the temperature dependence of RED, described in this Thesis, has been made to elucidate the mechanisms and activation energies for this process.

The technique of measuring the influence and extent of RED on sputter depth profiles described here has several advantages over previous techniques[3,4] . These previous methods consist of initiating sputtering on an alloy sample, ceasing sputtering and subsequently quenching the sample to liquid nitrogen temperature, thus freezing in the defects, and finally profiling the sample to determine the concentration versus depth distribution within the alloy. In contrast, our method consists of a single step,i.e. samples are held at a single constant temperature throughout the sputter depth profiling process. In addition to being simpler, this method has the virtue of being consistent with the technique with which most

active researchers in the field generate their profiles. Lastly, because our method of measuring diffusion differs from the previously employed quench method, our experiment provides an independent check on the work of others.

C. Review of Ion Bombardment Processes

Ions striking a material surface transfer their energy to atoms in the target material in the process of slowing down. Target atoms receiving energy in excess of their lattice binding energy are displaced from their original crystal locations. These moving atoms may now collide with other stationary atoms causing further displacements and ultimately lead to a collision cascade. This produces an altered material layer extending to the depth of the ion beam, typically several nanometers for keV energy incident ions. Target atoms approaching the surface with sufficient energy to overcome the surface binding energy of the material escape from the solid. These atoms are referred to as sputtered particles. Sputtering removes material from the surface resulting in topographic as well as compositional changes in multicomponent targets.

A variety of phenomena result from the sputtering process that tend to influence the depth resolution of the Auger sputter profiling technique. These are typically surface roughening, amorphyzation, preferential sputtering, recoil

implantation, cascade mixing, segregation, and radiation enhanced diffusion.

Surface roughening refers to the development of microstuctures on the surfaces of solids during the ion bombardment process.[5] This phenomenon appears to be due to the different rates with which materials are sputtered according to varying crystallographic orientations within polycrystalline targets. Regions which sputter more slowly, for instance, tend to remain as island structures as faster sputtering areas around them recede, giving rise to surface microstructure.

Amorphyzation is the breaking down of long range order in a solid material and results from the displacement of atoms during ion bombardment. Short range order may still be maintained, but the long range order of the solid crystalline lattice has been destroyed or lost. Recoil implantation and cascade mixing refer to processes which cause the compositional changes during sputtering in multicomponent targets as recoil atoms are displaced by energetic primary ions. Preferential sputtering refers to the process where different elements sputter at different rates in multicomponent material, thereby altering the composition versus depth distribution.

Lastly, segregation and radiation enhanced diffusion are processes characterized by the migration of defects produced in the solid crystalline structure during sputtering. Atoms displaced through energetic collisions leave their lattice

sites producing vacancies, unoccupied lattice sites, and interstitials, atoms between lattice sites. Vacancies and interstitials are referred to collectively as point defects, which may themselves combine to form complex defects. In any case, defects produced through collisions tend to diffuse over concentration gradients. Segregation occurs when defects of one element diffuse towards and build up on the surface of a multicomponent structure during sputtering. Radiation enhanced diffusion refers to the migration of these defects inside the sample producing an altered composition versus depth distribution.

II. DISTRIBUTION OF ORIGINS OF SPUTTERED PARTICLES AND THE SHAPE OF THE TARGET REGION AFFECTED BY THE CASCADE RECOILS

A. Introduction

Most of the atoms ejected from a target under ion bombardment originate from the first few atom layers[6]. Sputtered atoms are dislocated directly by the bombarding ions as well as by recoil atoms set into motion by collisions. In order to be sputtered, a dislocated atom must be near the surface and must either be set in motion towards that surface or become directed towards it by subsequent collisions it experiences. There is usually a chain of collision events from the first primary knock-on produced by an incident ion before a sputtered atom is produced. Thus the sputtered atom may be far removed from the ion-target atom collision which initiated the cascade.

As the angle of incidence is increased from normal to grazing, the sputtering yield rises to a peak and then decreases to zero as tangential incidence is approached[7]. The dependence of the sputtering yield on the angle of incidence of the ion beam is noteworthy since the sputtered atom is unlikely to have a "memory" of the direction of the incident ion. It is

possible that, though a sputtered atom does not contain much information about the incident ion's angle, the information is distributed in the cascade as a whole. If this is true, then such information may be in part contained in the spatial distribution of recoil production in the target, an hypothesis worthy of investigation.

The process of ion bombardment of a solid target sets target atoms into motion in a cascade process. The cascade region extends in depth to about the range of the incident ion and is composed of the atoms dislodged through direct impact by the beam ion as well as by recoiling target atoms. The spatial distribution of moving target atoms carries information concerning the transport phenomena. Knowledge of this spatial distribution may be useful not only in the investigation of the sputtering process but also in the study of ion implantation and related ion bombardment phenomena as well.

In addition to its dependence on the intitial angle of incidence and resultant collision cascade, the sputtering yield has also been found to be dependent on the energy of the incident ions. Such a dependence is to be expected as the number of recoils produced in the near-surface region is dependent upon the energy of the incident ion.

Very little information is found in the literature about the shape of the recoil density distribution even though such data is useful in developing an understanding of the dependence of sputtering yields upon incident angle as well as studies of

radiation damage effects. Shimizu et al.[8] traced the trajectories of recoil atom motion through the target for various incident angles and energies. In addition there is some work on the angular and energy distribution[9,10] of sputtered atoms; these results carry information about interactions beneath the surface.

EVOLVE[11], a computer program which simulates ion bombardment of materials, was used to study the shape of the collision cascade's recoil density for a single ion (or very thin beam) incident on the solid. Struck atoms which do not receive sufficient energy to be displaced from their sites are not included. It is assumed that the shape of the recoil density distribution can provide insight into the origin of the dependence of sputtering yield on the angle of incidence of the beam. As regions with higher collision densities are created closer to the surface the sputtering yields increase. To study these effects, computer simulations were carried out for Si targets bombarded by 5-keV and 15-keV Ar atoms. The incident angles used were 0^{o} and 60^{o} with respect to the surface normal. Simulations were made for all combinations of the two energies and two angles. The shape of the intensity distribution of recoil production in the target was obtained by outlining the disturbed region, from various perspectives, displaying contours of the recoil production density. Each contour represents a locus of points of equal recoil density.

The shape of the recoil cascade is investigated in detail by partitioning the cascade recoils into groups. The grouping is based upon the hierarchical ordering of sequences of collisions between the beam particles and the target atoms and thus the shapes of recoil cascades for successive groups resemble the time evolution of the whole cascade.

The generation or "G" model of grouping[12] of recoils used here is based upon the number of collisions occurring between the beginning of a cascade and the production of a given recoil. In this scheme, the group G_1 contains those recoils produced by the first collision of beam ions. Group G_2 recoils are generated by G_1 recoils in their first collision and by beam particles on their second collision. The group G_n then consists of recoils genereated by any chain of n successive collisions starting from an uncollided beam particle.

The sputtered atoms generally leave the surface at exit points which are not far removed from the point of impact of the incident ion. The distribution of exit locations of sputtered particles on the X-Y plane of the surface, where the surface normal denotes the Z-axis, has also been examined. Results are further presented which display the distribution of locations from which sputtered atoms are dislocated. Such information can be used to indicate the ultimate resolution of

ion microscopes which rely upon the detection of sputtered particles for surface analysis.

This portion of the overall work was performed by the author under the direction of Dr. Marvin Roush and Dr. Farhad Davarya using the ion bombardment simulation code EVOLVE, written by Dr. Roush, Dr. Omer Goktepe, and Dr. Tim Andreadis. The author performed specific modifications to the code necessary for this study and in addition developed companion software to selectively investigate the planar slicings and G groupings of recoil distributions within the simulated solid.

B. Computer Simulation of Ion Bombardment

Computer simulations of collisions in solids may be roughly divided into two groups: Molecular dynamics calculations, where a model crystal is treated taking projectile-target as well as target-target interactions into account simultaneously, and binary collision approximations, where only one collision between two atoms may be handled at a time. In molecular dynamics calculations, a model of a crystal lattice is established in the computer. The target atoms are allowed to interact through interatomic forces which are chosen to be as realistic as possible. Binary collision codes, by contrast, employ Monte Carlo, or random number generation,

techniques treating each projectile-target atom and target-target atom interaction as an individual event. The interaction potentials are selected similarly to those in molecualr dynamics calculations.

Molecular dynamics computer simulation techniques for the study of sputtering of crystalline targets have been developed by Harrison et al.[13-14] and by Robinson et al [15-16]. A number of other researchers have developed Monte Carlo simulation codes which are applicable only to amorphous or polycrystalline samples[17-20]. Ishitani et al.[18,21] have applied such a code to calculate ion trajectories within homogenous multielement targets.

Computer programs of this nature do not calculate the rearrangement of target material directly. They can be used, however, to calculate displacement probability distributions, i.e. the probability that an atom at a depth Z from the target surface will be moved to a position Z' during ion bombardment, as was demonstrated by Kang et al[22]. These authors used displacement probability distributions to approximate the atomic mixing with the assumption that these distributions are not changed by the material rearrangement.

An underlying assumption in many of these computer programs which have been used to model sputtering and cascade-development is that the implanted beam atoms do not play a significant role. In these models, the composition of the

target remains unchanged throughout the calculation and should be compared only with the results of low-fluence experiments. On the contrary, however, they have often been compared to the results of experimental measurements made upon equilibrium targets. In this chapter, the computer simulation code EVOLVE is described which has specifically been developed to provide the capability of folowing time-dependent composition changes which take place in nonuniform multielement targets under ion bombardment.

C. EVOLVE Code description

The Monte Carlo Code, EVOLVE[11], is used to simulate atomic collision cascade effects in the ion bombardment of solids. In multicomponent solids, the cascade development is affected by the mass difference[23,24] as well as by the dissimilar binding energies[25] (surface and bulk) of the constituents.

EVOLVE treats the transport and scattering of ions (and recoil atoms) in a solid as in a random walk problem. The trajectories of individual particles are followed in the form of straight-line segments joining points of interaction. The target is treated in slab geometry with the elemental composition of each slab evolving in order to represent the

changing composition of the system. Atoms in the target are treated as randomly located.

Atom-atom interactions are treated in the binary approximation. If the struck atom receives kinetic energy in excess of a displacement energy E_d, the atom leaves its site with a kinetic energy $T-E_d$, where T is the energy loss of the incident atom. Beam atoms and recoiling target atoms are tracked through the target until they leave the surface or lose sufficient energy to fall below 1.2 eV. A moving atom may escape from the target on reaching the surface by overcoming the surface binding energy, E_s, which was represented by using a planar model[26].

The scattering angle for individual interactions is dependent upon a randomly selected impact parameter and is found by integration of the classical central-potential scattering integral. The Thomas-Fermi potential with the screening function of Moliere[16], was used as the interaction potential.

A calculation of electronic energy loss was carried out for each segment of path length using the present material composition for that layer. Since the ion velocities involved here are less than the velocity of the electrons in the first Bohr orbit, the formulation of Lindhard and Scharff[27] was used to calculate electronic energy loss.

D. Shape of the Recoil Cascade

Figure 2.1(a-d) displays four selected recoil track patterns, each for a single 15-keV Ar ion incident upon silicon. The superposition of 20 such patterns is shown in Figure 2.1e, where the dark interior gives an indication of the average shape of the recoil cascade. The individual track patterns show considerable variation from cascade to cascade. The following section will deal with the average spatial behavior and with the recoil production density distributions.

To obtain the average response, the spatial distribution of the number of recoils produced was recorded for the trajectories associated with 5000 incident particles. This was accomplished by dividing the target into a three dimensional rectangular mesh of small volumes with an integer assigned to each volume. The integer assigned to a volume was incremented whenever a recoil was created in that volume. After the simulation was complete, the data were processed to exhibit features of the recoil production density distribution. The perspectives used to illustrate the shapes are those an observer would see facing the X-Y, X-Z, or Y-Z planes. In the case of the X-Y plane, all recoils within a given X-Y grid interval were summed (independent of Z) to obtain a projection onto the X-Y plane. The contours represent lines along points of equal recoil density. In all the cases presented here the ion beam's impact point is the origin, the beam is in the X-Z

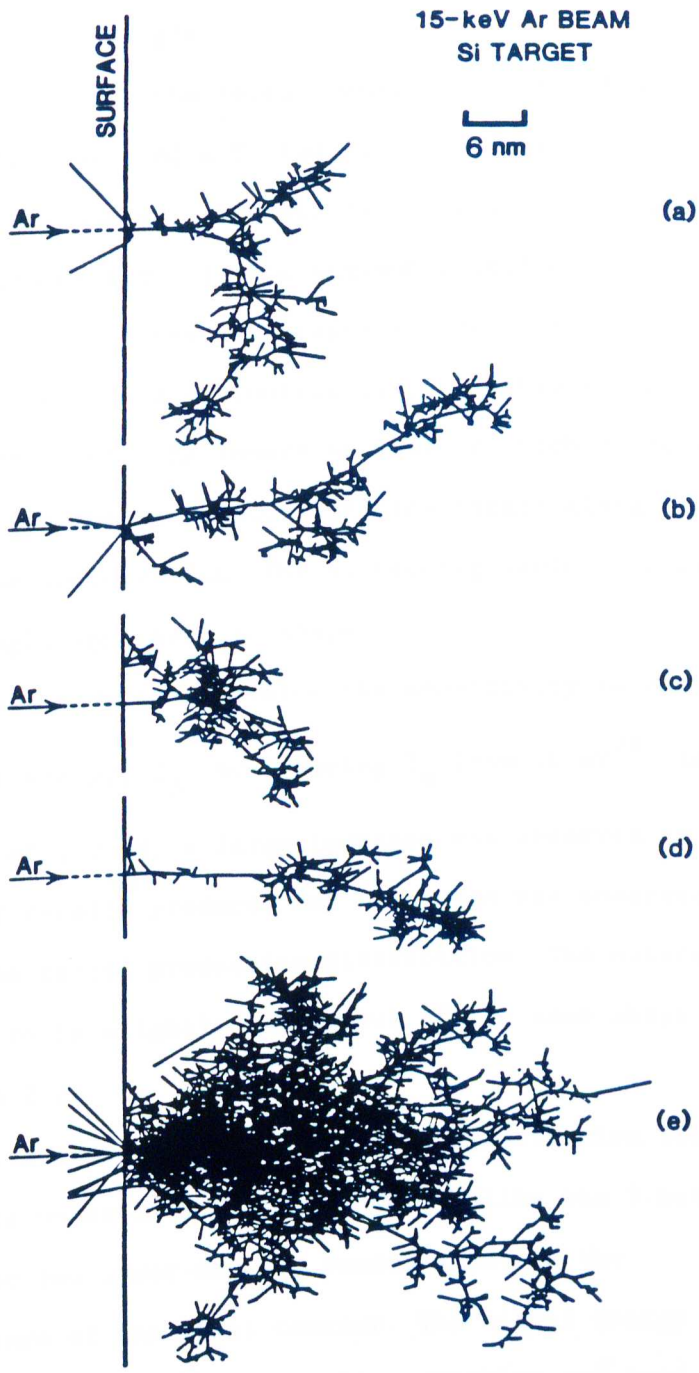

Figure 2.1 Track patterns are shown (a-d) for single 15 keV Ar ions incident normally upon Si. The trajectories are shown for both incident ion and all recoil atoms. The lines emerging from the surface indicate reflecting ions or sputtered atoms. The combined tracks for 20 particles are shown in (e).

plane, and the beam has a positive velocity component in the X direction for oblique angles.

Figure 2.2a shows the recoil density distribution produced by bombardment of a Si target by normally-incident 5-keV Ar atoms. The innermost contour represents the higher recoil production density. If the maximum recoil density is normalized to 6, the curves will represent densities of 5,3, and 1. As expected, the distribution is reasonably symmetrical about the impact point. The innermost contour which represents the higher number density extends into the target along the direction of the incident ion. The succeeding contours appear to be increasingly spherical in shape.

A study was made to determine the sensitivity to choice of displacement energy, E_d. By reducing E_d from 14 eV[28] to a very low value of 1.2 eV, a large increase was observed in the total number of recoils produced but no change was observed in the shape of the recoil production distribution. The outermost contour tended to be slightly larger but of the same shape as shown in Figure 2.2.

Figure 2.2c shows the recoil density distribution for normal incidence under 15-keV bombardment. Unlike the 5-keV case, the latter two lower-density contours retain the cylindrical nature of the first contour. The higher energy ions are less likely to undergo large-angle scattering and tend to

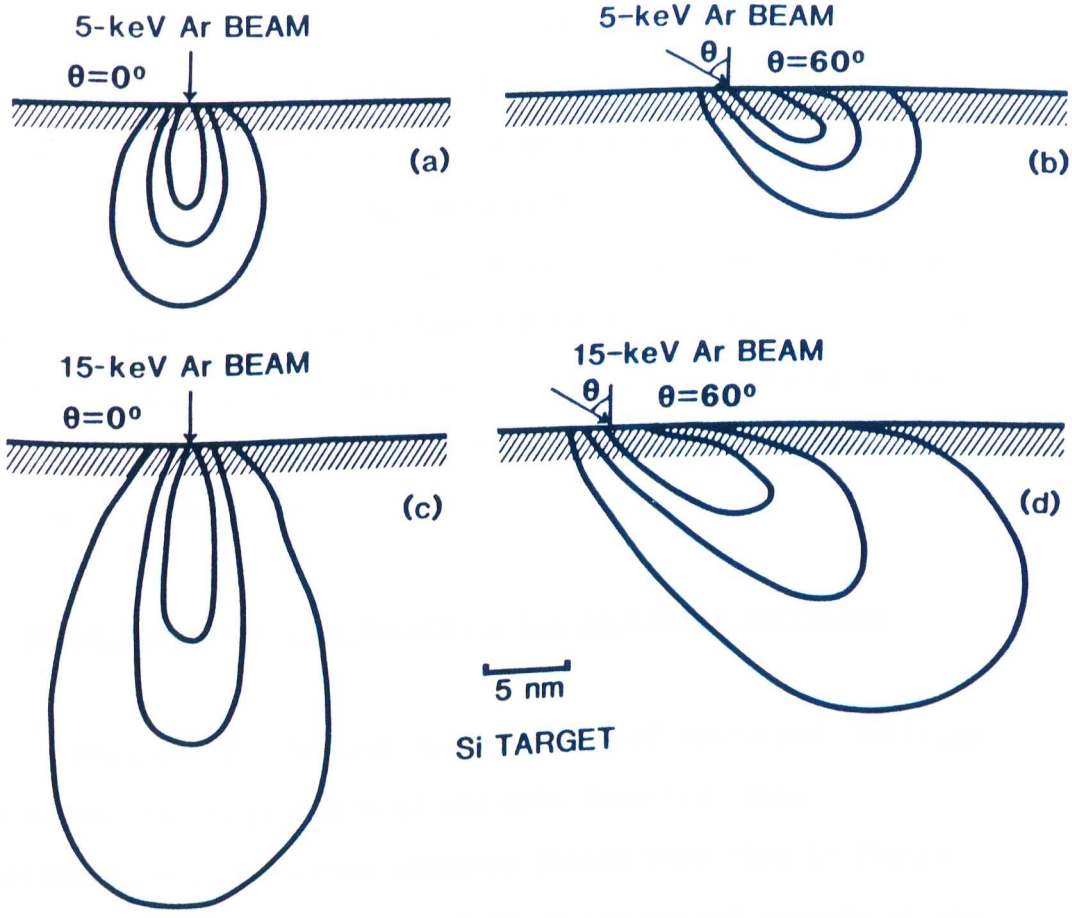

Figure 2.2 Recoil density contours are shown for Ar bombardment of Si. The incident energy is 5 keV for (a) and (b) and 15 keV for (c) and (d). The angle of incidence is 0^{o} for (a) and (c) and 60^{o} for (b) and (d).

retain the inward directed momentum within the cascade (incident ion and recoiling atoms).

Oblique incidence brings the regions of high recoil density closer to the surface of the target as may be seen in Figures 2.2b and 2.2d. As more recoils are produced closer to the surface the sputtering yield will increase.

Figure 2.3a shows the projection of the recoil density distribution onto the X-Y plane for normally incident 15-keV Ar ions. The distribution peaks sharply at the axis along which the beam is incident, dropping to 1/e of the peak intensity at 3.9 nm from the axis.

E. Distribution of Exit Locations for Sputtered Particles

Figure 2.3b displays the intensity of sputtered particles as a function of position of the exit location. This distribution is even more narrowly peaked than that in Figure 2.3a, reflecting the narrow nature of the recoil cascade at the point of entry on the surface. Here the intensity drops to 1/e of the peak value at 2.1 nm from the point of incidence of the ion beam. The projection of recoil production density shown in Figure 2.3a reflects the broader nature of the recoil cascade at points well below the surface.

Figure 2.4 shows the distribution of the exit locations for sputtered Si target atoms due to 5-keV Ar bombardment at an

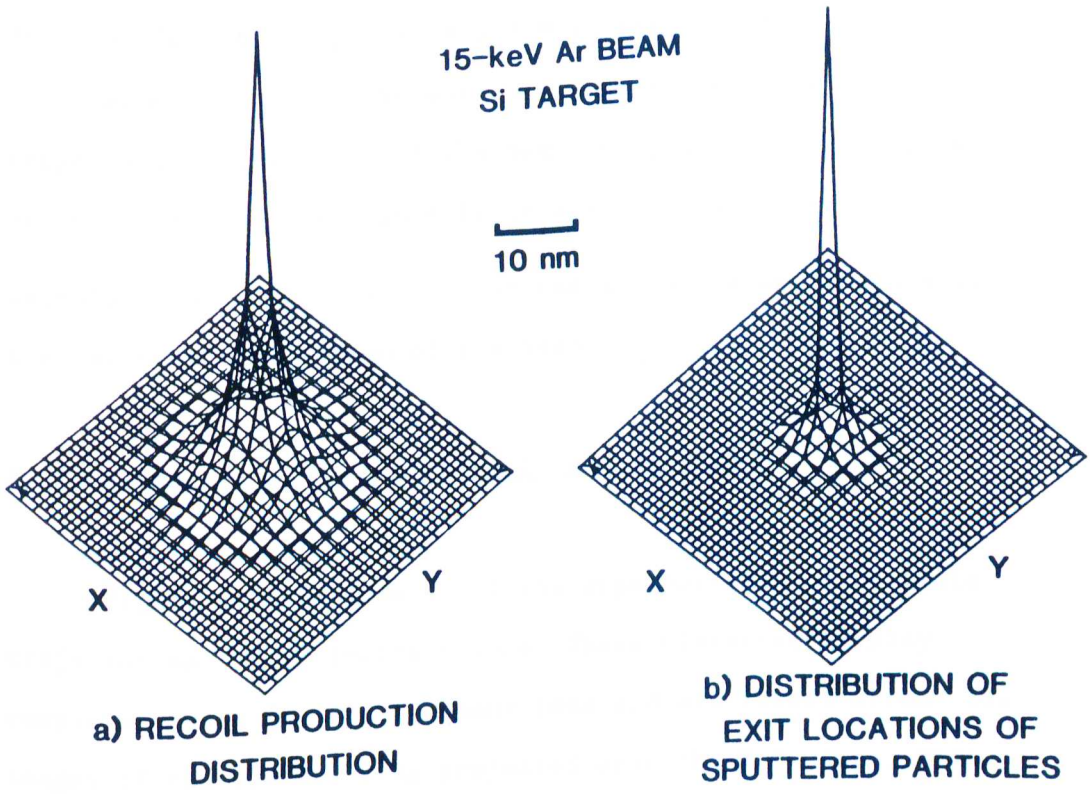

Figure 2.3 (a) Projected recoil density distribution for 15 keV Ar normally incident on a silicon target. The Ar ions strike the shown plane surface at the center. (b) Distribution of the exit locations of the sputtered Si atoms.

angle of 60^{o}. The distribution of sputtered particles as a function of the x-coordinate of exit locations is displayed in Figure 2.4a. Figure 2.4b shows slices taken through the distribution at the points A and B in Figure 2.4a.

Atoms sputter preferentially from the portion of the target which lies ahead of the beam and past the impact point on the surface. This result is in agreement with previous calculations[11]. The distribution has a crest along the X axis, i.e.,along the direction of the beam.

F. Time-Dependent Shape of Recoil Cascade Region

Figure 2.5a is made up of the superposition of particle trajectories for 20 incident ions. These histories display complete tracks for the incident ions and all recoil atoms, the images of the tracks being projected upon the X-Z plane. This superposition gives some idea of the average shape of the cascade region although individual particle histories vary widely as has already been shown.

The remainder of the track patterns, shown in Figure 2.5b-g, show selected portions of the particle histories. Each of these patterns contains only members of a selected generation (G_n group). For example, the G_3 display shows the first track segment for those recoils produced by the third collision in a sequence of collisions. This breakdown into

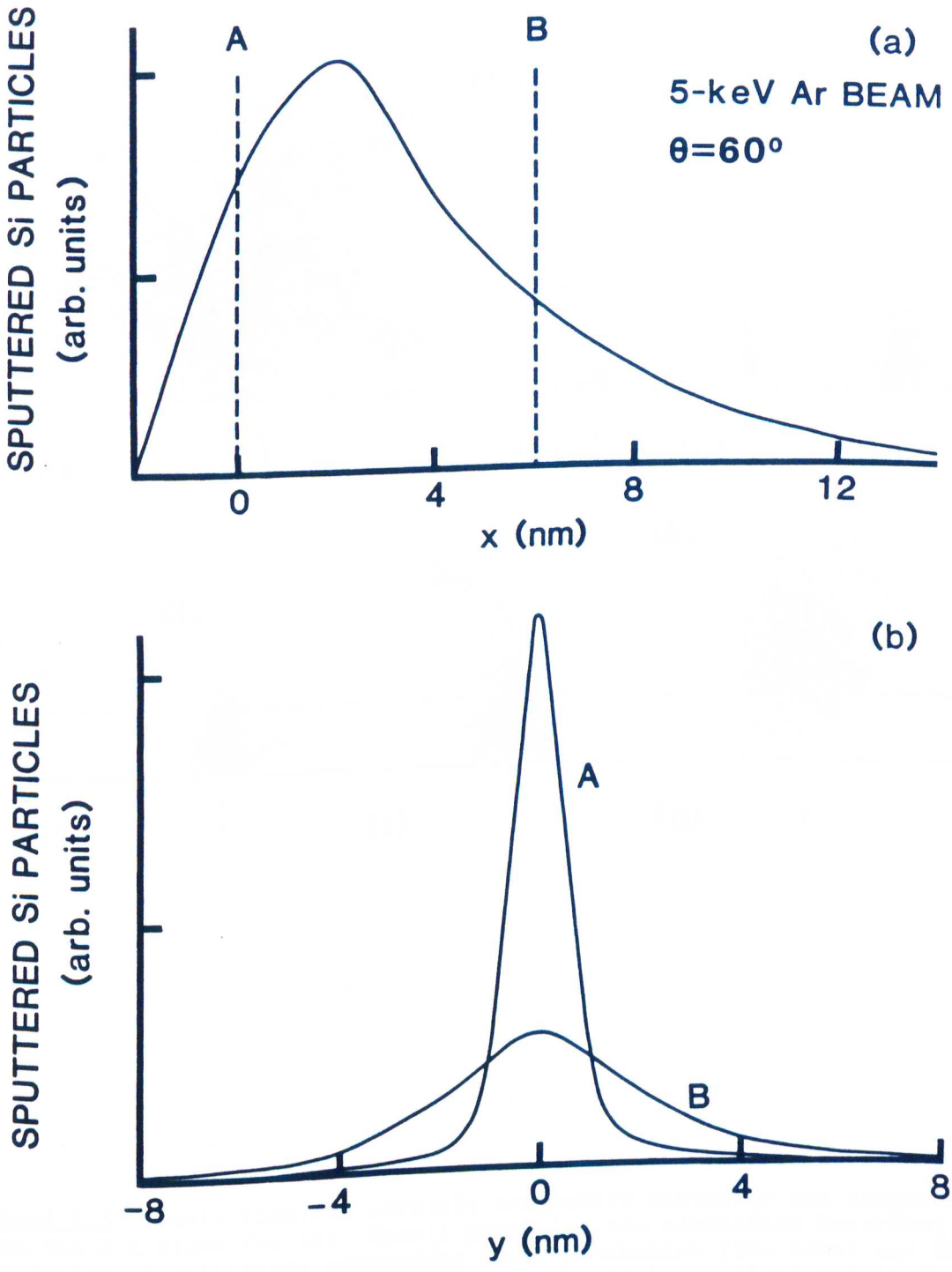

Figure 2.4 (a) Number of sputtered particles as a function of the x coordinate on the surface for 5 keV Ar incident on Si. The Ar ions strike the target at x=0. (b) Distribution of the sputtered particles in the y direction are shown for fixed x value at the points A and B.

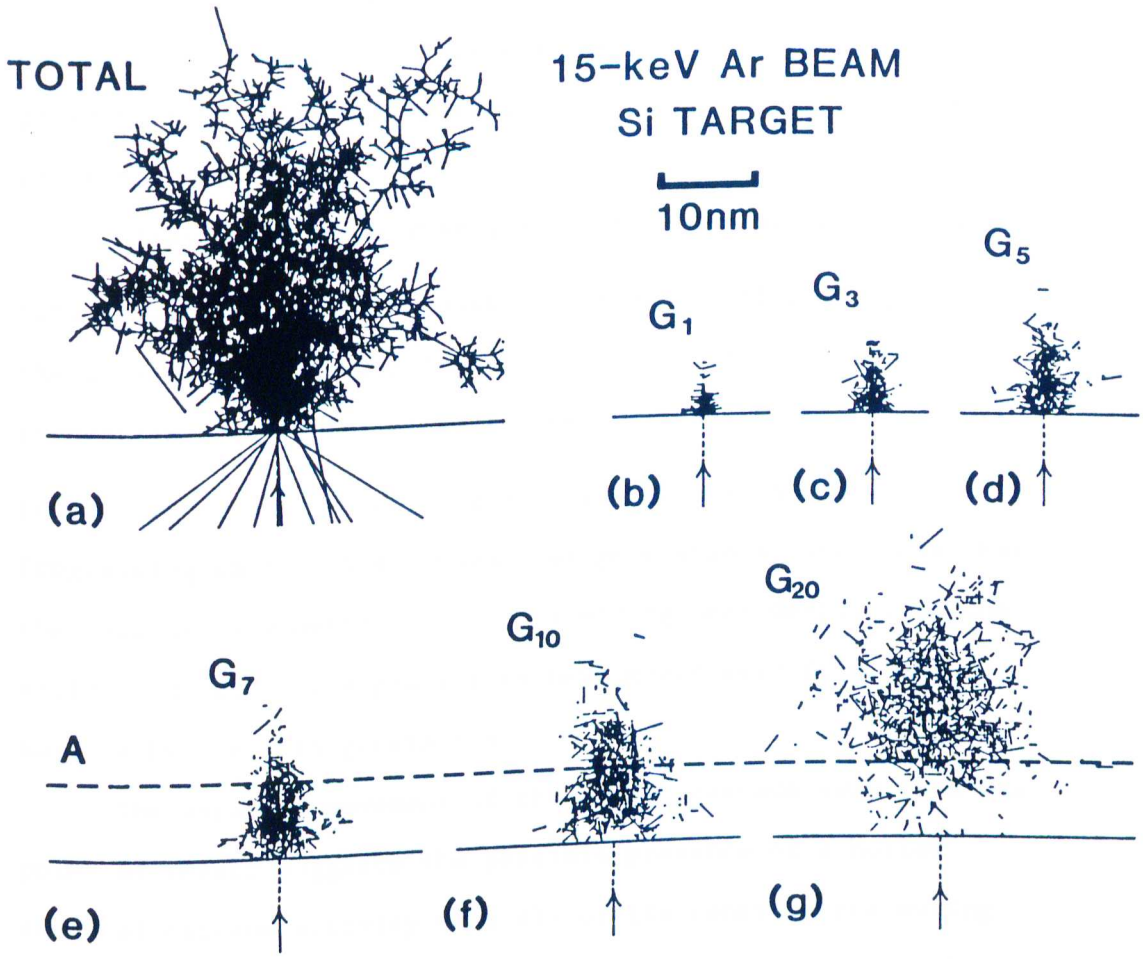

Figure 2.5 Twenty complete particle trajectory histories are projected onto the X-Z plane for (a). Recoil particles are classified according to the number of collisions preceeding their production (see text) and the first segment of selected recoil generations (G_n) are displayed in (b-g).

groups of track segments representing a sequence of generations can be used to display the general manner in which the cascade grows in time, although there is no direct connection between generation and time.

Figure 2.5b shows that all G_1 particles arise from the first collision of an incident ion, thereby originating along the line of the incoming ion. The majority of this recoil production occurs very close to the surface with the G_1 recoil production density decreasing exponentially with depth. Progressing through the sequence of generations, one finds that the cascade is growing in size, extending more deeply into the solid, and actually appearing to have moved away from the surface by the 10th generation.

The apparent movement of the recoil cascade away from the point of impact suggests the possible presence of a hollow shell of cascade activity with all of its constituents moving away from the point of incidence. We have attempted to evaluate this possibility by examing the cross-section of the recoil cascade at a depth of 7.5 nm (shown by the dashed line in Figures 2.5e-g). The track segments for G_7, G_{10}, and G_{20} having starting depths within 7.2-7.8 nm are shown in Figure 2.6. Here we see that the size of the cascade cross section tends to grow progressively with increasing n value,

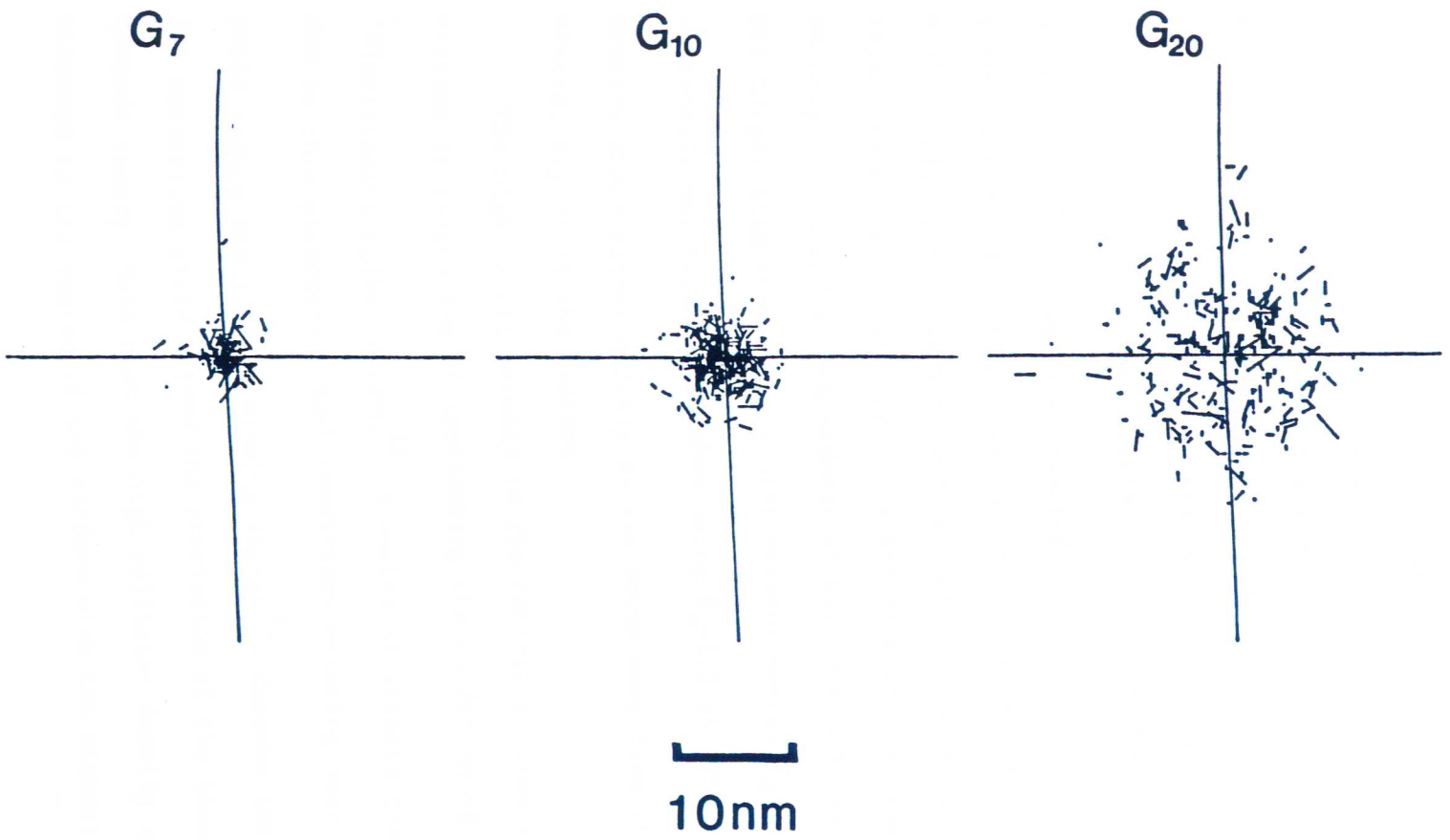

Figure 2.6 A cross section through the recoil production density distributions in fig. 1.5 (e-g) is shown. The depth at which the density distributions were sliced is shown by the dashed line in fig. 1.5.

but shows no evidence of a shell-like structure with recoil density decreasing toward zero at the center.

We note that all of these observations are based upon the linear cascade approach which assumes each particle is moving through a reasonably undisturbed solid. If the number of recoil events in a region approaches the local atomic density, nonlinear effects can be expected as has been discussed by many authors [25,29-31]. We have examined the average recoil-production density with a resolution of 0.1 nm, finding very high recoil density in a region .1 nm by .1 nm around the impact point of the incident ions and extending approximately 2 nm deep for 15-keV Ar bombardment of Si. We found .35 recoils per target atom when using a displacement energy E_d=14 eV and .6 recoils per target atom when using E_d=1.2 eV. The recoil density drops rather quickly as one moves away from this central region of the cascade.

The high recoil density in the central portion of the cascade is indicative of approaching the condition of a "displacement spike" region[32]. A number of effects could result due to this phenomenon. Such conditions occuring near a surface could reduce the surface binding energy[33], thereby increasing the sputtering yield beyond the prediction of the linear cascade theory. Note that the high collision density spike is situated in the region of the surface with the highest

sputtering yield. In addition this phenomenon could also allow sputtering of atoms which originate from significantly deeper layers than the first one or two monolayers as predicted[34] through the linear theory.

G. Distribution of Origins of Sputtered Particles

A simulation of 15-keV Ar ions normally incident on Si was carried out for 5,000 incident particle histories. All sputtered particles were sorted according to the X-Y coordinates of their point of origin, Figure 2.7 shows a 3-dimensional perspective display of the lateral distribution of the origins of sputtered particles. A large portion of the sputtered particles come from locations very close to the line of the incident beam. The narrow distribution about the beam line is seen to drop to 1/e of the maximum value in about .3 nm, although the mesh size of this calculation was not adequate to provide a good measure of resolution. This width of the distribution arises from diffusion of the cascade particles since the beam itself is assigned no width for the current calculation. The observed resolution of an ion microprobe is at least a combination of the width observed here with the contribution which arises from the beam size. The narrow distributions of sputtered-particles origins could prove useful in the future as the ability to provide small beam spots improves[35] . Scanning electron beams are often limited to

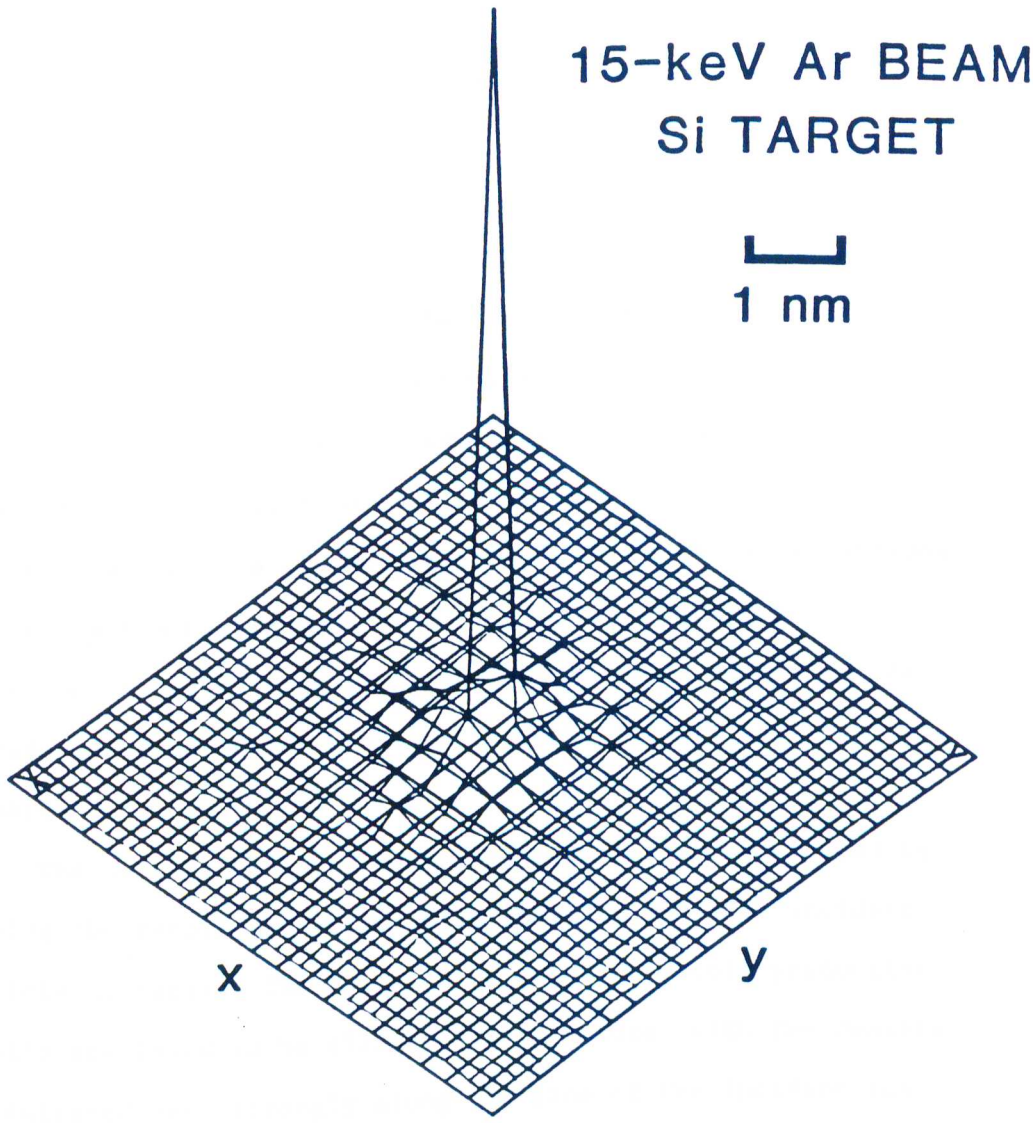

Figure 2.7 This perspective display shows the distribution of the origins of sputtered particles relative to the location of the beam direction which is coincident with the Z-axis.

resolutions of a few micrometers because the electron beam scatters into a "bloom" or cloud after entering the solid[35] .

H. Summary and Conclusions

EVOLVE simulations have been utilized to demonstrate the track patterns formed by trajectories of single bombarding ions along with associated recoil particles. These patterns are shown to vary greatly from particle to particle. EVOLVE has further been used to produce images of the recoil atom cascades induced by ion bombardment of a target. The bombardment of Si by 5- and 15-keV Ar ions was investigated and a number of the cascade characteristics obtained from the results are summarized below.

The average behavior of recoil cascades was exhibited by summing the recoil production distributions for 5000 incident particle histories. The contours of constant recoil production density are found to be ellipsoidal in nature, with the density concentrated very strongly along the line of the incident ion.

As the angle of incidence moves away from the surface normal, a portion of the ellipsoidal recoil cascade is brought closer to the surface where recoils can escape, with corresponding increases in the sputtering yield. As the ion energy is decreased from 15-keV to 5-keV, the average

scattering angle increases and a more spherical shape for the cascade is demonstrated.

It may be seen that the recoil cascades are narrow at the surface and broaden as the depth into the target increases, as expected. Along the projection into the target of the incident beam there exists a region of high recoil density. The ion bombardment sets a large portion of the target atoms into motion. In this region the linear cascade theory may not be entirely applicable. The significance of this effect needs to be explored more rigorously before any conclusions are reached.

By applying the generation method of segregating groups of recoils a number of features of the cascade were brought out. It was observed that the recoil activity grows in size and moves away from the target surface. Another observation was that most sputtered atoms arise from early generations and are produced from sites close to the bombarding ion's entry point. This area is also where the high recoil density mentioned above is situated and thus raises the possibility of a drop in the local surface binding energy, a parameter of well known importance to the sputtering yield.

III. DEPENDENCE OF THE SPUTTERED ATOM ANGULAR DISTRIBUTION ON THE DEPTH OF ORIGIN

A. Introduction

The theoretical description of sputtering by Sigmund [37] indicates that sputtered atoms originate from the uppermost 5-10 angstroms of sputtered samples. The detailed features of the sputtering process are affected by both the composition and the compositional gradient in the surface layer. It was predicted by Sigmund et al. [38] that sputtered atoms of one element originating beneath a surface-enriched layer of another element will exhibit a narrow angular distribution peaked at the surface normal. This feature of the angular distribution arises due to the reduction by the surface layer of the fraction of atoms originating deeper in the sample which exit at oblique angles.

Measurements of sputtered atom composition as a function of ejection angle have been used to indicate the presence of a segregated layer of indium on a liquid-phase Ga-In eutectic [39] and of copper on a CuPt alloy [40] during Ar^+ ion bombardment.

The experiments of Dumke et al.[39] were directed towards an investigation of the angular distributions of sputtering

yields of alloys as a funtion of depth. Their work was based on the assumption that sputtered atoms come predominantly from the top monolayer of a solid surface. These authors used Rutherford backscattering analysis of graphite collector foils to investigate the angular distributions of sputtered atoms from both the solid and liquid phases of gallium, indium, and gallium eutectic alloy. The targets were sputtered using 15 keV Ar^+. It was found that the angular distribution of sputtered gallium was more sharply peaked about the surface normal than was the indium distribution. In addition, it was observed that the angular distributions from liquid targets were well fit by a $\cos^2\theta$ function. It was concluded from this study that the majority of sputtered atoms originate from the first monolayer of the target.

In addition to this work, angular distributions of sputtered particles have been measured for a variety of combinations of target and bombardment species [39-42]; the resulting distributions can be characterized by $\cos^n\theta$ with values of n commonly between 1 and 2 but extending to as large as 5 [42].

The process of sputtering can be characterized by a model which includes an attractive surface force parameterized in terms of a surface binding energy, E_s and a local potential well which must be overcome in order to set an atom in motion

within the bulk solid, a feature parameterized by the use of a displacement energy, E_d.

Computer simulation codes [42-45] are frequently used to study the effects which arise from particular assumptions or from particular facets of the model of the process. These calculations have shown [46-48] the sputtering yield to be quite sensitive to assumed values for E_s and E_d.

The current work was undertaken, under the direction of Dr. Marvin L. Roush and Dr. Tim Andreadis, to examine the sensitivity of predicted angular distributions of sputtered atoms to their depth of origin as well as to a set of assumptions made concerning E_s and E_d. The study was performed using the Monte Carlo computer code EVOLVE, described in Chapter II. In addition to making specific modifications to the EVOLVE code necesary for this study, the author developed companion software to evaluate the dependence of angular sputtering yield distributions on depth of atomic origin and on choice of atomic surface and bulk energetic interaction model.

B. Surface Binding And Displacement Energies

The displacement energy is often separated into two parameters E_v, the threshold energy to produce a recoil, and

E_b, the energy lost in removing the atom from its position. Many calculations are done with $E_b = 0$. EVOLVE calculations combine these two parameters into E_d, the displacement energy.

The parameters E_d and E_s are a simplified representation of the summation of the potentials in a material. They take into account an averaging of effects from very complex force fields. Since they arise from the same source, the interatomic potentials, the two parameters have proved difficult to deconvolute.

It is plausible to assume that a depth dependence exists for the displacement energy. Since there are fewer neighboring atoms at the surface, atoms located at greater depths in the target are more tightly bound in their locations than atoms at the surface. For this reason, a depth dependent displacement energy model is used in this study.

This model is supported by a recent paper by Kelly[49], who has reformulated the quantitative sputtering yield model of Sigmund to include a proper definition of the surface binding energy E_s in terms of nearest neighbor atomic binding energies. Although E_s is usually identified with the cohesive energy (the heat of atomization), Kelly has argued that the cohesive energy yields values for E_s that are too low because it relates to half-space atoms (atoms at the surface with few adjacent neighbors) as opposed to in-surface atoms which are more nearly

typical of a sputtered surface. In Kelly's model, the binding energy of an atom depends, in part, on its depth below the surface.

In addition to the depth dependence, the displacement energy has been found to be related to the surface binding energy in a formulation recently discussed by Biersack and Eckstein [50]. Using the computer program TRIM.SP, these authors showed that the sputtering yield did not change when E_b and E_s were varied, as long as their sum was held constant; this sum being normally set equal to the heat of sublimation, H_s.

The model used in this study is shown in Figure 3.1. The displacement energy has a value E_{dt} over an interval bounded by the surface and a depth Z_t, equal to the nearest neighbor distance. From this point the displacement energy is increased linearly to the bulk displacement energy E_d at the depth Z_s. Equation 3.1 indicates how the quantities E_s and E_{dt} are specified.

$$E_s = E_{dt} = 1/2\ H_s \tag{3.1}$$

Values of bulk displacement energy and heat of sublimation were taken from the compilation of Andersen [51].

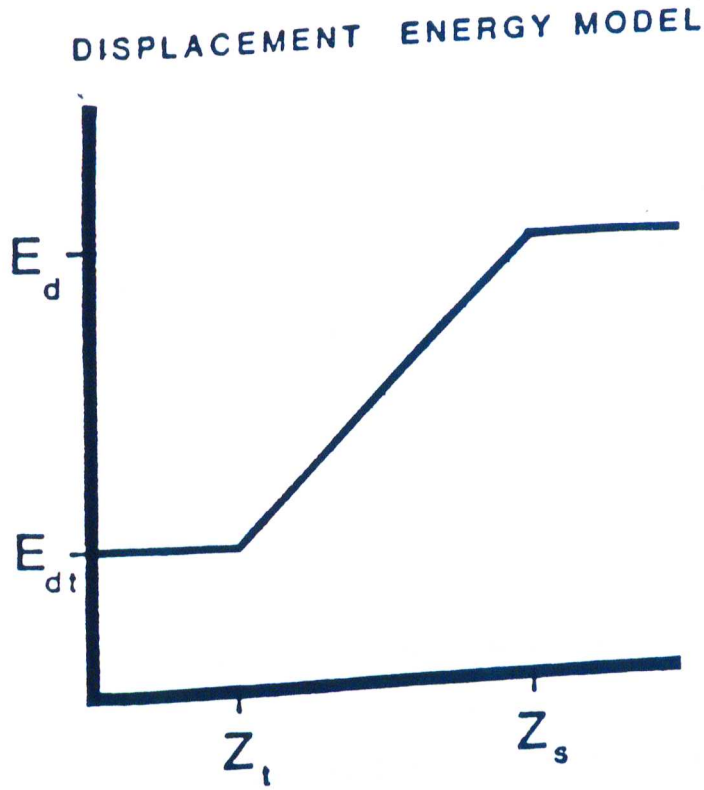

Figure 3.1 The depth dependent displacement energy model used in the EVOLVE calculations.

C. Sputtering Yield Calculations on Ni and Ge

One necessary criterion for an acceptable displacement energy model is that it produce values in reasonable agreement with experimental sputtering yields. Sputtering yield calculations were made for Ni and Ge targets using the displacement energy model described above. Incident ion energies were in the 1 - 10 keV range. In addition, calculations were made at different values of Z_s for the Ni target in order to examine the sensitivity of sputtering yields to the model parameters.

Nickel and Germanium targets were selected because of their different properties under bombardment. Nickel maintains its face centered cubic crystal structure during ion bombardment whereas LEED studies indicate that the diamond lattice structure of Ge deteriorates rapidly [52], becoming amorphous during ion bombardment.

Figure 3.2 shows a comparison of calculations of sputtering yields with experimental results [53] for Ar bombardment of Ge. The distance Z_t was taken to be 0.244 nm while Z_s was chosen three times as large. The surface binding energy used was 1.9 eV while the displacement energy of bulk atoms was 7.6 eV.

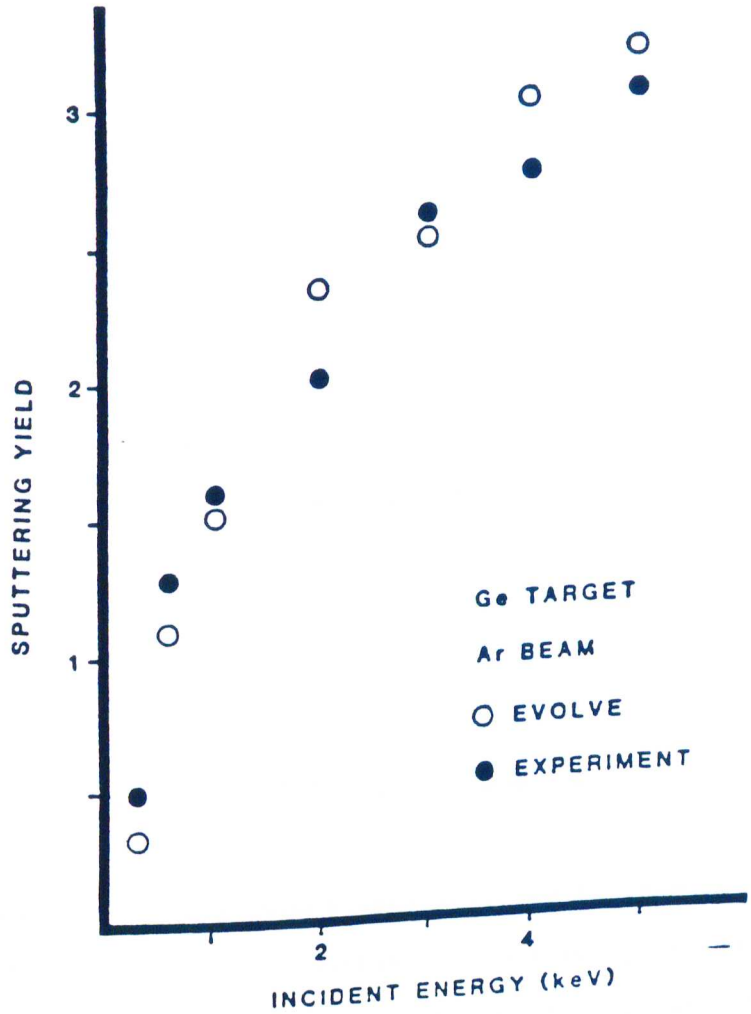

Figure 3.2 EVOLVE calculations of the sputtering yield for Ge bombarded at normal incidence by Ar ions. Experimental data is from reference 19.

Figure 3.3 displays a similar comparison of calculations of sputtering yield with experimental results [53] for Ne bombardment of Ni. The distance Z_t was taken as 0.249 nm while Z_s was chosen as twice as large and as three times as large for the two calculations. The surface binding energy used was 2.23 eV and the displacement energy for bulk atoms was 20 eV.

This depth variation for the displacement energy can be seen to produce sputtering yields which are in reasonable asgreement with experiment when Z_s is chosen 2.5 - 3.0 times the value of Z_t, the nearest neighbor distance.

D. Angular Distribution of the Sputtering Yield

Simulation calculations were utilized to examine the variation in angular distribution of sputtered particles with depth of origin. Conditions were chosen to represent those of the experiments of Dumke al. [39], where variations in angular distribution were interpreted as arising from a monolayer of In which was found to form on the surface of a Ga-In alloy.

Three different samples were simulated for these calculations. Gallium, indium, and gallium covered with a monolayer of indium were bombarded by 15-keV Ar ions. Five thousand incident particle histories were calculated for each

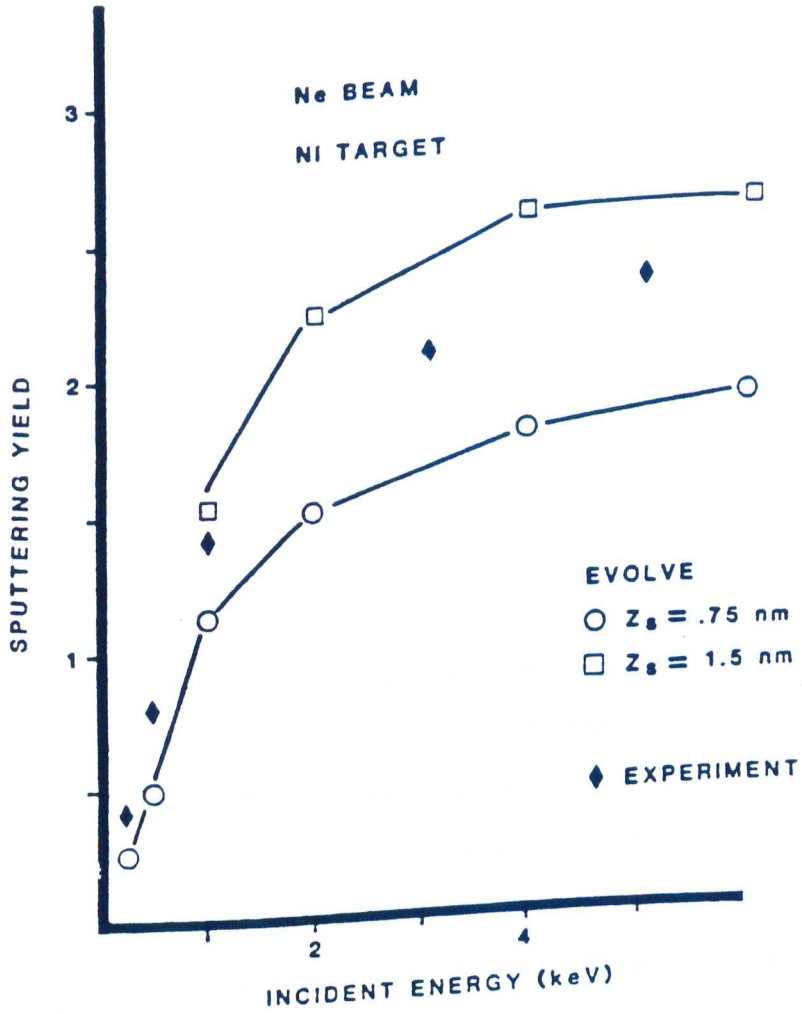

Figure 3.3 EVOLVE calculations of the sputtering yield for Ni bombarded by Ne atoms. Calculations for Z_s values of 0.75 nm and 1.5 nm.

target sample. Details concerning each sputtered particle were recorded and angular distributions compiled for sputtered particles originating within a selected depth interval. Depth intervals of 0.30 nm and 0.24 nm were selected for In and Ga respectively, representing the distance to the nearest neighbor atoms. Surface binding energies of 1.25 and 1.3 eV were used for In and Ga respectively. Displacement energies were taken to be 15 eV for In and 12 eV for Ga obtained from the compilation of Anderson [51].

Figure 3.4 shows the sputtered atom angular distributions of the three top layers of the In/Ga sample. Each individual angular distribution was fit to a function of the form $A\cos^{n}\theta$. The angular distributions grow more strongly peaked at the surface normal as the depth of origin is increased. The fits range from n = 0.88 for the top layer to a value of approximately 2.4 for the fifth layer and all deeper layers. Although the uncertainties increase with depth because of the decreasing yield of sputtered atoms, there appears to be a region for which associated angular distributions are similar.

The angular distributions and their variation with depth of origin were found to be very much the same for the simulations of sputtering of pure In and Ga.

While the simulation calculations have shown the qualitative depth dependence anticipated, the calculated angular distributions are not as sharply peaked as was

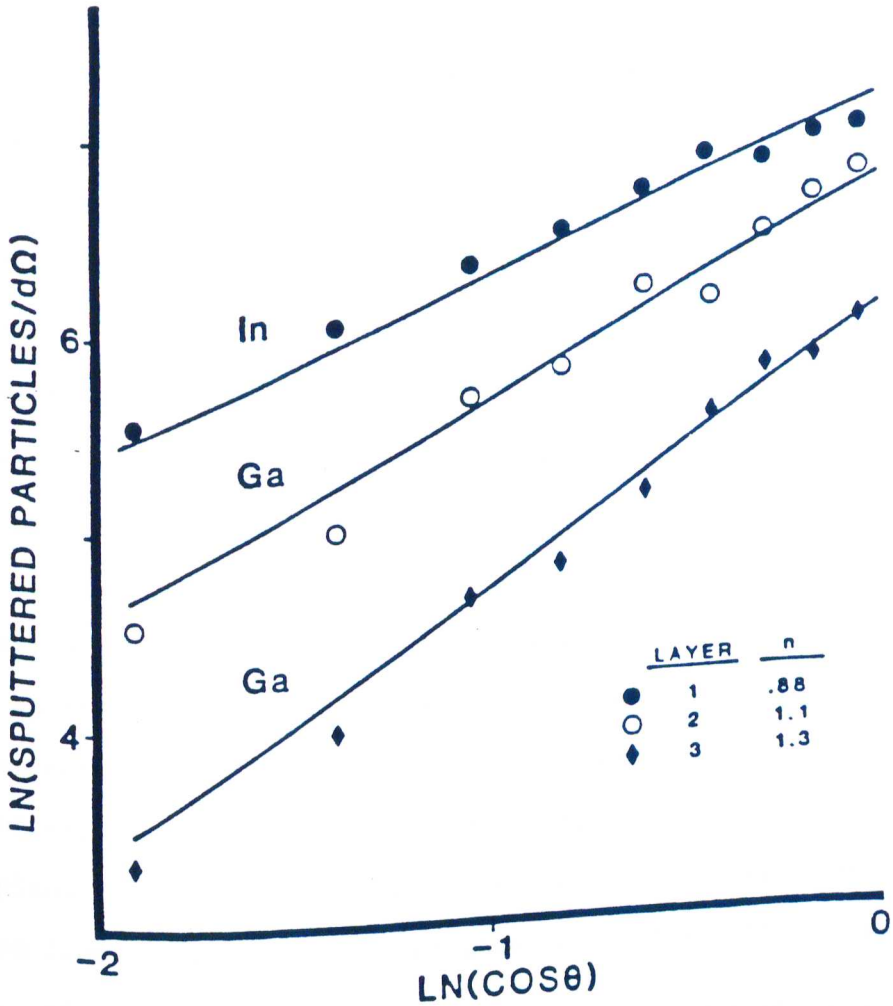

Figure 3.4 EVOLVE calculations of the angular distribution of atoms sputtered from a Ga target with a surface layer of In. Solid curves are line fits of the form $A\cos^{n}\theta$. Bombardment was with 15-keV Ar at normal incidence.

observed by Dumke et al.[39]. For pure samples the simulation results gave n equal to about 1 rather than the experimental observation of about 2. Similarly, the EVOLVE results for Ga sputtered from under a monolayer of In gave an n of 1.2 as compared with experimental observation of 3.6.

The reason for these discrepancies is, we believe, two-fold. On the one hand, the experiments of Dumke et al. were performed at an incident ion bombardment angle of 45^{o} while the EVOLVE calcualtions described here were run at normal incidence. It is well known[54] that the total sputtering yield is highly sensitive to bombarding ion angle of incidence, so it is likely that the angular yield may also be affected. Indeed, grazing angles of incidence would be more likely to cause atoms to sputter into the normal exit direction than a normally incident ion beam which would not be expected to produce many sputtered atoms exiting in its direction of impact. The other explanation for the discrepency in the cosine dependence may stem from physical effects not modelled by the EVOLVE code. Kelly[55] has argued that preferential normal emmision of one species over another in a binary alloy is due to bombardment induced Gibbsian segregation as opposed to mass-related trajectory differences. In this view, bombarded In-Ga alloy should give a narrower angular distribution for Ga, as was observed by Dumke et al., since Ga is the non-segregating species. Since EVOLVE does not model the Gibbsian effects of

ion-induced segregation, EVOLVE calculations may be used to estimate the extent of influence of this effect on the angular distribution of sputering yields in the eutectic alloy system studied, assuming the correctness of the model of Kelly.

Lastly, it is well known that sputtered particles originate predominantly from the first few atom layers of the target. The displacement energy model employed in this study produced this basic feature. The fractional contribution to the total yields for the first four layers calculated by EVOLVE was .44, .13, .12, and .06 for the In/Ga target. This gives a drop of 1/e in the first three atom layers.

E. CONCLUSION

A depth dependent displacement energy model was introduced in this study. From use of this model, it is concluded that variation in the dependence of the displacement energy affects the sputtering yield; the modeling used providing agreement with experimental observations.

The depth dependent displacement energy model also gave a reasonable variation of sputtering yields with depth. In addition, this modeling demonstrated increasingly peaked angular distributions as the depth of origin was increased.

IV. LOGISTIC INTERFACE PARAMETERIZATION

A. Introduction

The process of sputtering, investigated in detail in Chapters II and III, has found significant use as an analytical tool when used in conjunction with analytical surface techniques such as Auger electron spectroscopy (AES) and Secondary Ion Mass Spectroscopy (SIMS). Though sputtering is a destructive process, useful information can be obtained by examining Auger electron spectra as the surface is successively removed by ion bombardment. Typically, detectable Auger electrons escaping the surface of a solid are emitted from atoms at depths seldom greater than three atomic layers. For this reason, a measurement of the intensity of characteristic elemental Auger electron spectra, taken periodically as the surface recedes due to sputtering, provides a profile of the composition versus sputtered depth of a multicomponent solid, i.e. an Auger sputter depth profile. This type of analysis may be used to measure the composition profile of a relatively uniformly mixed elemental target, such as an alloy, or of a target where the elements have been separated into distinct layers during the fabrication process. In the latter case, the transition region between two distinct elemental layers is referred to as an interface.

The interface between two dissimilar materials as studied by sputter depth profiling exhibits a composition distribution through the interface region that depends upon the sputtering conditions as well as upon the nature of the undisturbed interface. Processes such as surface roughening, cascade mixing, and diffusion limit the resolution with which interfaces can be characterized through sputter depth profiling and contribute to an apparent interface distribution that can mask the nature of the true interface. The depth resolution of sputter profiling has been the subject of extensive theoretical and experimental studies [56-60], but as yet little attention has been paid to the systematic parameterization of observed changes across the interface region for the purposes of comparison of different measurement techniques or different materials. In this chapter we present a systematic parameterization which has proved to be superior to previously available characterizations.

Previous work has focused on the development of theoretical models for the characterization of depth profiles. Ho and Lewis[61] developed an expression for the true depth profile in terms of a convolution integral involving the actual measured profile. This approach treated the depth profile as a series of thin slab segments, each suffering ion induced broadening independently. The contributions from each of the slabs were summed to form the actual profile. Sanz and

Hofmann[62] extended this model to derive an expression for the composition versus depth depth profiles of thin oxide films in terms of exponential functions of the sputtering time. A similar approach was adopted be Seah and Leah[63], who attempted to describe the shape of depth profiles employing a convolution integral utilizing an exponential function of the sputtered surface position in the integrand. To model the broadening of interface regions with depth, Seah et. al.[64] developed an expression consisting of error functions of the sputtered depth summed for each successive interface to define an entire multilayered normalized Auger intensity depth profile.

A more rigorous attempt to reliably charaterize interface regions was presented by Marton et al[65] . These authors utilized the concepts of Ho to develop an interface Parameterization in terms of error functions. Describing the diffusional broadening during depth profiling with exponential functions, the true profile shape was generated by integrating over a series of infinitely thin slabs to produce an error function. To model real profiles, however, it was necessary to employ sums of complementary error functions, thus introducing an additional level of complexity to the analysis. In terms of this model, Giber et al.[66] described the depth resolution, Δz, in terms of the inverse error function of linear superpositions of error function profiles.

These approaches all tend suffer from instabilities and an inability to handle poorly structured data. Moreover, because the functions employed are tabulated and not analytic, these techniques tend to be cumbersome and time consuming in their use. By contrast, proprietary interface analysis software, available through analytical surface instrument manufacturers, employs various smoothing procedures and straight line approximations which, though easily and inexpensively utilized, do not result in a thorough and complete functional description of the profile shape.

The interface-analysis program LOGIT, described in this chapter, provides a complete and accurate characterization of the interface region. Use of this algorithm results in a simple, convenient, rapid, and reliable analysis. The choice of the logistic function, described below, along with a specifically written least-squares procedure provides statistically evaluated parameters describing the asymmetry, width, and midpoints of interface profiles in a reproducible and unambiguous way.

Further, LOGIT employs a physically plausible model of the interface region and is superior to other functions (e.g. polynomials and error functions) in that it contains the minimum number of parameters for describing interace shapes. An additional important feature of LOGIT is its ability to make its own initial estimates of the parameters, allowing it to run without operator intervention. As the functional form employed

by LOGIT is ideally suited to the description of real interfaces, the program has proved robust in the handling of a wide variety of real data of sigmoidal character and is capable of dealing with extremely sharp profiles, noisy data, and pronounced outliers with a speed improvement factor of from 10 to 100 over less automated-methods.

The program LOGIT, which is described in this chapter, was originally written by Dr. William Kirchhoff of the National Bureau of Standards for the analysis of phase transitions of chemical thermodynamic data. Under the direction of Dr. Kirchhoff, the author developed and adapted this program to the parameterization of Auger depth profile data. In addition, the author integrated this software into an automated computer data analysis system for the evaluation of Auger spectral data. Lastly, the author performed the study to determine the success, accuracy, and applicability of this analysis software to the evaluation of Auger depth profiles.

B. Mathematical Development

The appearance or disappearance profiles of elemental surface concentrations at an interface between two layers as observed by sputter profiling have a sigmoidal shape that can be characterized by a cumulative logistic distribution. In its simplest form, the logistic distribution is given by

$$y = 1/(1+e^{-cx}) \qquad (4.1)$$

If c is positive, equation 4.1 represents a growth curve from y=0 to y=1 as x increases through the origin. If c is negative, equation 4.1 represents a decay curve. The differential form of equation 4.1.

$$dy/dx = y' = c/(1 + e^{-cx})(1 + e^{cx}) = cy(1 - y), \qquad (4.2)$$

has a shape very similar to a Gaussian but with longer tails. The similarity in shape between the Gaussian and logistic distributions has been responsible for the popularity of the latter in statistical applications where its analytical simplicity was a distinct advantage before the availability of computers. The logistic function is also encountered in the representation of a variety of physical and chemical phenomena, most notably in autocatalysis.

In the analysis of sputter depth profiles, we have used an extended form of the logistic function, namely

$$Y = [A + a(T - T_o)]/(1 + e^{x}) + [B + b(T - T_o)]/(1 + e^{-x}) \qquad (4.3)$$

where

$$x = (T - T_o)/D. \tag{4.4}$$

In these equations, Y is a measure of the elemental surface concentration as determined from the Auger electron intensity of surface atoms. The variable T is a measure of depth and is usually taken to be the time, assuming a constant sputtering rate, at which the Auger electron intensity was measured. The variable T_o is the apparent midpoint of the interface profile. The expression $[A + a(T - T_o)]$ is defined as the preinterface asymptotic limit and the expression $[B + b(T - T_o)]$ as the postinterface asymptotic limit of the appearance or disappearance profile. The parameter D is a scaling parameter that defines the breadth of the interface region. In particular, the time required for the decay or growth curve to progress from a fraction f of completion to (1 - f) of completion is proportional to D and given by the simple formula

$$T_f = 2D\log[(1 - f)/f], \tag{4.5}$$

so that, for example, the traditional 10% to 90% interface width is 4.39D. Another measure of the width of the interface region is the time interval between the intercept of a line

drawn tangent to the profile at $T = T_o$ with its pre- and postinterface asymptotes. This width is given by

$$T = 4D / (1 + 4d^2) \qquad (4.6)$$

where $d = D(b - a)/(B - A)$.

The slopes of the asymptotic limits, a and b of equation 4.3, have been included in the model in order to account for possible instrumentation or matrix effects on the measured intensity. Ideally these slopes should be zero. Deviations from zero may be used to test for uncontrolled or unexplained instrumental effects or significant departures from an ideal interface. One of the two asymptotes is expected to be zero corresponding to the disappearance of that one of the two materials from the surface. However, both asymptotes are allowed to vary during this least squares fit to the model in order to test for statistically significant deviations from expected behavior.

In practice, the shapes of the interface profiles are found to be asymmetrical. That is, the curvature is greater at one end or the other of the interface region. In order to obtain a measure of the difference in curvature of the pre- and postinterface regions and to test for its statistical significance, equations 4.3 and 4.4 have been modified to allow

the scaling parameter D to vary logistically through the interface region

$$D = 2D_o/[1 + e^{Q(T - T_o)}], \tag{4.7}$$

where Q is defined as the asymmetry parameter. If Q = 0, the interface profile is symmetric and $D = D_o$. If Q < 0, then D varies from 0 to $2D_o$ as T varies from $<< T_o$ to $>> T_o$ giving a sharp preinterface curvature and a broad postinterface curvature. If Q > 0, then the postinterface curvature is sharper. Since different processes can be distinguished by determining whether the outer material at the interface is distributed to a greater depth into the underlying material than vice versa, the sign and magnitude of Q and its statistical significance may be useful for distinguishing among the different physical factors contributing to the observed interface profile. Other means of incorporating asymmetry in an analytical expression for the interface profile are possible, but equation 4.7 has proven to be quite satisfactory in recent application so long as Q is small compared to $1/D_o$, that is, so long as the dimensionless quantity QD_o is small compared to unity.

The introduction of the asymmetry parameter into the extended logistic function makes the calculation of the 10%

and 90% points of the interface more complicated than equation 4.5. In particular, for fractions f and 1 - f of completion of the interface transition,

$$T_f = T_o + 2D_o \log[f/(1-f)]/[1 + e^{Q(T_f - T_o)}] \quad (4.8a)$$

and

$$T_{1-f} = T_o + 2D_o \log[(1-f)/f]/[1 + e^{Q(T_{1-f} - T_o)}]. \quad (4.8b)$$

The quantities T_f and T_{1-f} can be evaluated most readily by Newton's method of successive approximations.

C. Data Analysis Programs

Two companion computer programs have been written in FORTRAN for the analysis of EN(E) Auger sputter depth profile data. The first of these, GAUFIT, is used to determine the intensities of Auger spectral lines by performing a least squares fit of the spectral data to a Gaussian line shape. The second, LOGIT, performs a least squares fit of the elemental surface concentration (as represented by the Auger intensities) versus depth (time, assuming a constant sputtering rate) to equation 4.3 as modified by equations 4.4 and 4.7.

In order to analyze Auger spectral intensities, it is first necessary to perform a background subtraction on the spectra. Figure 4.1 (a) displays an Auger EN(E) spectrum taken from the first layer of a Cr/Ni multilayered thin film structure. The peak appearing in the bottom left portion of the spectrum represents the LMM Auger chromium peak. The solid line represents an extrapolated background under the peak produced by a linear least squares fit to an exponential function of the form $Y = \alpha e^{-\beta x}$, where α and β are fitting parameters. Though many trial functions using more parameters were tested, this simple function was found to provide the most reliable and consistent description of the spectral background region in the case of both a large peak present as well as in the case of no detectable peak present as demonstrated in the upper right portion of the figure. The exponential function is applied in the region where the Ni peak is expected, however, as there is no Ni present in this layer of the thin-film structure, there is no observable peak in this region. Notice that the solid line exponential fits this spectral intensity data nicely.

The fit is obtained by first taking the logarithm of the intensity data in the designated background region above the peak and fitting it to a linear equation. The parameters from this fit are used to construct the exponential background which is extrapolated to the region beneath the peak. This

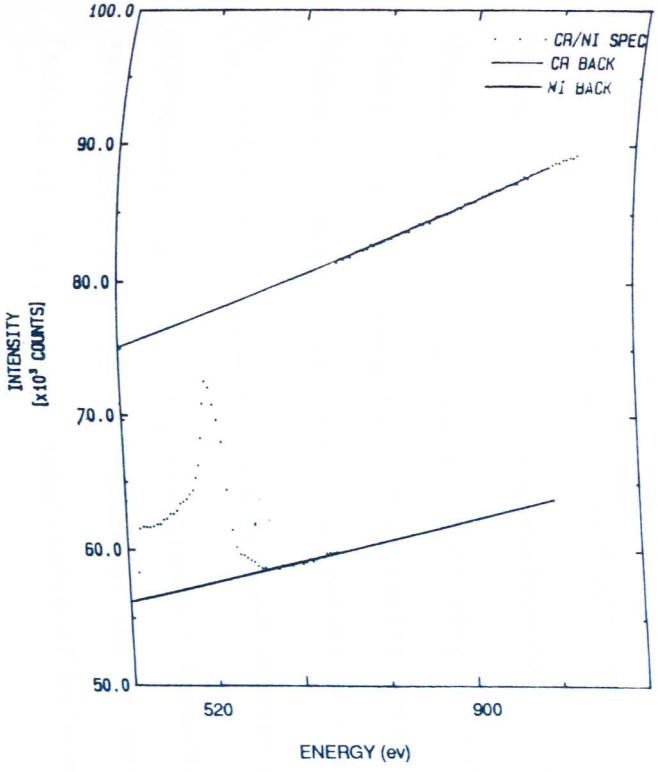

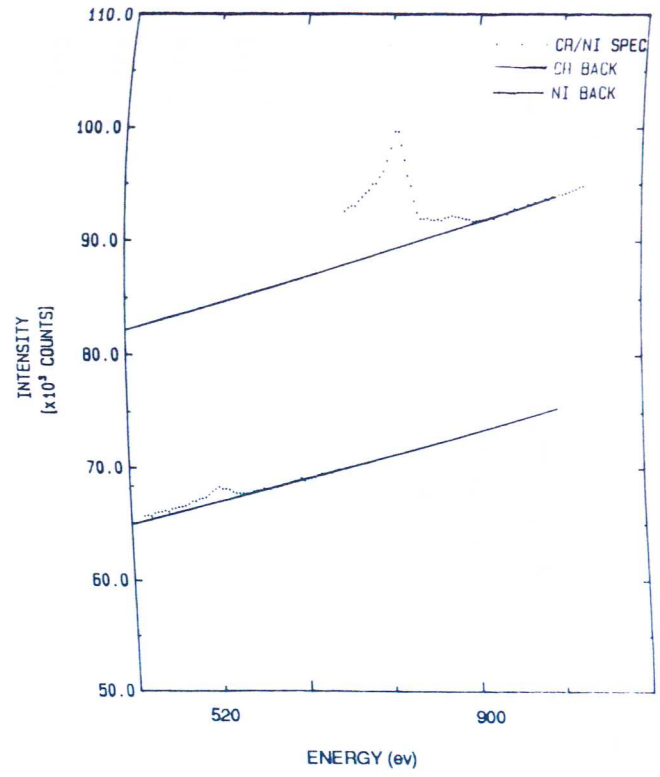

Figure 4.1 (a) Auger EN(E) spectrum from first Cr layer of a Ni/Cr multilayered thin film structure. The solid lines represent least-squares fits to exponential background regions. In this spectrum, the Cr peak (lower left) is prominent while the Ni peak (upper right) is negligible or nonexistent. (b) Auger EN(E) spectrum at the first Cr/Ni interface. Solid lines represent least-squares fits to exponential backgrounds. In this spectrum, the Cr peak has subsided while the Ni peak has come into prominence.

background is subsequently subtracted leaving a skewed guassian looking line shape. Figure 4.1 (b) shows the extrapolated background (solid line) passing under the Cr peak (lower left) and the Ni peak (upper right) of the spectra recorded slightly beyond the first interface region of a multilayered thin film structure.

In order to measure the intensity of an Auger spectral line, data near the apex (generally within the upper 20% of the maximum intensity) of each spectral feature are, following the background subtraction, fit by least squares to a Gaussian function

$$I = I_o \exp(- [(X - X_o/S]^2) \qquad (4.9)$$

where I is the intensity at an electron energy X. The quantity X_o is the electron energy at the Auger line maximum, S is the width parameter and I_o is the maximum Auger line intensity whose value is being sought. Following an initial linearization of equation 4.9 by taking logarithms of both sides in order to obtain initial values of the parameters I_o, X_o, and S, the parameters are refined through successive approximations by fitting equation 4.9 expanded as a Taylor series about the current values of the parameters. A unique feature of GAUFIT is the maintenance of reference values for

X_o and S for each of the spectral features. The reference values are updated each time the parameters I_o, X_o, and S are determined. When a particular peak is very weak or nonexistent, the reference values of X_o and S are introduced as data, weighted by the inverse square of their uncertainties. This procedure prevents wild excursions when the data would otherwise appear to be on the wings of a distant, intense Gaussian line shape. The reference values are maintained in such a way that the influence of earlier measurements is diminished by 10% each time a new spectrum contributes to the reference values. This allows the reference values to track slow drifts in the spectral parameters. This technique of introducing final fitted parameters from previous spectra as initial guesses for the analysis of current spectra has been demonstrated to be superior in practice to more generalized fitting programs which tend to be highly unreliable when used to fit data with no discernable peak. Auger intensity data obtained using GAUFIT can subsequently be converted into elemental surface concentration values for depth profile analysis.

The code LOGIT also follows an iterative approach in which equation 4.3 as modified by equations 4.4 and 4.7 is expanded in a Taylor series about the current values of the seven parameters A, a, B, b, T_o, D_o, and Q. A linear fit of Y(obs) - Y (calc) is then performed from which linear

corrections to each of the seven parameters are obtained. The values of the parameters are updated and the procedure is repeated until the corrections to the parameters are small compared to the standard deviations of the parameters. Generally, the values of I_o obtained from GAUFIT are used directly and without modification as the values for Y (obs) in LOGIT.

A special feature of LOGIT is the manner in which the program deals with data sets having few values in the interface region. First, a transition interval is defined as the interval in T in which values of Y(obs) differ from each asymptote of equation 4.3 by more than two standard deviations. The asymptotes of equation 4.3 are

$$Y = A + a(T - T_o) \tag{4.10a}$$

and

$$Y = B + b(T - T_o) \tag{4.10b}$$

and the standard deviation used for the comparison of Y(obs) with the asymptotes of equation 4.3 is the standard deviation returned by the least squares fit divided by the square root of the weight given to each Y(obs) tested. The number of data for which Y(obs) differs from each asymptote by more than two

standard diviations is counted. If no data fall within the transition interval, T_o is assigned a value midway between the two data spanning the transition interval. D_o is estimated from the standard deviation of the fit, the separation between the two asymptotes, and the separation between the two measured values of T spanning the transition interval, while Q is held fixed at its most probable value. If two data values fall within the interval, D_o and T_o are allowed to vary in the least squares fit, but Q is held fixed at 0. If three or more data values fall within the interval, T_o , D_o, and Q are all allowed to vary.

The routine LOGIT also contains a provision for identifying outliers. Following calculation of the least squares fit, the standardized residuals for each of the data are calculated. The standardized residuals are given by

$$R_i = [\, Y_i(obs) - Y_i(calc)] \,/[S^2/W_i - s(calc)^2]^{1/2} \qquad (4.11)$$

where s is the standard deviation of the fit, $s/\sqrt{W_i}$ is the standard deviation of Y(obs), and s(calc) is the standard deviation of Y(calc) at $T = T_i$. This latter quantity is calculated from the variance-covariance matrix returned by the least squares fit. The second minus sign in equation 4.11

arises from the correlation between the standard deviations of Y(obs) and Y(calc) resulting from the use of Y(obs) in the calculation of Y(calc). The values of R, are the number of standard deviations by which each Y(obs)-Y(calc) differs from its expected value of 0. The R, should follow a student's t distribution. Values of R greater than 3.0 are regarded as outliers and the data are refit dropping the outliers from the fit, although their values are printed in the data listings accompanying each fit. Since the asymmetric fitting routine occasionally has trouble dealing with extremely outlying data points, it is first necessary to perform a symmetric fit, ie. holding Q fixed at zero, to identify and eliminate troublesome outliers. The program proceeds to the asymmetric fit only after the symmetric fit has eliminated all pronounced outlying data points.

The uncertainties in the seven parameters and all functions derived from these parameters are obtained from the variance-covariance matrix, $VCV_{i,j}$, which contains all information about the quality of the fit and the correlation of errors among the parameters. In general, for a given function F of the parameters $C_k(A,B,a,b,D,T_o,Q)$, the variance (square of the standard deviation) is given by

$$s^2(F) = (dF/dC_k)VCV_{k,i}(dF/dC_i) \qquad (4.12)$$

where repeated indices imply summation over all k and i. The standard deviations of each of the determined parameters are given by the square root of the variance-covariance matrix diagonals. Thus the standard deviation of the dimensionless parameter Q*D, to be described later, is given by

$$s^2(Q*D) = D^2*VCV_{7,7} + (D*VCV_{4,7}*Q) + Q^2*VCV_{4,4} \quad (4.13)$$

which differs from the standard error summation formula due to the fact that the parameters Q and D are correlated.

The linear least squares algorithm used with GAUFIT and LOGIT is subroutine ORTHO which performs the least squares fit using a Gram-Schmidt orthonormalization procedure on vectors of the dependent and independent variables. Subroutine ORTHO is derived from a program originally written by Walsh[67] and extensively tested by Wampler[68]. The robustness of ORTHO, the provisions for dealing with a paucity of data in the interface region, the procedures for identifying outliers, and provisions for a number of postfitting tests on assumptions underlying the selection of parameters to be held fixed, have resulted in a least squares fitting procedure that has been successful in the analysis of a wide variety of data structures.

The codes GAUFIT and LOGIT have been extensively documented and the subroutines and their documentation are available from the author.

D. Application to Auger Depth Profiles

We have analyzed a large number of interfaces and have found that equation 4.3 as modified by equation 4.7 fits our data in every case tested to within the estimated measurement uncertainty, approximately 1%. The results of fitting data collected in the region of a typical interface between chromium and nickel are presented in Figure 4.2. Casual inspection of Figure 4.2 would suggest that data in the interval have greater precision than data in either of the asymptotic regions. This is an illusion brought about by the pronounced slope in the interface region masking vertical deviations. Inspection of the values of Y(obs) - Y(calc) for the same data, presented in Figure 4.3, shows a random distribution throughout the asymptotic and transition regions. In Table 4.1 the values of the parameters derived from the analysis of the data in Figure 4.2 are presented. A plot of a chromium disappearance profile with the seven fitting parameters shown in their corresponding geometrical regions of influence is presented in Figure 4.4.

For comparison, we have also tested the logistic fit on synthetic data generated from the error function shown in Figure 4.5. As stated in the Introduction, the logistic function and the error function (the cumulative Gaussian function) are similar in shape. Further, error functions have previously been used to describe broadening of metal/metal interfaces during sputter depth profiling by several authors,

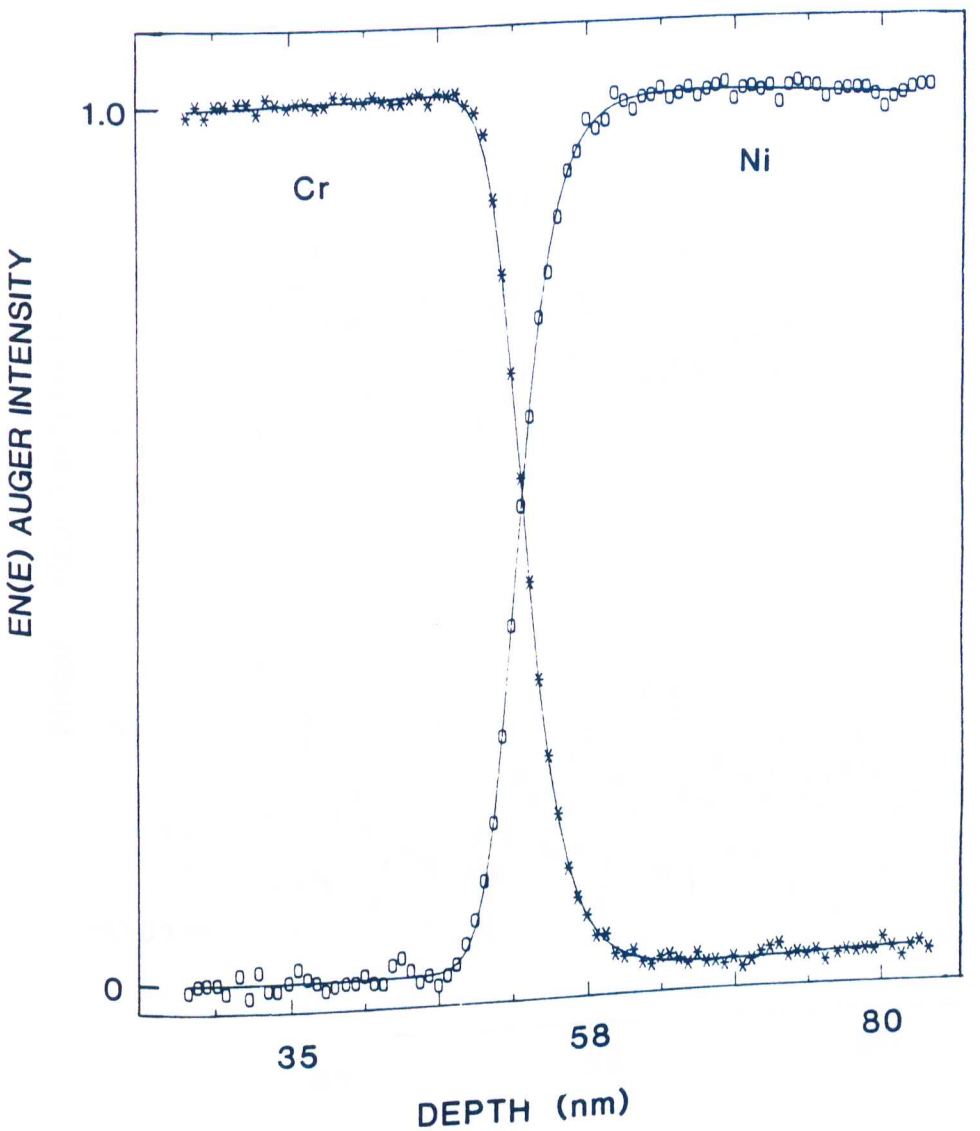

Figure 4.2 Typical depth profile of chromium through a chromium (x) and nickel (o) interface. The solid lines are the calculated values from Eq. 4.3 as modified by Eq. 4.7. Parameters of the fit are given in Table 4.1.

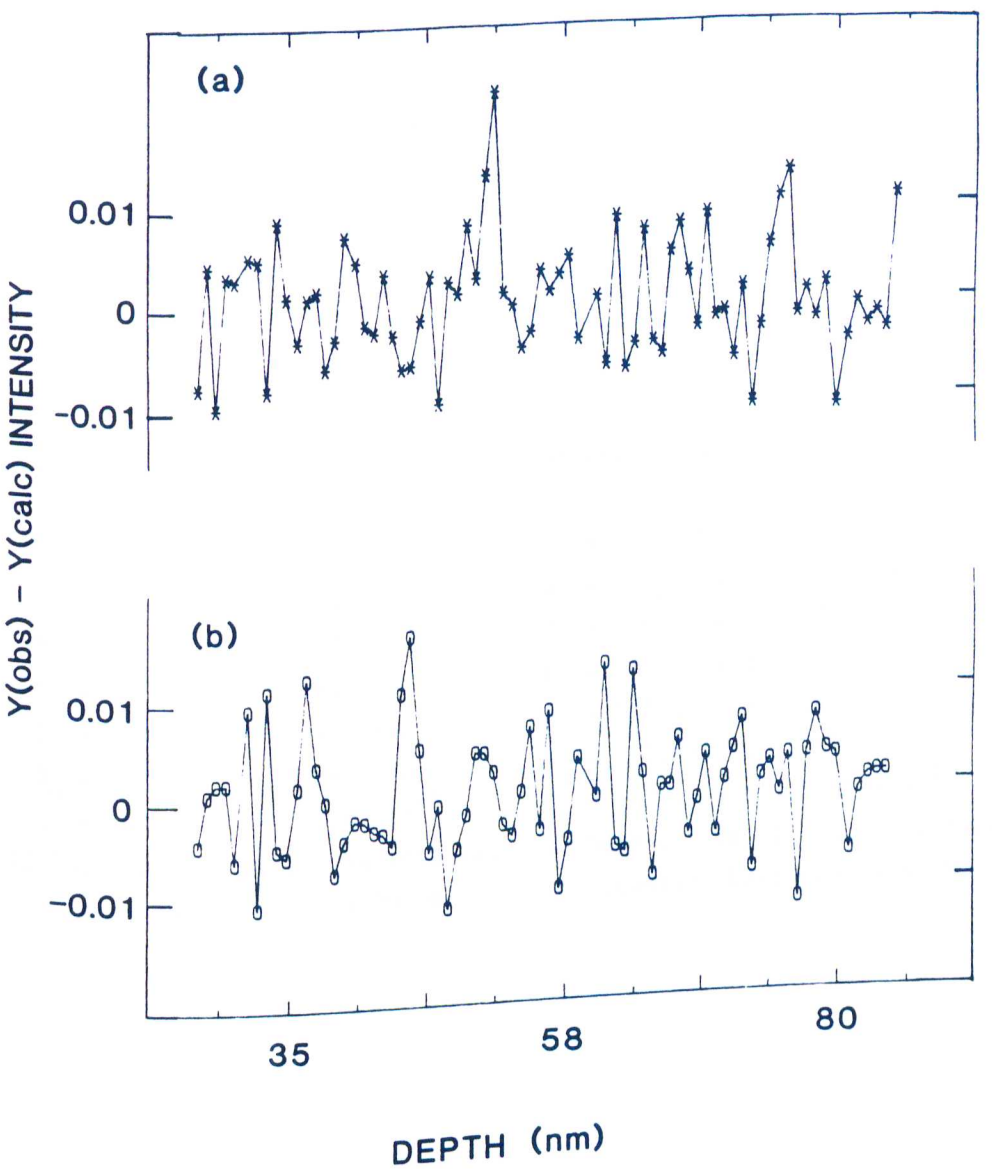

Figure 4.3 Plot of Y(obs) - Y(calc) for the data depicted in Fig. 4.2 as a function of depth (time): (a) disappearance profile for chromium, (b) appearance profile for nickel.

Table 4.1 Profile parameters for a typical chromium/nickel interface.

Chromium (Disappearance Profile)

$A = 14893.00 \pm 42.78$

$a = 4.59 \pm 1.32$

$B = -167.68 \pm 69.07$

$b = 4.43 \pm 1.81$

$T_o = 108.24 \pm 0.04$ min

$D_o = 2.862 \pm 0.034$ min

$Q = -0.0451 \pm 0.0056$ min^{-1}

72 Data points, 20 in the interval

Standard Deviation = 79.06

Nickel (Appearance Profile)

$A = -87.80 \pm 47.48$

$a = 1.65 \pm 1.46$

$B = 10656.14 \pm 72.91$

$b = -2.19 \pm 1.90$

$T_o = 107.30 \pm 0.04$ min

$D_o = 2.801 \pm 0.052$ min

$Q = -0.0470 \pm 0.0080$ min^{-1}

73 Data points, 18 in the interval

Standard Deviation = 89.90

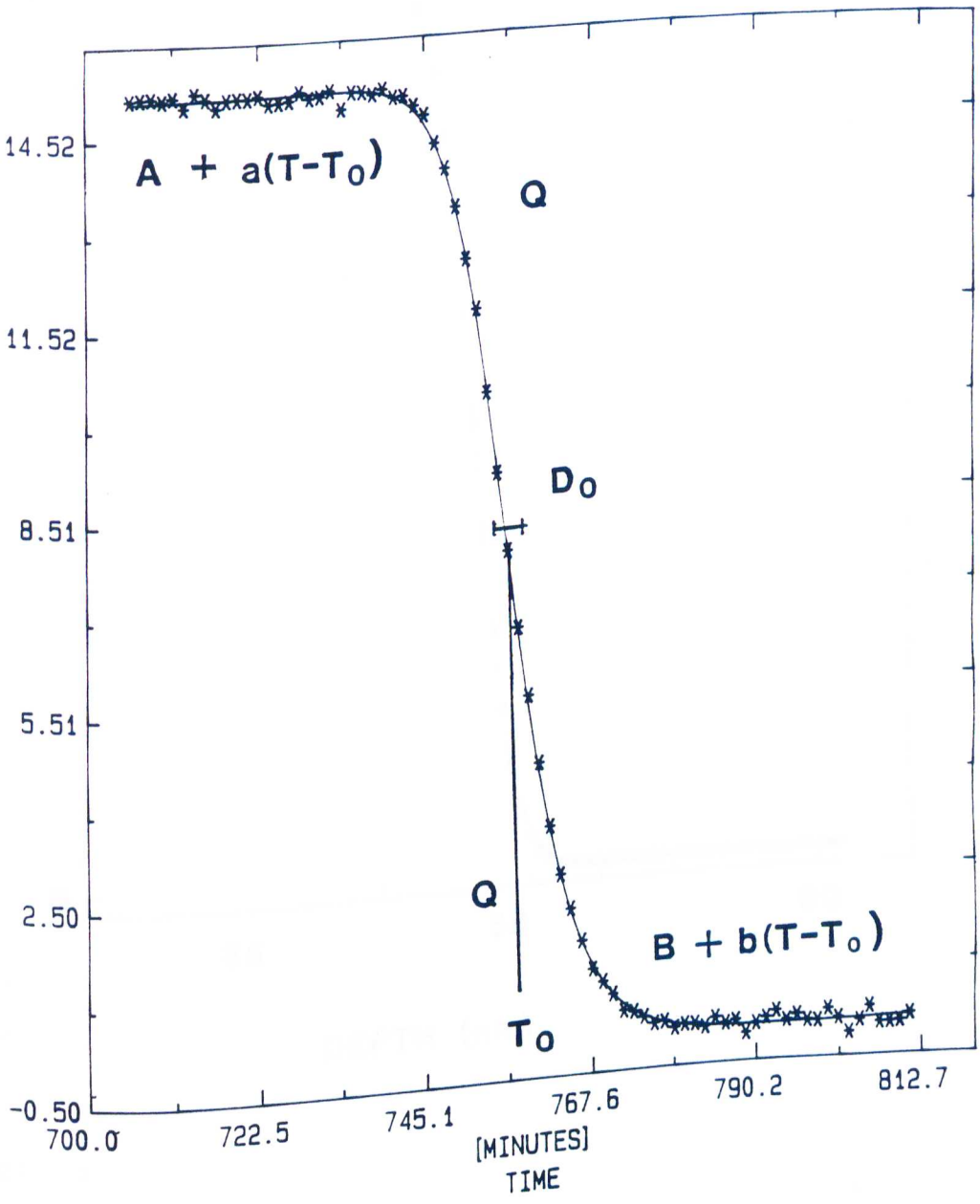

Figure 4.4 Auger depth profile of a Cr/Ni interface(*) with logistic fit (solid line). The logistic parameters are shown in their corresponding geometrical regions of influence.

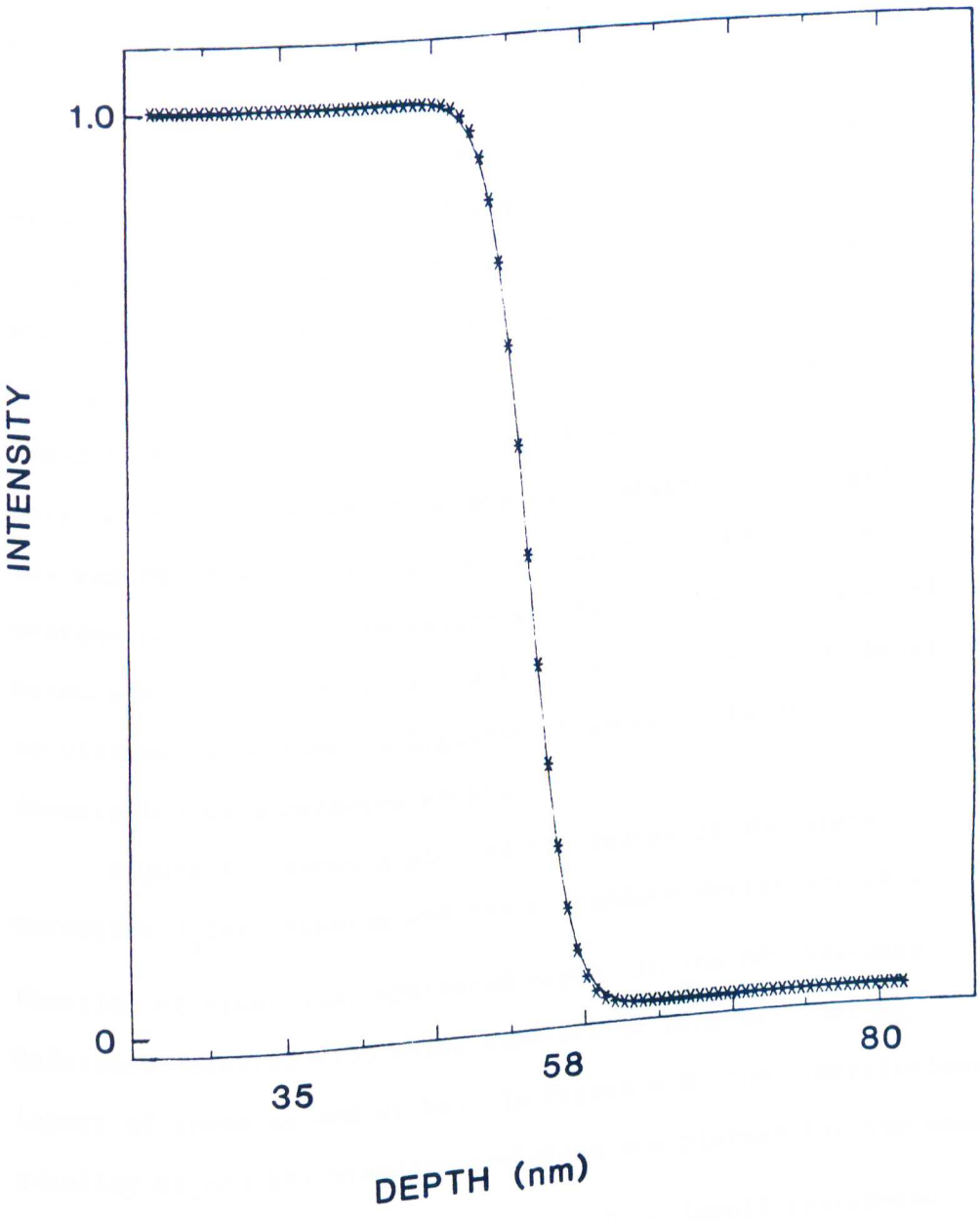

Figure 4.5 Plot of the fit of the logistic function (Eq. 4.3) to an error function (*) (solid line).

as has been discussed earlier. The standard deviation returned by the fit of the error function data was approximately half that obtained in the fit of actual interface data. Inspection of a plot of the values of Y(obs) - Y(calc) shown in Figure 4.6(a), reveals a pattern characteristic of a systematic error. When random, normal errors with a standard deviation comparable to the measurment uncertainty for actual interface data were added to the error function data and the combined synthetic data refit, the systematic error was completely submerged into the random error as can be seen in Figure 4.6(b). A direct consequence of this observation is that at the current level of measurement accuracy, approximately 1%, it will not be possible to distinguish between a logistic or an error function description of a measured profile.

Figure 4.7 shows a plot of the values of the width parameter D_o for chromium and their standard deviations as a function of time, i.e, sputtered depth, in the NBS Standard Reference Material 2135 which consists of nine alternating layers of chromium and nickel. In Figure 4.8, the dimensionless quantity QD_o and its standard deviation are plotted for the same data. Because the asymmetry parameter Q is itself introduced logistically through multiplication by $(T - T_o)$, Q values are artificially smaller for broader interfaces, given the same level of true asymmetry, than for narrower interfaces. For this reason, it is necessary to scale the parameter Q by the

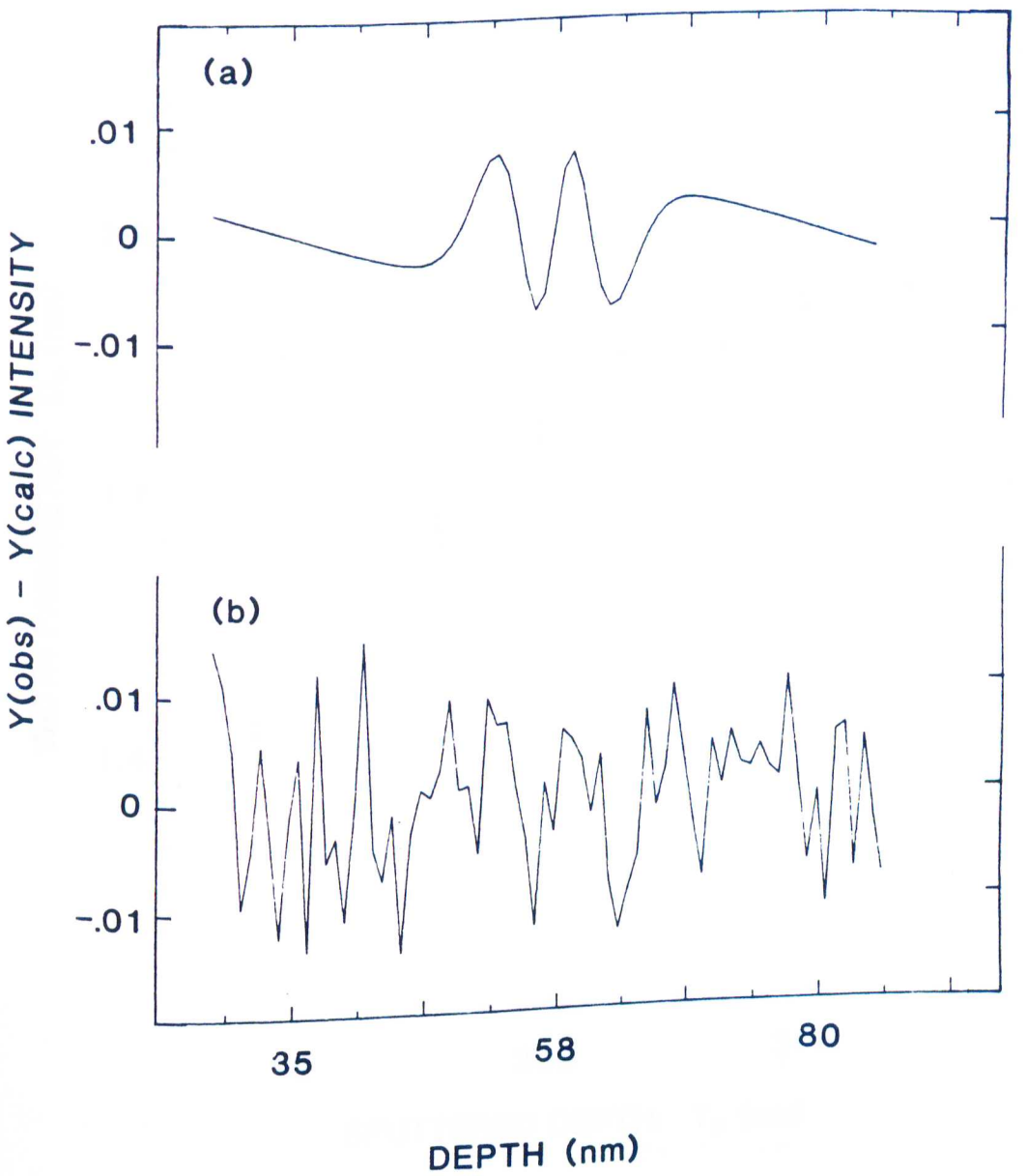

Figure 4.6 Plot of Y(obs) - Y(calc) for the fit of an error function to the logistic function of Eq. (3): (a) the error function alone, (b) the error function plus random normal errors with a standard deviation comparable to that of the data depicted in Fig. 2.2.

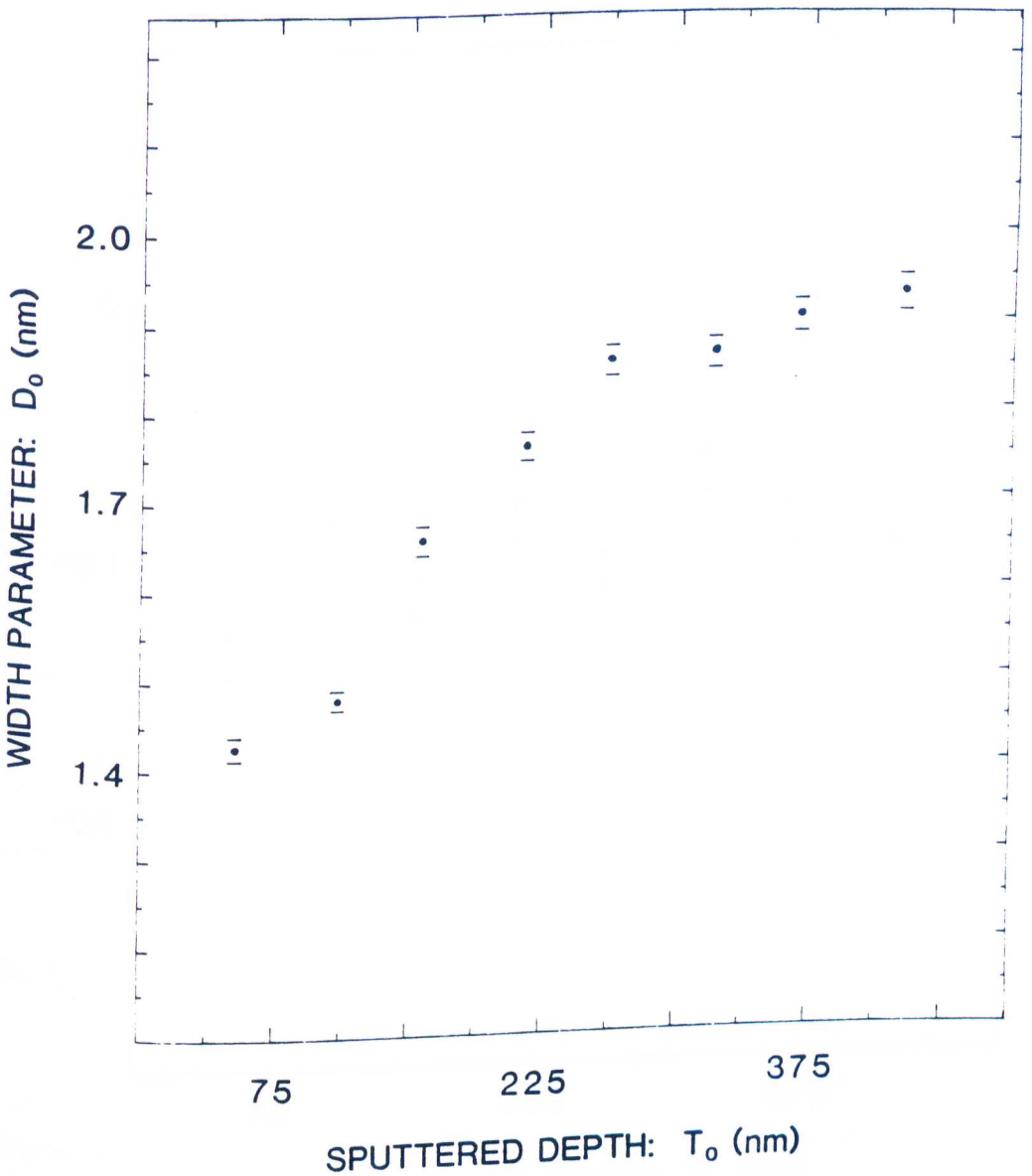

Figure 4.7 Plot of the width parameter D_o vs T_o for chromium in a sample consisting of alternating layers of chromium and nickel; the values of these parameters have been converted from dimensions of time into dimensions of length (nm). Uncertainty bars represent one standard deviation.

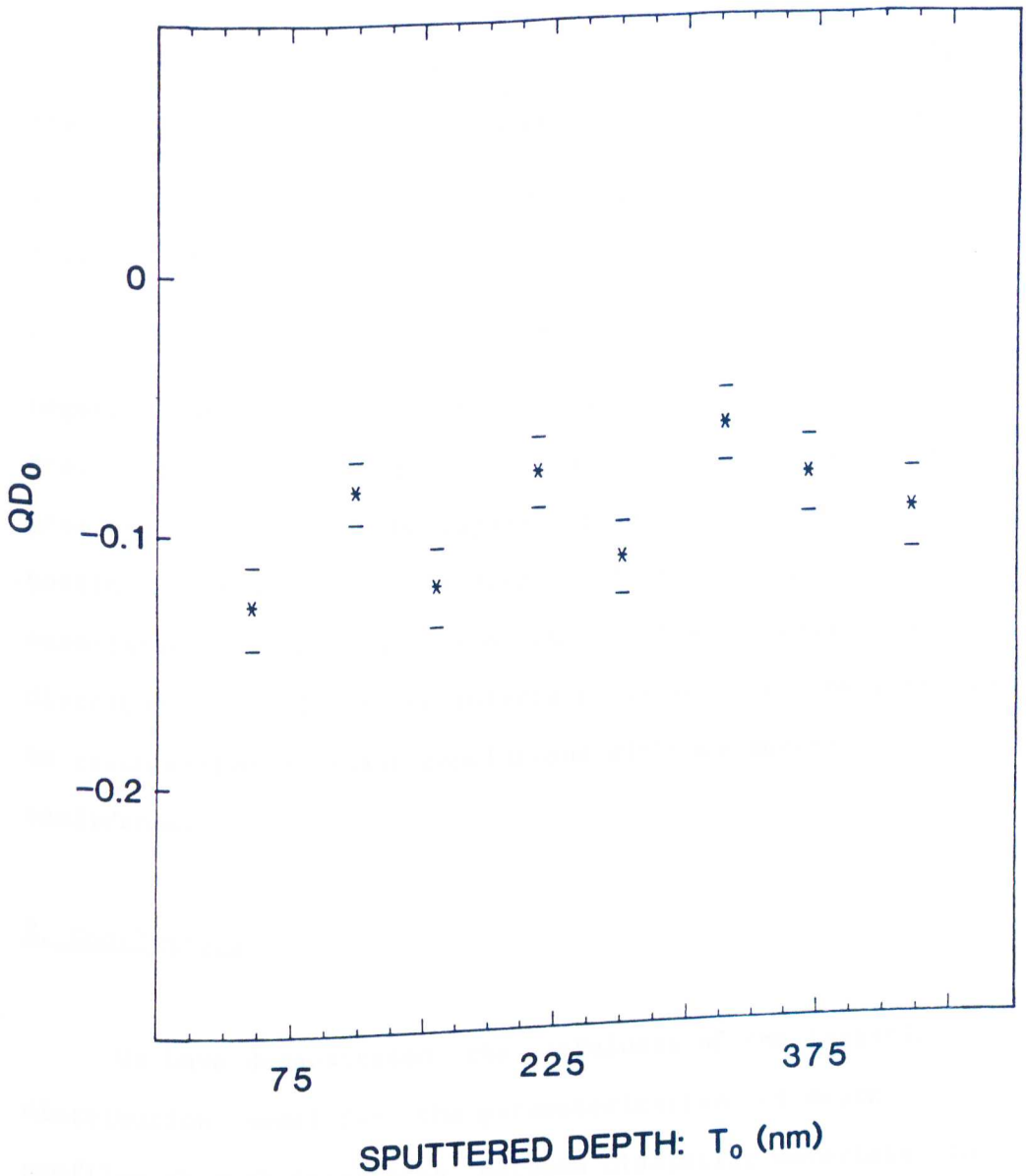

Figure 4.8 Plot of the dimensionless quantity QD_o vs T_o (sputtered depth) for chromium in a sample consisting of alternating layers of chromium and nickel.

interface width D_o to obtain a meaningful representation of the interface asymmetry. As can be seen from these two figures, the width of the interface D_o shows a statistically significant increase with depth, possibly leveling off at the deeper levels. While the dimensionless quantity QD_o does not show a corresponding trend with layer depth, the sign of QD_o is always negative, demonstrating a statistically significant sharper preinterface curvature for every interface. This implies a greater dispersion in the apparent interface on the postinterface side. Without display of the statistics associated with the analysis of the profile in terms of a distribution model for the interface, it would not be possible to reach either of these conclusions with any degree of confidence.

E. Conclusions

We have demonstrated the usefulness of the logistic distribution model for the parameterization of depth profiles through interfaces between dissimilar materials. In all cases analyzed thus far, the data fit the logistic distribution to within measurement uncertainty. At the current level of measurement accuracy, it is not possible to distinguish between a logistic distribution and an error function distribution. The least squares fitting program

written to analyze measured interface profiles in terms of the parameters of the logistic distribution has proven to be robust and capable of analyzing all of the profiles tested so far without the need for providing the program with initial estimates of the parameters. The parameterization of the interface profile should prove most useful in comparing measurements made with varying experimental conditions and in comparing measurement with computer simulation of surface sputtering. The statistics of the least squares fit will allow the statistical significance of these comparisons to be evaluated.

V. DEPENDENCE OF INTERFACE DEPTH RESOLUTION ON ION BEAM PARAMETERS

A. Introduction

The profile of composition vs depth at virgin solid/solid interfaces is at present difficult to determine using sputter depth profiling techniques. Sputter profiles obtained at presumably abrupt interfaces often show significant interface broadening - composition vs depth is no longer a steplike function. Those factors which contribute to this broadening, especially at sputtered depths greater than a few tens of nanometers, are mostly related to material redistribution at the interface resulting from the bombardment process; they include cascade mixing, recoil implantation, surface topography change and radiation enhanced diffusion. Although there are a number of excellent reviews which discuss sputtered interface resolution[69-75], there has been a need for a thorough exposition of the role which ion bombardment parameters play in interface profile broadening.

A careful evaluation of bombardment parameters, such as ion beam energy, angle of incidence, and current density, as well as sputtered depth, on interface resolution has not been previously available for any given set of interface materials.

While some data of this type does exist[76-83], most of it consists of uncorrelated measurements made on different materials [75,84]. It is the purpose of this chapter to describe a consistent set of measurements obtained for the above ion bombardment parameters, examining interfaces of thin films of Ni and Cr using Auger spectroscopy.

Depth profiles of multilayered Ni/Cr sandwich structures have been previously described by Hofmann et al[77]. These authors used alternating layers (each 37 nm thick) of Ni embedded in layers (each 11.5 nm thick) of Cr. These elements were chosen because of the similarity of their sputtering yields[85]. Hofmann et al. observed that the Ni/Cr interface region exhibited an observable broadening trend with increasing sputtered depth, i.e. layers embedded deeper in the sample exhibited broader interfaces than layers lying closer to the surface. Hofmann had predicted this result on theoretical grounds in a previous study[86]. Because of the similarity of the sputtering yields of Ni and Cr and the use of low energy (1-keV) ions at normal incidence, Hofmann was able to neglect the distorting effects of preferential sputtering and casade mixing and conclude that the increase in interface broadening with sputtered depth was due to the buildup of surface micro-structure during the sputtering process.

In a follow-up study, Hofmann and Zalar[78] compared the effects of 1-keV Ar^+ bombardment to N_2^+ bombardment of Ni/Cr multilayered structures. This study showed that in both cases the dependence of interface resolution on depth could be approximated by a $z^{-1/2}$ law using a simple sequential layer sputtering model. To determine the dependence of depth resolution on the sample materials, Seah and Jones[58] performed low energy (3-keV) Argon ion bombardment on multilayered silver, gold, and tantalum films. Scanning Electron Microscopy (SEM) was employed, both before and after ion bombardment, to determine the development of surface roughening due to sputtering. The increase in interface broadening was found to be due to the development of surface microstructure and not to atomic mixing. The magnitude of the roughening was found to be proportional to the sputtering yield of the sample materials; highest for high sputtering yield materials such as silver and gold, for the same energy, but lower by a factor of 3-5 for the low sputtering yield element tantalum. By contrast, the authors found that roughening effects, and consequently interface broadening, were negligible for thin-films of amorphous oxides of silicon and tantalum. The authors concluded that the development of surface roughening during low energy ion bombardment was a highly materials dependent phenomenon.

These results were supported by an independent study conducted by Ferron and Vidal[87] on multilayered Si/Ta thin films. Utilizing Monte Carlo computer code simulations together with experimental AES depth profiling, these authors were able to reinforce the finding of Seah and Jones that interface broadening during sputter depth profiling was due to induced surface roughening for the case of tantalum.

To determine the effect of ion energy on interface resolution and to deconvolute the factors contributing to it, Davarya et al.[81] conducted a study on alternating multilayered Ni/Cr thin film structures utilizing experimental AES depth profiling techniques as well as Monte Carlo computer simulations. Using the code EVOLVE, described in Chapter II, Davarya et al. were able to show that the contribution to interface broadening due to preferential sputtering and cascade mixing, phenomena modeled by the EVOLVE code, were small compared to the actual interface broadening observed experimentally. Assuming that the mechanisms contributing to the total interface resolution could be summed in an r.m.s fashion, these authors were able to quantitatively separate the broadening effects due to surface roughness from those due to other effects. In addition, Davarya et al. reported a clear effect of increased interface broadening with increased incident ion energy.

To explain the development of surface roughness during ion sputtering of solid targets, Marton and Fine[88] have proposed a simple statistical model. This model attributes the development of surface microstructure to different sputtering rates of differently oriented crystallographic surfaces in a polycrystalline solid. This model is able to successfully explain the square root dependence of the interface broadening on depth as well as the dependence on incident ion energy.

The research presented in this chapter, directed towards a complete and thorough investigation of the dependence of interface broadening on the experimental parameters, was performed under the overall direction and coordination of Dr. Joseph Fine of the National Bureau of Standards. The experimental study was performed by Dr. Fine, with the assistance of the author. The automated computerized data analysis and real-time experimental monitoring software used in this investigation were developed by the author. Raw data for the study of how interface broadening depends on angle of ion incidence were taken at the Perkin-Elmer Corporation. The analysis of this data was performed by the author.

B. Materials, Methods, and Measurements

As a consequence of the recent development by NBS of a Ni/Cr multilayered thin-film Standard Reference Material (SRM 2135) for depth profile analysis[89], sets of similarly fabricated specimens are now available. This systematic study was made of interface broadening using these multilayered standards. The samples reported on were taken from three separately produced batches of specimens: one batch was made as a prototype (or developmental) material while the two other batches were made, and have been issued, as NBS SRM 2135. The accurately characterized structure of all these materials provides a series of well-defined Ni/Cr interfaces of known spacings for analysis and makes possible a reliable intercomparison of results. These thin-film SRMs are composed of a total of nine metal layers with Cr forming the outermost layer; the average thickness for each Cr layer is 53 nm (38.0 ug/cm^2) and 66 nm (58.3 ug/cm^2) for each Ni layer. This structure provides 8 metal/metal interfaces at known depths for use in this interface resolution study.

The Auger sputter profiling results presented here were obtained with two separate instruments, both of which use the same type of ion gun but make use of different Auger data acquisition techniques. Sputter profiling was done in an ultra-high vacuum system using argon ions produced in an electron-impact-source differentially-pumped ion gun. The experimental procedure is as follows: the ion gun and electron energy

analyzer (cylindrical mirror type) are aligned so that the beam strikes the sample at the focal point of the CMA. This alignment is performed using a technique pioneered by Dr. Fine [90]. An SiO_2 target is positioned at the focal point of the CMA. A well defined beam of 3-keV electrons is scattered from this target and their energies analyzed by the CMA. When the target is aligned properly at the focal point, the elastically scattered 3-keV peak becomes prominent. At this point, the CMA is switched to a scanning electron mode to observe the target. A video image of the target is produced from the secondary electrons produced by the electron beam. The raster of this electron beam is synchronized with the sweep of the video monitor so that changes in the secondary electron current within the beam's characteristic footprint are converted to visual differences on the monitor. This change in secondary electron current results from the capture of free electrons by ions. Suitable deflection of the ion beam brings it to the focal point.

The focused beam of ions (~ 1 mm FWHM), although not mass analyzed, was rastered over an area of a few mm^2 to insure uniform erosion at the point of Auger analysis. The specific Gaussian features of the beam profile have an effect only at the edges of the sputtering region. Pressure in the chamber during depth profiling was about 2×10^{-8} Torr (base pressure <

5×10^{-10} Torr). In order to obtain precise interface profiles, much of the sputtering was done using low current-density ion beams (typically 100 nA in a 1 mm FWHM size beam). Auger electron energy spectra were acquired repetitively while the ion beam continuously bombarded the specimen. The amount of material sputtered during the time needed to acquire a Ni-Cr data point was small, in many instances only about 5 monolayers.

Auger analysis of the elemental surface composition was obtained in either the EN(E) or the dN(E)/dE mode depending on which instrument was used for a specific set of measurements. The EN(E) spectra of Ni(860 eV) and Cr(525 eV) were acquired sequentially using 100-MHz pulse-counting techniques with a multichannel analyzer and transferred to a microcomputer for analysis; a 2.5-keV primary electron beam (50 nA) was used to excite those spectra. The microcomputer executed a preliminary real-time analysis of the data by performing an exponential background subtraction, as described in Chapter IV, and fitting the resultant peak to a Guassian-type function employing a simple linear-least squares fitting routine. The resultant peak height intensities were sent to an external printing device. This allowed the experimenter to monitor the progress of the experiment as successive Ni/Cr interfaces were sputtered. The data presented in Figures 5.1-4 were determined from profiles obtained in this EN(E) mode. Multiplexing techniques were used

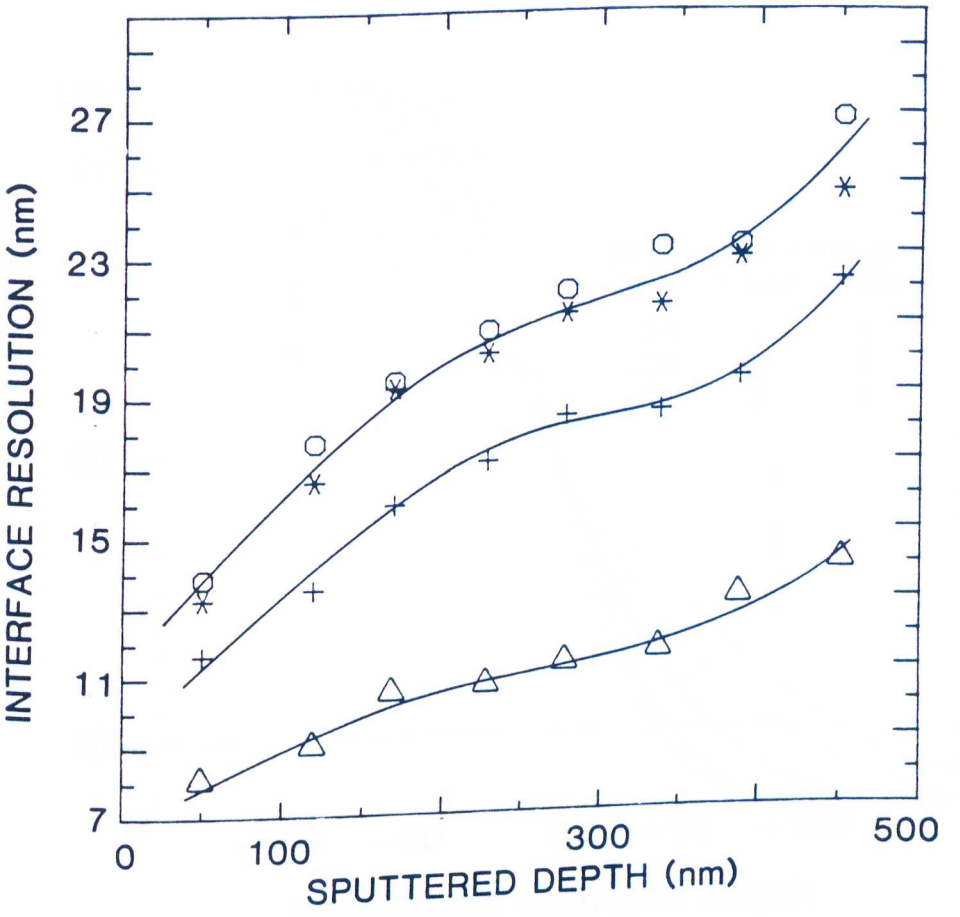

Figure 5.1 Interface resolution as a function of sputtered depth at eight successive Ni/Cr interfaces. Sputter profiling was done with argon ions: 1-keV(Δ), 2-keV(+), 3-keV(*), and 4.5 keV(o). The specimen was a prototype Ni/Cr material.

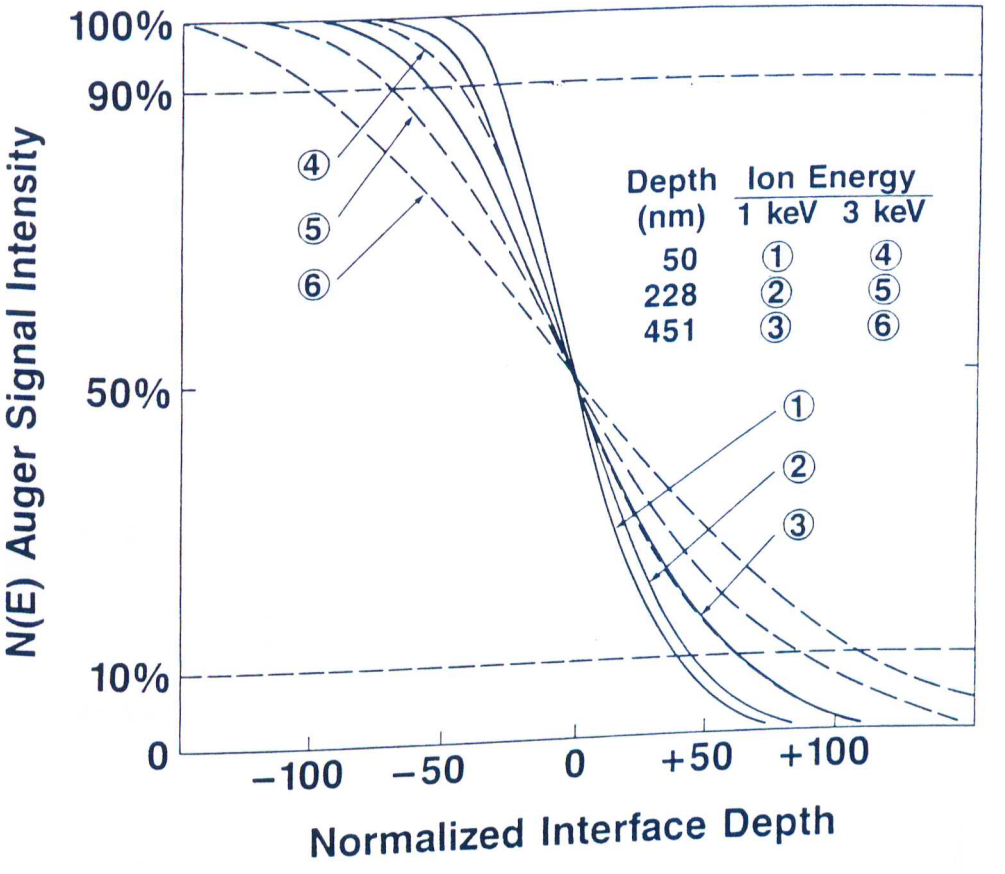

Figure 5.2 Interface profile shapes obtained at three sputtered depths using both 1 and 3 keV argon ions.

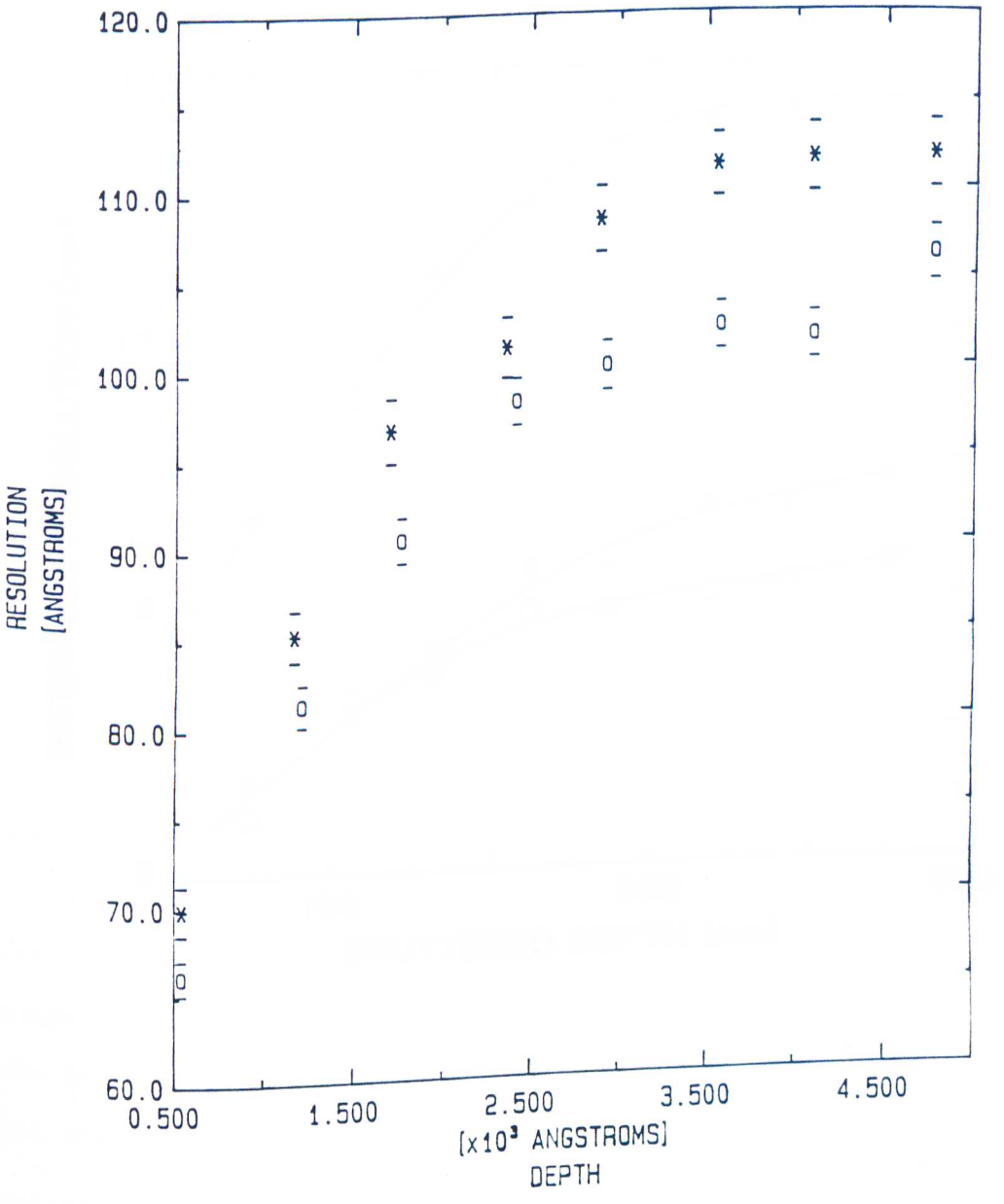

Figure 5.3 Interface resolution as a function of depth, with error bars, for 1-keV argon ions at two beam currents [170 nA(o) and 300 nA(*)]. The profiles are distinct to within experimental uncertainty (NBS SRM 2135), indicating a broadening effect due to higher current density.

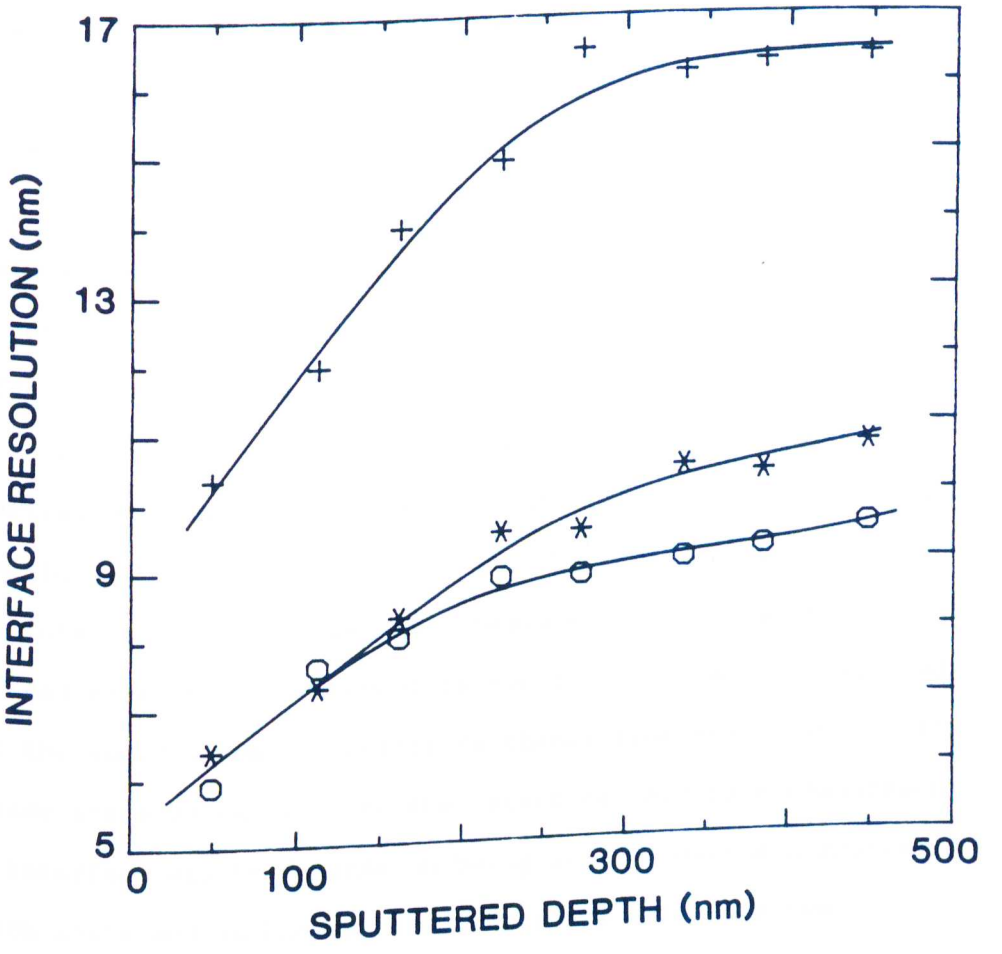

Figure 5.4 Interface resolution as a function of sputtered depth for 1-keV argon ions at two beam currents [170 nA(o) and 300 nA(*)] and for 2-keV argon ions [170 nA(+)] (NBS SRM 2135).

with the other instrument to obtain dN(E)/dE Auger intensities using a 5-keV primary electron beam (1 μA). Data obtained in this last mode are shown in Figures 5.5 and 5.6. Although both instruments used a single-pass cylindrical mirror analyzer (with concentric electron gun) as well as the same type of ion gun, the ion beam currents used with the EN(E) instrument were somewhat smaller than those used with the other instrument. It is possible that such differences in measurement technique can affect the observed widths of sputtered interfaces.

Interface broadening was determined from the Auger profiles by assuming that the original interface was a steplike function of composition with depth. The interface resolution (or interface width), used as a measure of the broadening, is defined here as the increment in sputtered depth (nm) required for the Auger signal intensity to change from 90% to 10% of its steady state value prior to the interface. Accurate measurement of interface widths depends on being able to define a sputtered depth scale and on knowing the sputtering rate of a two component interface. For the thin-layer standard samples used, the depth scale for these Ni/Cr materials is well known since the individual layer thicknesses have been measured and the relative Ni/Cr sputtering rates also have been determined [89].

Results of the relative Ni/Cr sputtering rates (in nm/s) indicate that this rate changes from 1.03 for 1-keV Ar^+ bombardment to 1.09 for 4.5 keV bombardment. Since the rates

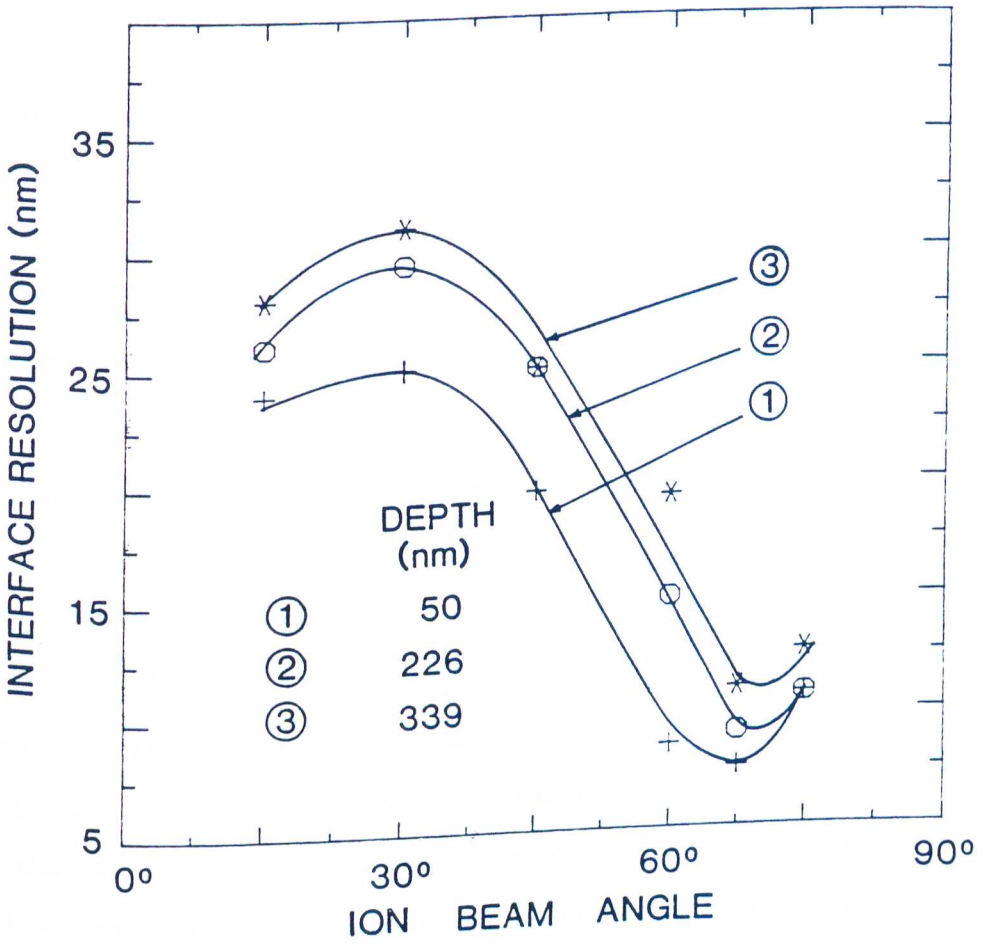

Figure 5.5 Dependence of interface resolution on ion beam angle of incidence (measured from the surface normal) at three sputtered depths for 2-keV argon bombardment (NBS SRM 2135).

are quite similar for Ni and Cr, an average sputtering rate was determined for each ion-energy depth profile and used to obtain the interface widths. The estimate of the uncertainty in these widths due to using this average rate is slightly less than 4%.

C. Results

i. Interface widths at an incident ion beam angle of 50°

Eight successive Ni/Cr interfaces, at depths ranging from 50 to 451 nm, have been sputter profiled with 1.0-4.5 keV argon ions incident on the specimen at a fixed angle of 50° with respect to the surface normal. An Auger sputter depth profile of the Ni/Cr multilayered thin film SRM 2135, taken with a 1-keV rastered argon beam, is shown in Figure 5.7. The profile was generated from over 1500 Auger EN(E) spectra and was produced using analysis software developed by the author. To determine the interface widths of this sample as a function of depth, further computer analysis was performed. Due to the large number of spectral intensities comprising the profile, it was tedious and impractical for the operator to readily locate and specify appropriate metal/metal interface regions. Therefore, it was necesary to program the microcomputer to

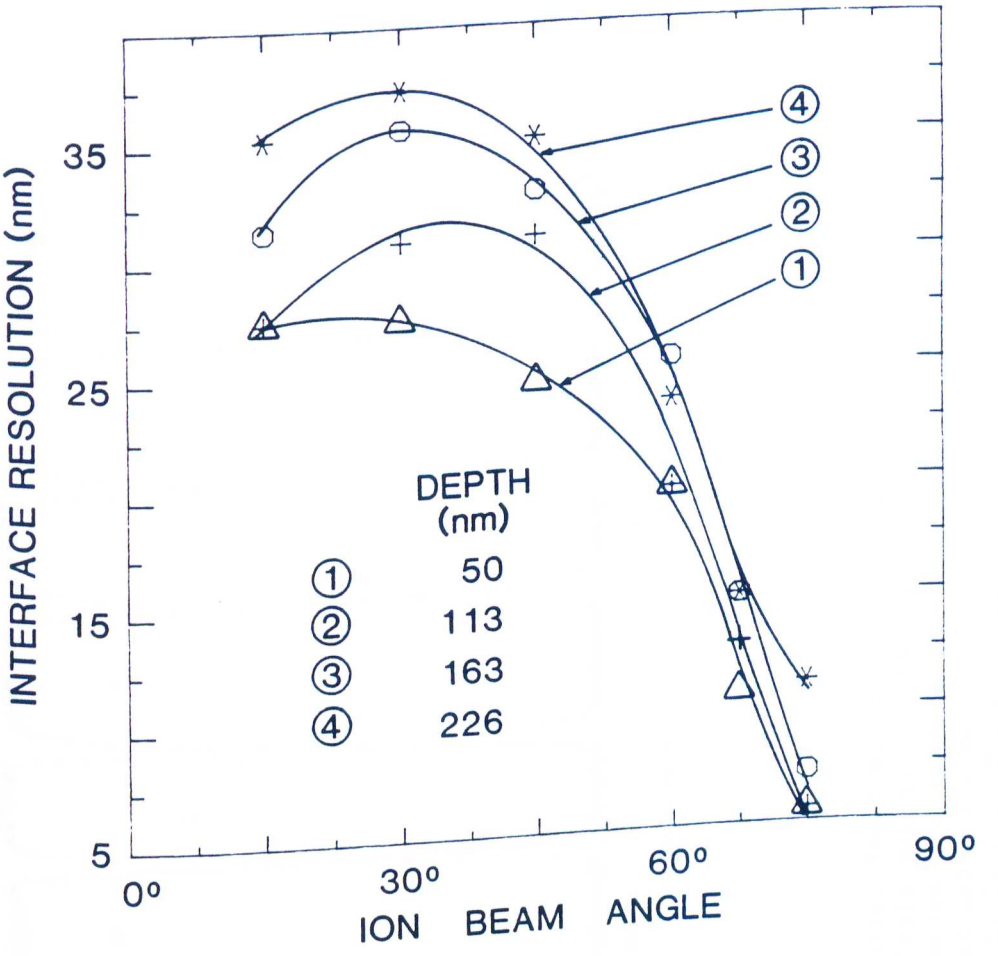

Figure 5.6 Dependence of interface resolution on ion beam angle (measured from the surface normal) at four sputtered depths for 4-keV argon bombardment (NBS SRM 2135).

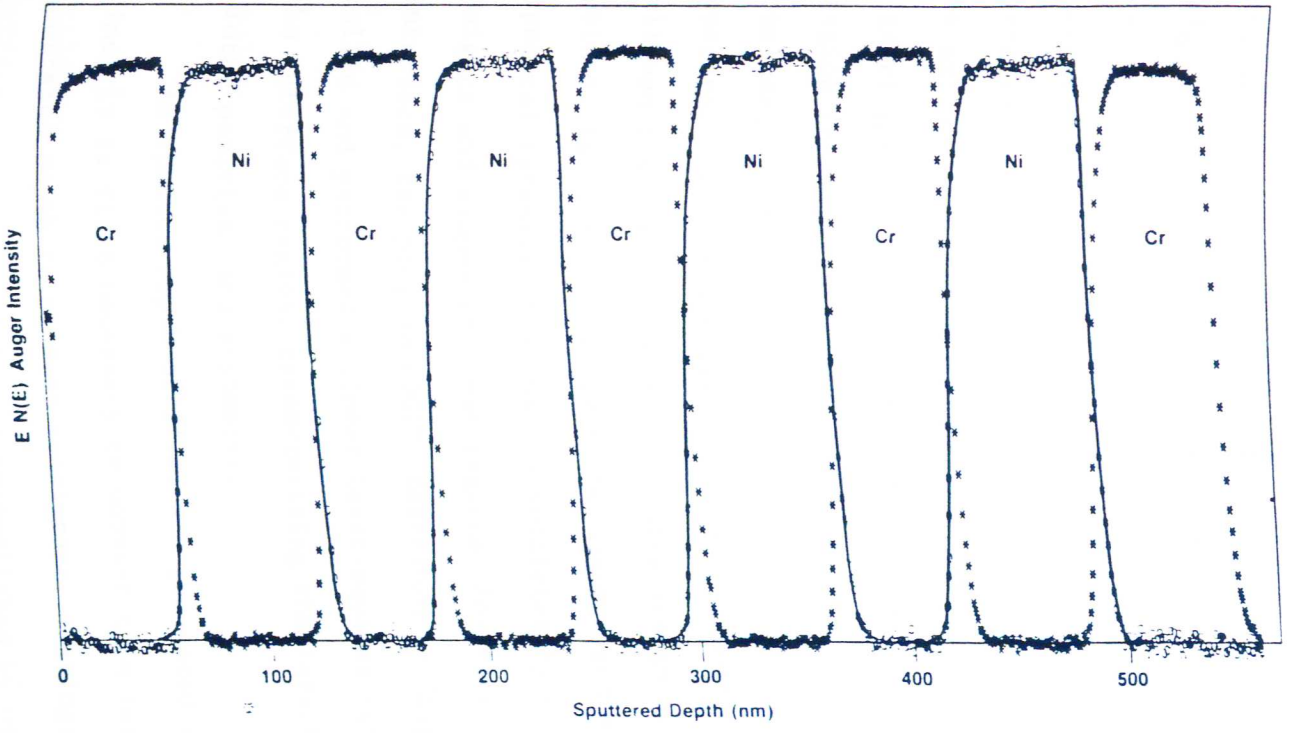

Figure 5.7 Auger sputter depth profile of Ni/Cr multilayered SRM 2135. Auger analysis was done in the EN(E) mode and the Ni and Cr intensities shown have been normalized. The metal films were sputter profiled using a 1-keV rastered argon beam (total sputtering time was 16 hours). The eight well-defined metal/metal interfaces obtained provide a sensitive means for calibrating sputtered depth.

automatically locate and identify appropriate Ni/Cr interfaces without operator intervention. This was accomplished by allowing the machine to search for continous slopes passing through 50% of the maximum peak intensity for the profile. The sign of the slope (positive or negative) was checked to determine correct correspondence with the direction of progression of the sputtered spectral intensities, ascending or descending, for each element separately. This method proved to be extremely reliable in practice and was capable of correctly ignoring stray or anomalous data points. Once the interface region for a given element had been identified, the program included a set number of data points, specified by the operator, to both the pre- and post- transition regions. This allowed for the inclusion of a large enough number of plateau points, ie. intensities from the maximum and minimum elemental spectral intensity regions, to sufficiently pin down the heights and slopes of these regions. For each successive interface, the program LOGIT, described in Chapter IV, was called and performed a linear least-squares fit of the data in the interface region, parameterizing the interface in terms of width, position, and asymmetry.

As sputter depth profiles are generated as functions of time, it is first necessary to convert them into functions of sputtered depth to produce consistent, meaningful, and comparable results. This was accomplished by utilizing the interface transition midpoint times provided by the LOGIT

subroutines. These times were then compared, interface by interface, to known thin-film layer thicknesses, determined by neutron activation analysis and by Rutherford backscattering[19], to produce a series of layer-by-layer sputtering rates through the sample. These sputtering rates were subsequently used to convert sputtering times in minutes to depths in angstroms. The width parameters returned by the LOGIT fit were similarly converted from units of time to units of distance along with their uncertanties. A plot of the widths of successive interfaces through SRM 2135, with error bars, is shown in Figure 5.8. Statistically significant interface broadening, due to topographical and other effects, is clearly exhibited. The solid line represents a fit to an exponential function of the form

$$Y(x) = A - Be^{-Cx} \qquad (5.1)$$

where x represents depth of the interface, Y the width, and A,B,C are fitting parameters. The ability to fit the interface broadening as a function of depth to such a simple function is an indication of the quality of the data.

Another measure of the consistency of our analysis technique is provided by two separate profiles taken on different days but on the same sample and under the same experimental conditions. These two distinct measurements, taken

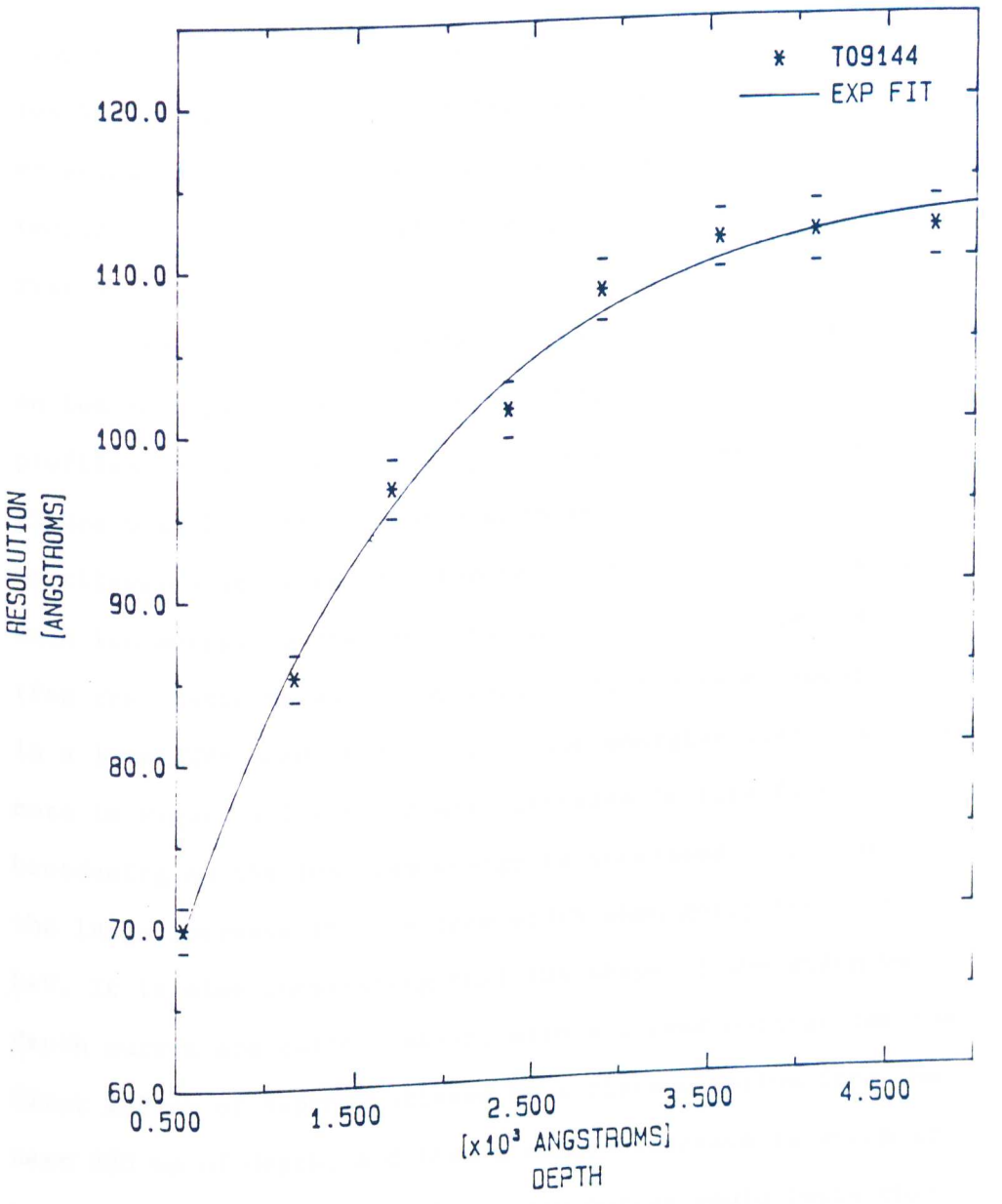

Figure 5.8 Plot of interface resolution vs depth, where known layer thicknesses have been used to convert time scales into depths. The solid line represents a least-squares fit to an exponential function. The ability to fit such a simple function to the depth dependence of interface broadening is an indication of the quality of the data.

for 1-keV argon ion profiling under the same beam conditions (100 nA), are shown in Figure 5.9. These sets of interface resolution data are very similar, agreeing to well within their experimental uncertainties, and demonstrate the precision, reproducibility, and consistency of this interface analysis system.

Interface width dependence on sputtered depth as well as on ion beam parameters , determined from EN(E) Auger sputter profiles obtained on a Ni/Cr prototype material, is shown in Figure 5.1. For this set of measurements, all made on the same multilayered specimen, the ion beam current was adjusted for each ion energy so that the instantaneous ion current density (for the static beam) was approximately the same (about 100 nA in a 1 mm FWHM beam) for the four ion energies used. One should note in Figure 5.1 the dramatic increase in interface broadening as the ion beam energy is increased, particularly the large increase in interface width when going from 1 to 2 keV. It is also interesting that the shape of the width vs depth curves are quite similar, with a linear portion for the first 200 nm of depth, followed by a plateau region from the next 200 nm of depth, and then a sudden increase in width at about 400 nm. These similarly shaped curves would imply that specific types of broadening processes take place over certain sputtered depths, more or less independent of the ion energy, and that changing the ion energy changes the magnitude of the specific type of broadening. This is consistent with a material

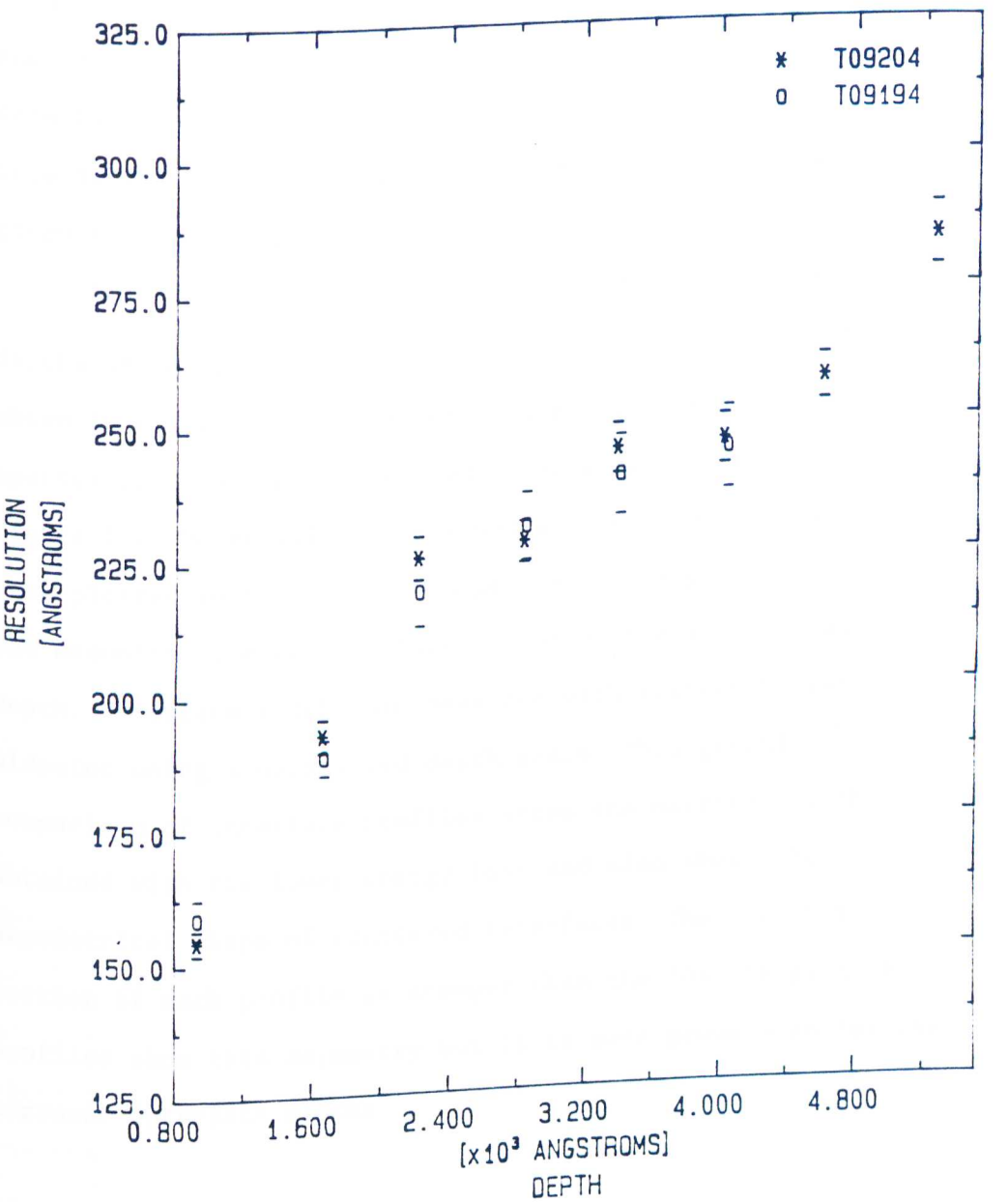

Figure 5.9 Interface resolution, with error bars, obtained at eight successive metal/metal interfaces of SRM 2135. Two separate profiles were run under the same sputtering conditions using 1-keV argon ions. These profiles show very similar sputtered interface widths and agree to within experimental uncertainty.

transport concept for interface broadening in which the higher energy ions have a greater range and produce more damage and defects, all of which may result in more interface interdiffusion and consequent surface topography change at a given sputtered depth.

Interface profile shapes obtained at three sputtered depths of 50, 228, and 451 nm using both 1 and 3-keV Ar^+ are shown in Figure 5.2. These curves are from the same set of sputter profiles that were used to generate Figure 5.1. In Figure 5.2 the profiles determined at the above depths have been plotted so that the 50% Auger intensity points (chosen as the midpoint of each interface) occur at the same normalized depth. Interface widths are measured with respect to each midpoint using a normalized depth scale. This graphical comparison of interface profiles shows the narrower widths obtained with the lower energy ions and also shows the asymmetrical shape of sputtered interfaces: The 90% -50% portion of each profile is steeper than the 50%-10% part. All profiles show this asymmetry but it is more pronounced for the narrower interface widths.

ii. Interface width dependence on ion current density

Measurements made of interface broadening using 1-keV Ar^+ bombardment indicate that the interface width observed is related to the instantaneous ion beam current density. Sputter depth profiles obtained at two different beam current densities (achieved by change in the argon pressure in the gun) but otherwise under identical gun conditions show broader interfaces at the higher current density. This interface width dependence on sputtered depth is shown in Figure 5.3 for 1-keV Ar^+ at beam currents of both 170 and 300 nA as well as for 2-keV Ar^+, shown for comparison, in Figure 5.4; the Ni/Cr specimen used for this measurement was an NBS SRM 2135 and was different from that used for the previous profiles. The difference in width determined for 1-keV Ar^+ at these two beam currents and at depths greater than 250 nm is greater than the measurement uncertainty. Considering the reproducibility of the profiles shown in Figure 5.9, which were taken at similar depths but under constant ion beam current density conditions, it is reasonable to conclude that the difference in widths observed in Figure 5.3 are a result of the different ion beam current densities used. This assertion is supported by the statistical analysis associated with these results.

Although electron beam current density effects on interface broadening have been observed in Auger sputter profiling,[91-93] broadening attributable to ion beam current

density has not, we believe, been previously reported. Whereas the electron beam broadening seems to be related to localized heating and consequent diffusion, the ion beam current densities are, however, much too low to cause similar thermal effects. It is possible, however, for diffusion to occur along defects produced as a result of ion bombardment: radiation enhanced diffusion [94-99]. Defect diffusion can take place at room temperature [97-99] but does depend on how fast the defects anneal out and on the displacement energy necessary for atoms and defects to migrate. Should the defects anneal out before overlapping collision cascade can occur, then the collision events arising from seperate impinging ions are independent and there will be no current-density related effects. However, if the defect lifetime is greater than the time for an overlapping cascade to take place, then the energy in the overlapping cascade can also give rise to enhanced atomic displacement along defects produced by the previous cascade. Such an ion-current-density dependent diffusion can result in material redistribution, in crystallographic reordering, and, consequently, in surface topography change. Since changes in surface topography often are cumulative, increased interface broadening is expected to occur at greater sputtered depths as shown in Figure 5.4

The relationship of ion current density to the development of surface topography may not be well understood

but it certainly is not unknown[100]. Surface topography formation which results from ion bombardment is not simply a function of the total ion dose but can depend rather critically both on the ion current density employed as well as on the specified materials being sputtered [e.g., for Cu(11 3 1) a current density greater than 100 $\mu A/cm^2$ of 40-keV Ar^+ ions is needed] [100]. The existence of an ion current density effect on topography development would seem to indicate that the current density dependent interface broadening which was observed here may also be related to changes in topography. This interdependence of sputtered interface widths, surface topography developmment, and ion current density needs further clarification if sputter depth profiles are to be correctly interpreted.

iii. Interface width dependence on incident ion beam angle

Ni/Cr multilayered SRMs were sputter profiled at different angles of ion beam incidence in order to determine how this would affect interface resolution [63]. Each complete dN(E)/dE Auger profile (8 Ni/Cr interfaces) was obtained at one fixed beam angle. A set of six such angle dependent profiles was acquired at constant ion beam current (although not at a constant ion current density) and at constant ion energy;

measurements of interface widths were obtained for argon ion energies of both 2-and 4-keV. These results of interface width dependence on ion beam angle of incidence are summarized in Figures 5.5 and 5.6 for 2-keV and 4-keV Ar^+ profiling, respectively. Interface widths (shown in Figure 5.5) are plotted at only three sputtered depths (50, 226, and 339 nm) in order to present more clearly the dependence on beam angle. Similar interface width data is given in Figure 5.6 at four sputtered depths (50, 113, 163, and 226 nm). One should note that these results were obtained on an NBS SRM 2135 specimen.

The two sets of interface width data, given in Figures 5.5 and 5.6, display a very similar dependence on ion beam angle: the interface widths show a broad maximum at about 30^o ion beam angle and then become much narrower as the beam angle increases (becomes more grazing). Also, there is a general increase in width with sputtered depth, similar to what we have already reported at fixed beam angle, and the 2-keV widths are much narrower than the 4-keV widths, except near 75^o beam angle. These results indicate that narrower interfaces can be obtained at lower beam energy and at near-grazing ion beam angle. The data presented in the last two figures together with that of Hunt and Seah[82] are the only such results showing interface width dependence on ion beam angle of which we are aware.

There seem to be two dominant factors which control this dramatic decrease in sputtered interface widths as the incident ion beam becomes more grazing. These are the effects of ion current density and the extent of the collision cascade normal to the surface. Included in the results of the width dependence on ion beam angle (shown in Figures 5.5 and 5.6) is also an ion current density which for this data is proportional to cos θ (θ is the angle of the ion beam measured from the surface normal). For the range of beam angles used here, this amounts to a factor of about 4 in ion current density. Since we have seen that a reduced ion current density can result in narrower width, it seems reasonable that one consequence of using a more grazing ion beam is the reduction in ion current density. The other consequence is that the depth of the collision cascade, also proportional to cos θ, is reduced. Assuming that material redistribution and topography change are predominantly responsible for the interface broadening observed at the sputtered depths examined here, then decreasing the depth of the collision cascade region should reduce the range of defect diffusion, reduce recrystallization, and therefore reduce topography development. Sputter profile measurements which we have made on these same materials at fixed ion beam angle using Xe^+ instead of Ar^+ also show a significant decrease in interface widths. Since the extent of the collision cascade resulting from the impact of a heavier ion is smaller than from

a lighter ion, it is reasonable to conclude that the depth of the cascade does affect the width of these sputtered Ni/Cr interfaces. In the results presented here on interface width vs ion beam angle, both the current density and the cascade depths do change with beam angle and both can be effective in determining the observed widths. One cannot distinguish the separate role played by these two factors on the measurement of sputtered interface widths.

D. Summary and Conclusion

Interface resolution measurements have been made by Auger Sputter depth profiling of Ni/Cr multilayered thin-film structures in order to determine the effect which ion bombardment parameters have on interface broadening. Various bombardment parameters such as ion beam energy, angle of incidence, and ion current density, as well as sputtered depth have all been examined on these materials which have been shown to have well defined interfaces. This consistent set of metal/metal interface width measurements makes it quite apparent that in order to assess the intial sharpness of an interface, one must consider the conditions under which it was sputtered: interface broadening is not simply a materials dependent phenomenon. Understanding how these conditions affect interface depth resolution can be useful in the optimal

selection of sputter depth profiling parameters.

VI. RADIATION ENHANCED DIFFUSION

A. Introduction

The study of phenomena which occur during the sputtering of solids by ions has attracted continuous interest ever since sputtering has been used either as a layer deposition method or as a technique for layer-by-layer analysis. A wide variety of phenomena result from sputtering; among these are roughening, amorphyzation, preferential sputtering, segregation and enhanced adsorption, implantation, recoil implantation and knock-in, cascade mixing, and radiation enhanced diffusion (RED)[101-103,70-72]. All these influence the depth resolution of sputter-based analysis techniques. Therefore, depth resolution has been used to study such phenomena. However, additional information is required in order to separate the factors contributing to interface broadening. The usual assumption is that these contributions sum in quadrature [70], which is equivalent to assuming that an originally step-like interface will be transformed by the measurement to an error-function-like depth profile, an assumption of limited validity[60,104]. On the other hand, such an assumption makes it possible to choose systems and parameters which simplify the analysis but often

require the collection of a large amount of information employing various materials and analyzing methods.

Radiation enhanced diffusion (RED) and radiation-induced mixing (RIM) are two interrelated, yet different phenomena. While the latter is confined to the cascade of collisions initiated by the impinging primary ion, RED is a phenomenon which is spatially and/or temporally outside the region of the cascade. Investigations of sputtering related defects and of transmission sputtering show that a substantial number of displaced atoms reach far beyond the predicted range of the random collision cascade, not only in the case of monocrystalline and polycrystalline targets, but even in amorphous materials[105,106]. It should be emphasized that this range effect applies to a variety of primary ions, including noble gases, down to energies as low as 700 eV. This observation means that RED may take place in many systems during sputter depth profiling, producing effects at depths beyond the range of cascade mixing, provided the activation energy of diffusion of the species involved is sufficiently low.

Considerable effort has been made by several authors to provide an analytical description of interface profiles attributable to RIM[107-109], but, such theoretical predictions of interface broadening underestimate that which is actually observed[108]. This may be due in part to the role played by RED.

Early theoretical work relating to the subject of RED was performed by Dienes and Damask[110], who developed a microscopic theory of diffusion based on the creation of point defects (atomic vacancies or interstials in a solid lattice structure) through the process of ion bombardment. In this model, energetic impinging ions create defects by providing sufficient energy to displace atoms from their lattice sites; these defects subsequently diffuse over concentration gradients leading to the observed phenomenon of RED. Dienes and Damask provided a rigorous mathematical and physical description of this process in terms of diffusion kinetics.

More recent theoretical work has been geared towards the investigation of the so-called "altered layer," a thin layer at the surface of an ion bombarded multicomponent solid that suffers compositional changes as a result of the bombardment process. Winters and Coburn[111] developed a phenomenological model of alloy sputtering, considering the effects of sputtering, such as impact or damage enhanced diffusion, to extend below the topmost surface layer to a depth of about 10 nm. Because the sputtering process causes large numbers of vacancies and interstitials to migrate to the surface, Winters and Coburn considered this surface region to be in a high state of flux. Ho[97], in an elegant paper, rigorously reformulated this model by introducing an additional mass balance equation for the region below the surface layer to be solved

simultaneously with that for the sputtered surface. Ho was able to demonstrate that useful information such as the ejection probability ratio, altered layer thickness, matrix effects, and initial surface composition could be judiciously extracted from the Auger depth profiling data in terms of his model.

In a later paper, Chou and Shafer[112] argued that though the model of Ho was largely theoretically sound some inconsistencies arose from certain implicit assumptions made without consideration of their physical origin. Chou and Shafer attempted to remove these inconsistencies through a generalized reformulation involving the reduction of kinetic and transport theory in phase space to a mass transport problem in physical space. From this generalized theory, these authors derived various particular cases governing binary alloys and compounds. Chou and Shafer were able to extend their model to include the frequently ignored effect of ion impregnation.

In order to investigate the ion-bombardment induced alteration of the near surface region, Swartzfager et al.[3] performed experimental studies on Cu-Ni and Au-Pd alloy surfaces annealed at 600^{o}C under steady-state ion bombardment conditions. Measurements were performed at varying initial temperatures and ion dose. Typically, samples were heated, sputtered, and then quenched to liquid nitrogen temperature to freeze in the defects. Depth profiling was performed on the samples after quenching. Basing their analysis on the

theoretical model of Ho, Swartzfager et al. were able to determine the altered layer thickness as a function of initial sputtering temperature. The altered layer thickness was found to be independent of the ion current density, but the enhanced diffusion coefficient was found to be directly proportional to the current density.

Similar types of experiments were performed by Li and Koshikawa[4], who measured the radiation enhanced diffusion and segregation in an Au-Cu alloy quenched to liquid nitrogen temperatures. Diffusion coeficients were measured as a function of the pre-quench sputtering temperature and were found to be significantly higher than those for normal diffusion by a factor of 10^6 . Arrhenius plots of Ln D versus 1/T were made to determine the activation energy for the enhanced diffusion process. In an attempt to correlate the cohesive energy and the onset of radiation enhanced diffusion in ion mixing, Cheng et al.[113] performed a beam irradiation study of W-Mo, Ta-Nb, and Pt-Pd bilayered systems. These authors found a correlation between the cohesive energy of ion mixed solids and a critical temperature T_c at which radiation enhanced diffusion was found to become dominant.

A Monte-Carlo code simulation of the generation of point defects (the mechanism for RED) was carried out by Karpuzov and Armour[114]. Depth and lateral spread distributions of defects generated by 0.5 - 5 keV argon ion bombardment of crystalline

Ni were determined using the computer simulation program MARLOWE. These authors found the vacancies to be well separated from the interstitials over the entire energy range investigated. The authors also observed the formation of depleted zones resulting from replacement sequences and defect recombination.

Experimental studies of RED[115-119,3,4] usually consist of 3 steps: (1) a sample is prepared containing a marker of well-known depth distribution; (2) the sample is then irradiated (ion bombarded) and (3) the depth profile of the marker is obtained (this last step often includes the observation of the radiation induced segregation, RIS). Studies of RED caused by ion sputtering are complicated by the erosion of the sample during irradiation[108]. The depth profiles obtained in step 3 are frequently observed using techniques which remove surface material by sputtering, which, also can lead to additional complexity in evaluation.

In a preceding study[99], it was shown that Ag segregates to the surface from a thin Ag layer buried beneath a thick (50 nm) Ni layer after the outer Ni layer has been partly removed by sputtering, at room temperature. While that study was directed to the analysis of RIS, it showed also the role of diffusion in the transport of Ag atoms to the surface. The segregation rate was shown to obey first order kinetic

equations, and segregation rates for 1 keV and 4 keV sputtering were determined.

The aim of the present study is the analysis of RED occuring during ion bombardment (thus combining steps 2 and 3) using Auger depth profiling and the description of the depth profile obtained using a simple model, which includes primarily roughening and RED, the latter being characterized by an effective diffusion rate. This approach has the advantage that the results obtained are directly applicable to Auger (and SIMS) depth profiling and allow us to separate the contributions due to each effect. In these experiments, no quenching is performed prior to the depth profiling process, i.e. the sample temperature is held fixed during the entire course of the experiment.

The evaluation of Ni/Ag Auger depth profiles including the separation of the interface broadening due to RED and roughening of the surface is rather complex. This separation can be confirmed, however, by an independent measurement of the surface roughness using light scattering from the surface, since the magnitude of light scattering varies in direct proportion to the amount of surface roughness. Surface roughness measurements were performed in-situ on the same samples and on the same surfaces studied by AES depth profiling.

Experimental investigation of the broadening of interfaces due to radiation enhanced diffusion was performed

under the direction of Dr. Joseph Fine and Dr. Denes Marton of the National Bureau of Standards. The computerized experimental monitoring, the automated spectral data analysis, and the asymmetric Gaussian fitting and analysis programs were developed by the author. The experimental study of the temperature dependence of defect diffusion and interface broadening was performed by the author. Light scattering studies of surface topography were performed by Dr. Marton and are included here for comparison.

B. Experiments

Both RED and surface roughening which result from ion bombardment of the Ag/Ni and Cr/Cr_2O_3 systems were analyzed using multilayered Ag/Ni and Cr/Cr_2O_3 thin film structures. The Ag/Ni structures consist of five thin (3-4 nm) Ag layers alternately deposited between six thick (50 nm) Ni layers. The Cr/Cr_2O_3 structures consist of metallic Cr interleaved with seven extremely thin (~3 atom layers thick) Cr_2O_3 marker layers placed at 40 nm intervals. Such samples were produced by sputter deposition using polished Si substrates that had been coated, in situ, with amorphous Si prior to the deposition of the metal films and are similar to those previously described[99]. The total thickness of these layered structures was determined by the quartz oscillator microbalance technique during

deposition and checked by stylus measurements after the analysis. The thicknesses of the Ag layers were estimated from microbalance results; estimates based on Auger sputter-depth profile results, however, are probably more accurate.

Sputter-depth profiling of the Ag/Ni samples was carried out using Ar^+ ions of both 1-keV and 4-keV energy. Depth profiling of Cr_2O_3 marker layers was performed using 1-keV Ar^+ ions only. A differentially pumped ion gun produced a beam whose diameter was about 1 mm at total beam currents in the 50 to 500 nA range; Auger analysis was performed using a high resolution single-pass cylindrical mirror analyzer described elswhere [22]. The base pressure in the vacuum system during the experiments described here was typically 3×10^{-9} Torr. Auger electron-spectra excited by a primary electron beam of 2500 eV energy (50-200 nA) and rastered over a surface area of about 10 x 10 μm were recorded in a pulse counting mode; digital background subtraction techniques were employed to obtain high precision depth profiles. The elements detected were Ni (LMM line, 844 eV), Ag (MNN line, 349 eV) and nitrogen (KLL line, 375 eV) for the Ni/Ag system and Cr (LMM line, 525 eV) and O (KLL line, 503 eV) for the Cr/Cr_2O_3 system. The fact that the Auger spectral lines for Cr and O lie so closely together presents a problem in the data analysis that is discussed below. Monitoring of N is important because it is a possible

contaminant both from the residual gas and the Ar reservoir; furthermore, nitrogen, if it were present, would appear in the background of the Ag line and would consequently have a significant effect on the Auger analysis. Nitrogen has not been detected in any of our depth profile measurements except in the outermost few atomic layers of the samples.

A typical depth profile is shown in Figure 6.1. The abscissa is the sputtering time, which can be readily transformed to a depth scale using layer thicknesses obtained from Rutherford backscattering and neutron activation analysis. It is interesting to note that the sputtering time intervals between the Ag peaks are equal to the sputtering time needed to reach the first peak. Thus no peak shift is observed, to within the uncertainty of the depth scale, estimated to be about 10%.

For light scattering measurements, some depth profiling experiments were interrupted after the 1st, (2nd, etc.) Ag layer had been crossed. These optical measurements have been carried out in-situ, using an ellipsoidal mirror and a semiconductor detector, both situated in the UHV analysis chamber. A He-Ne laser (633 nm wavelength) was used as the light source. The sensitivity of these experiments was limited to approximately 3 nm (r.m.s. roughness) because of a background due to scattered light internally reflected from the walls and components of the apparatus. Relative values of the RMS surface roughness were derived from these experiments,

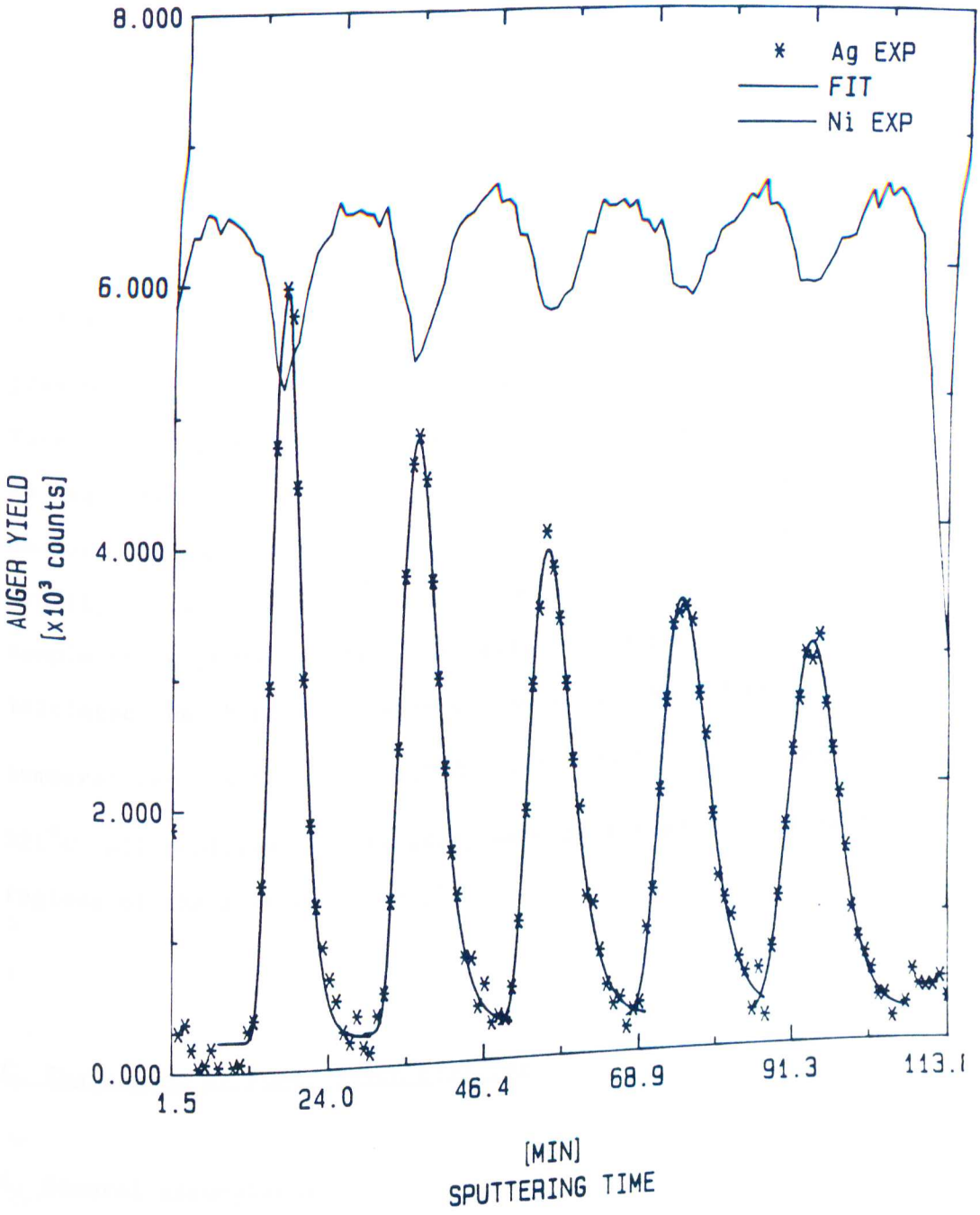

Figure 6.1 Auger depth profile of a Ni/Ag multilayered thin-film structure (E_p = 1 keV). The ordinate in the N(E) yield in counts per channel of the Ag MNN line. Measured Ag data are shown as (*); Ni data are connected with straight lines. The full line through the Ag data represents a fit to eq. 6.8.

using the theory of light scattering in the smooth surface limit [120].

The investigation of the dependence of depth profiles on temperature was performed on a Ag/Ni system using 4-keV Ar^+ ions at a current density of 100 nA/cm^2. The background pressure in the chamber was typically on the order of 2×10^{-9} Torr. The sample was heated by applying a voltage between 5 and 18 volts to an attached heater coil and the temperature was measured using a Chromel-Alumel thermocouple. Heating was usually performed overnight at a given voltage, allowing the sample temperature to stabilize before depth profiling was initiated. Depth profiles were collected at the following temperatures: 26°C, 102°C, 137°C, 171°C, 221°C, 330°C, and 521°C. All profiles in this study were performed on different regions of the same Ag/Ni sample.

C. Evaluation of Auger depth profiles

i. General assumptions

Depth profiles of Ag and Ni were generated using the spectral background subtraction and analysis software described in Chapter IV. As mentioned above, the analysis of O and Cr

spectra poses a special problem because of the overlap of their Auger spectral peaks at 503 eV and 525 eV respectively. In order to deconvolute the two spectra, a background subtraction was first performed in the Cr peak region by extrapolating from data at higher energies as shown in Figure 6.2. This background was subtracted from data near the Cr peak in the center of the figure. The resulting peak was fit to a Guassian and the peak height intensity was determined in the usual manner. The peak height derived from this fit was in turn used to establish the high energy asymptotic region of an asymmetric logistic function of the type described in Chapter IV. The lower energy side of the Cr spectral peak was then fit to the logistic function (upper solid line) using points on both sides of the small oxygen peak seen in the far left side of the figure. As can be seen, the asymmetric logistic fit characterizes this region well, allowing a reproducible subtraction of the Cr spectrum from under the overlapping oxygen peak. After background subtraction, the deconvoluted small oxygen peak can be readily fit to a Gaussian function and its peak height intensity determined. The software was designed to automatically perform the analysis on successive Cr and O Auger spectra without operator intervention. A computer generated depth profile for a Cr/Cr_2O_3 multilayered structure performed at 1-keV Ar^+ ion bombardment is shown in Figure 6.3.

The evaluation procedure for each depth profile, of the types shown in Figs. 6.1 and 6.3, is based on the series of

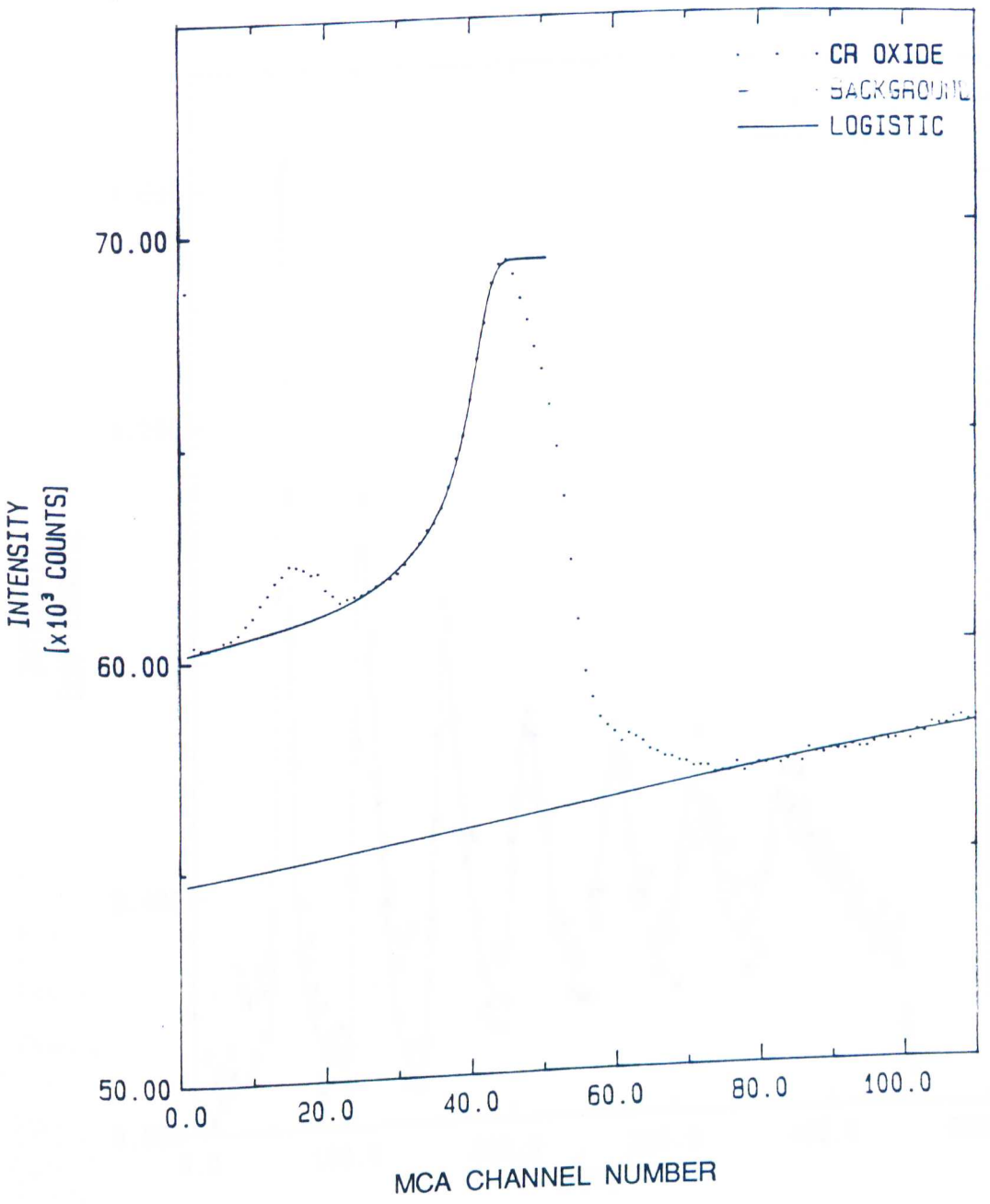

Figure 6.2 Overlapping Auger spectra of Cr (large peak) and of O. Thin solid line represents an exponential background fit for the Cr spectrum. A logistic function fit (upper solid line) is shown to characterize the left side of the Cr peak. This line is then subtracted from the small O peak to deconvolute the spectra.

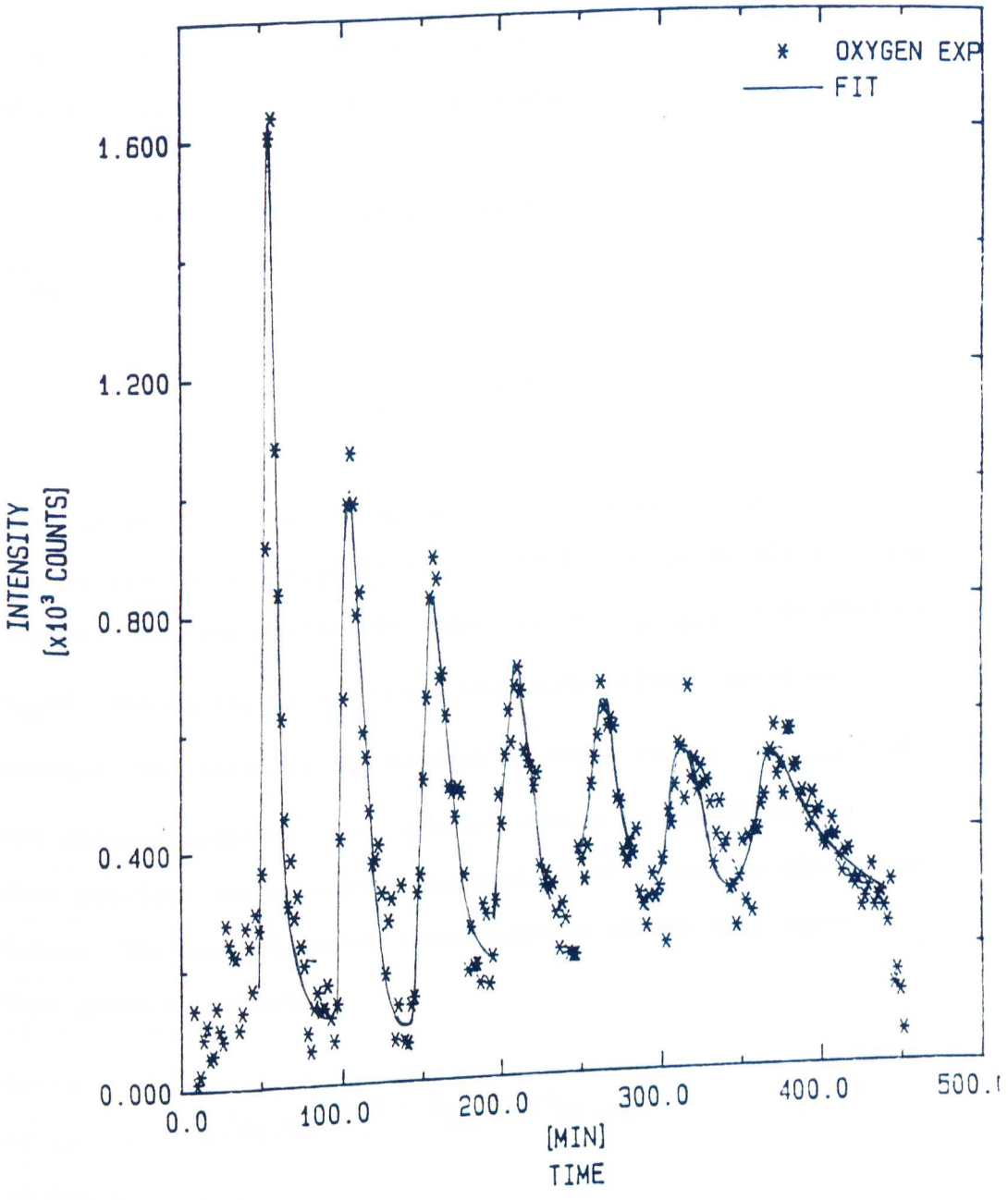

Figure 6.3 Auger depth profile of a Cr/Cr_2O_3 mutlilayered thin-film structure (E_p = 1 keV). The solid line represents a fit to each layer of eq. 6.8. Each layer was fit separately using this equation.

assumptions and simplifications listed below. Some of these are quite widely accepted and will not be dealt with in detail while others will be given more extensive description.

1. The sum of the fractional concentrations of silver (c_{Ag}) and nickel (c_{Ni}) is

$$c_{Ag} + c_{Ni} = 1 \tag{6.1}$$

i.e. there is no third component in this sample. The nickel layers are thick enough to reach 100% Ni in the middle of these layers, thus the maximal Ni Auger yields, $I_{Ni,max}$ correspond to $c_{Ni}=1$. The Ag layers are thin, thus 100% silver cannot be reached. The ratio of the minimal Ni Auger yields ($I_{Ni,min}$) in the silver layers to their maximal values in the Ni layers then provides the concentration minimum of nickel in the silver layers. The maximal silver concentration at the same layer is then given by relation

$$c_{Ag,max} = 1 - I_{Ni,min}/I_{Ni,max} \tag{6.2}$$

2. The sputtering rate of a Ag-Ni compound is a linear combination of the sputtering rates of Ag and Ni:

$$S = S_{Ag}c_{Ag} + S_{Ni}c_{Ni} \qquad (6.3)$$

where S_{Metal} is the sputtering rate (nm/s). In calculation of S, two further simplifications have been adopted: the average silver concentration, $\langle c_{Ag} \rangle \simeq 1/2 c_{Ag,max}$ and $S_{Ag} \simeq 3S_{Ni}$ (based on bulk densities and absolute sputtering yields[121]. The sputtering rate of Ni was estimated from the sputtering time between two silver concentration maxima and the thicknesses of the layers.

3. The thickness of the Ag layers (d_{Ag}) can be determined from the area under the Ag peak, arrived at through numerical integration using Reimann sums; a value of $d_{Ag} = 3.7 \pm 0.6$ nm was obtained in this way.

4. Each individual depth profile of a given single Ag layer is analyzed independently. Each such depth profile resembles a Gaussian in shape but is asymmetric, having a steeper slope at earlier sputtering times. We propose that each of these Ag profiles is the result of the superposition of a Gaussian (symmetric) and a RED (asymmetric) profile. The width of the Gaussian is determined mainly by surface roughness, although a small contribution from other factors is not excluded. One such contribution is the thickness of the Ag layer, another is the escape depth of Auger electrons, a third is interface broadening due to cascade mixing, and a fourth is

that due to thermal diffusion. Since Monte Carlo computer simulations of ion bombardment on multicomponent systems[81] tend to show that the contributions from these factors are small and since there are no grounds to suggest that the surface roughness distribution is anything other than normal, our assumption is that all these combined factors yield a Gaussian depth profile shape:

$$c = (2^{1/2} c_o/\Delta z_R)\exp[-2(z-z_o)^2/\Delta z_R^2] \qquad (6.4)$$

where c_o depends on the total number of the Ag atoms per surface area in that single silver layer, z is the depth coordinate, directed perpendicular to the surface, and z_o is the depth of the center of the Ag layer. According to the assumptions made so far,

$$\Delta z_R^2 = \Delta z_r^2 + d_{Ag}^2 + l_e^2 + \Delta z_c^2 + \Delta z_d^2 \qquad (6.5)$$

where Δz_r, Δz_c and Δz_d are the contributions of surface roughness, cascade mixing, and thermal diffusion, respectively, and l_e is the inelastic mean free path of Auger electrons.

ii. The RED model

The RED process takes place during the time of sputter-depth profiling, but physically outside the actual collision cascade.

Furthermore, we assume that RED starts when the sputtered surface is at a distance of z_o from the Ag layer (c.f. Figure 6.4), and it continues at a constant rate after that. This will lead, according to standard diffusion theory for a planar source of negligible thickness at z_o, to a profile described by the equation[122]:

$$c = c_o(4Dt)^{-1/2}\exp[-(z-z_o)^2/4Dt] \qquad (6.6)$$

where D is the diffusion coefficient and t is the diffusion time. Time t is related to depth z, according to the above definition for z_o by

$$z = St \qquad (6.7)$$

where S is the sputtering rate of the ion beam through the sample. Note that the time t is not the "laboratory time" t_L indicated in the abscissa of depth profiles (c.f. Fig 6.1), but is calculated for each Ag layer separately.

Figure 6.4 may help to illustrate the model postulated here. The defect concentration, d, introduced into the target

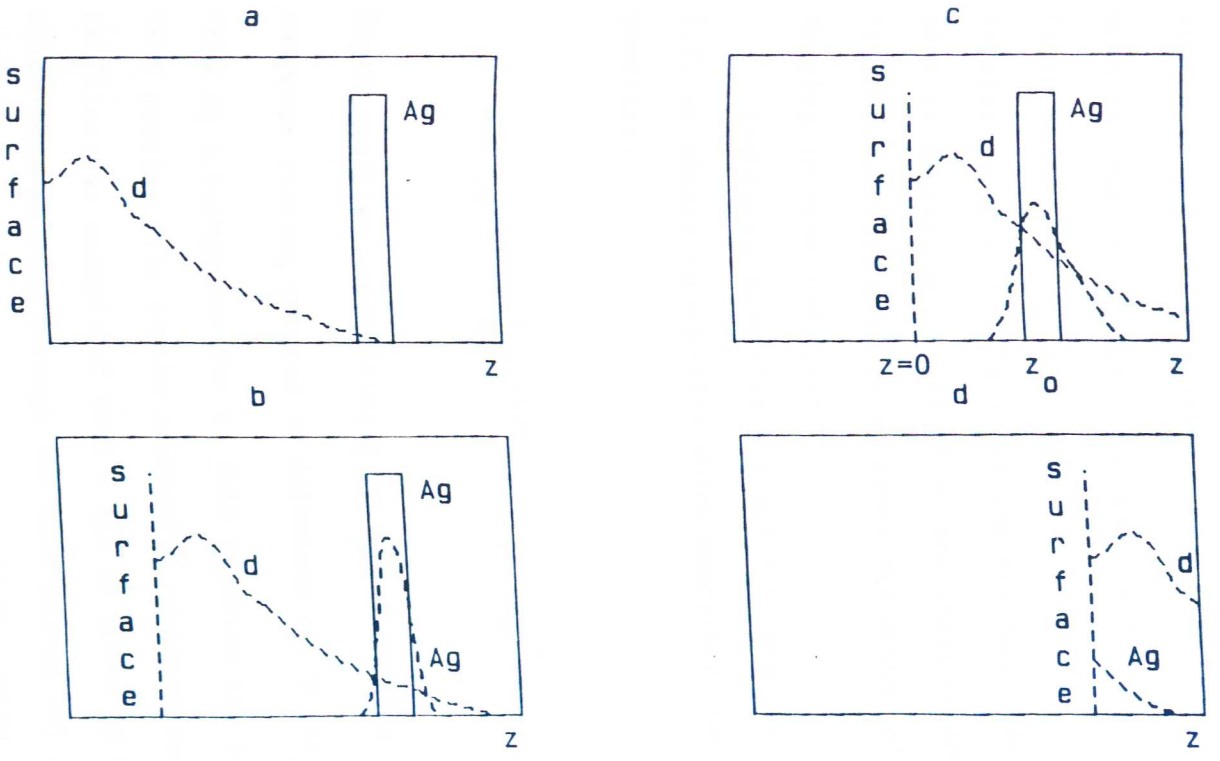

Figure 6.4 The diffusion model used to evaluate the RED part of the layer broadening. The abscissa is the depth coordinate, the ordinate represents concentrations of defects (d) and of silver (Ag), in arbitrary units. (a) The onset of sputtering of the Ni layer. (b) The surface is still far from the Ag layer. (c) Diffusion starts at this moment according to our model. (d) the diffusion continues until all Ag atoms are removed.

by ion bombardment is a function of depth. It is taken to be equal to zero when the bombardment has just started (a) and remains 0 as long as the distance between the Ag layer and the sputtered surface is greater than z_o (b). Starting at $z<z_o$, both the defect concentration and the diffusion rate D are taken to be constant in depth (c). The diffusion is only terminated after the Ag atoms are sputtered away (d). This picture is very much simplified and leads to some averaged "effective" diffusion rate, since the actual diffusion rate is varying in time and space.

Combining equations 6.4 and 6.6, and taking into account 6.7, we obtain an equation which describes the measured depth profiles:

$$c = c_o(4Dt+\Delta z_R^2/2)^{-1/2}\exp[\ -(St-z_o)^2(4Dt+\Delta z_R^2/2)^{-1}] \quad (6.8)$$

Depth profiles, containing c vs t_L information, are used in a computer fitting program to calculate c_o, D, Δz_R, and z_o, as well as a background for c. This equation can be used to obtain very precise fits to the asymmetric Ag-layer sputter depth profiles; an example of such a fit is shown in Figure 6.5. The solid line passing through the data points (*) represents a linear least squares fit to eq. 6.8. The solid jagged line on the zero axis under the peak represents the Y(obs)-Y(calc) values provided by the fit. As can be seen, these values

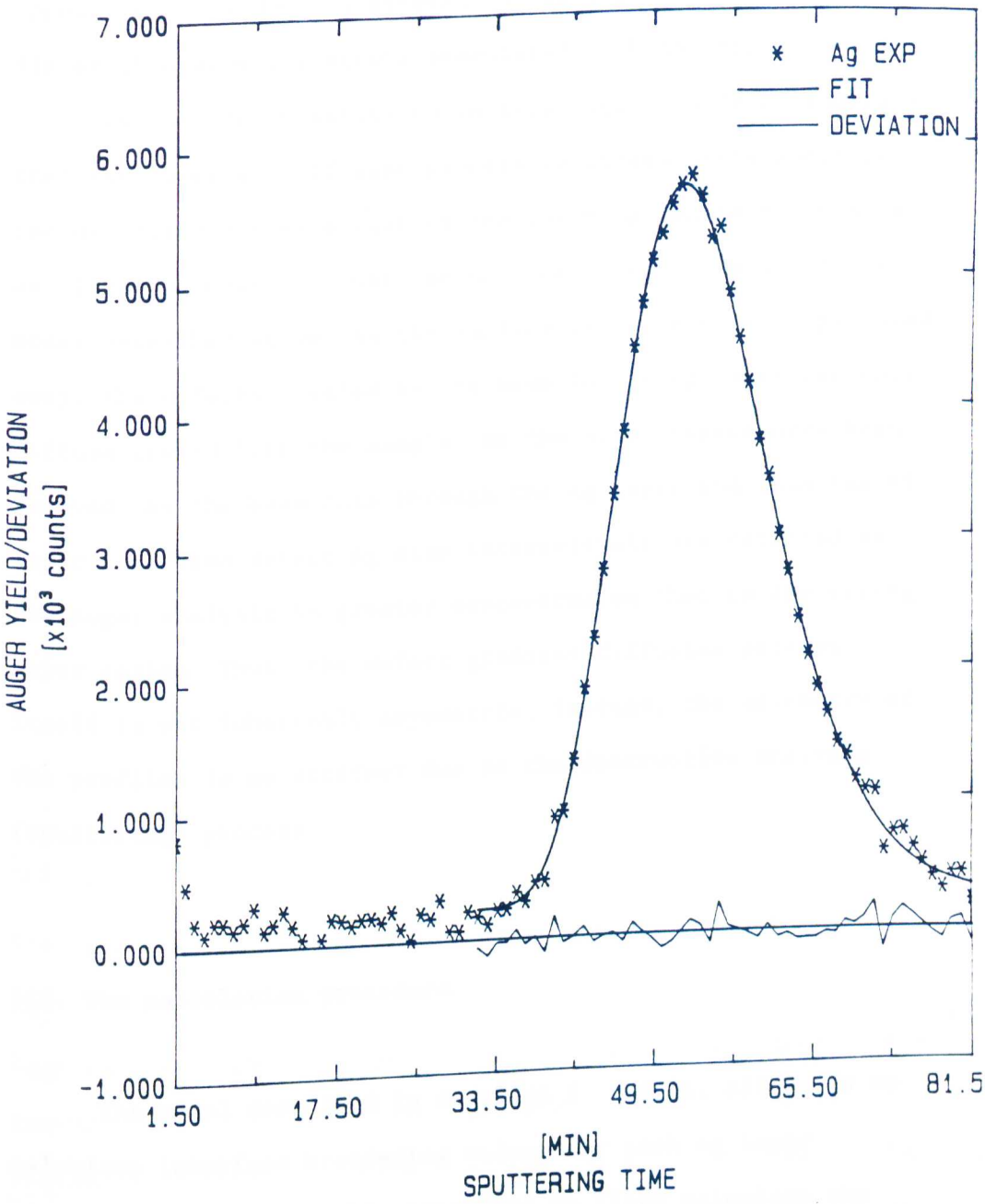

Figure 6.5 Auger depth profile of an Ag layer (E_p = 4 keV). The x-axis represents sputtering time, while the y-axis represents counts. This detailed figure is intended to show the quality of the fit. Measured points are denoted by (*), the solid line through these points represents an asymmetric Guassian fit to the data. The solid line below this peak represents the standardized residuals of the fit, which are seen to be random.

appear to be randomly scattered indicating that there are no discernible modeling errors associated with the fit.

The asymmetry exhibited in this figure tends to indicate that the observed diffusion process is biased preferentially in the direction opposite that of the incoming ion beam. This is an illusion, however, that can be understood in terms of the model described above. As the surface is successively sputtered away, the defects created by the beam in the Ag layer can only diffuse inward into the sample, as the outer layers have been removed. As the beam cuts through the Ag layer and into the Ni layer, diffused defect Ag atom interstitials are detected by the Auger analysis in greater concentration than in the pre-Ag layer region. Thus, the defect gradient diffusion process itself is not inherently asymmetric; instead, the asymmetry of the profiles is an artifact due to the destructive analysis (sputtering) process.

iii. The calculation procedure

The model described in sections i. and ii. allows us to calculate interface broadening values for each Ag layer sputtered through. In this procedure we first calculate the sputtering rate, S. Then the maximal Ag concentration and the thickness of the Ag layer are obtained. At this point, we determine z_o as the distance between the depth where the Ag

concentration starts to increase to the Ag layer itself. In the present study, we used values around 16 nm and 20 nm for z_o at 1-keV and 4-keV bombardment, respectively. Then, equation 6.8 is used to fit the experimental depth profile and c_o, D and Δz_R are determined from the fit.

The profiles are characterized using a highly specialized linear least squares fitting routine designed especially for this equation. This program is capable of making its own initial guesses, of eliminating outlying data points, of producing both symmetric and asymmetric Gaussian fits, and of fitting real data entirely without operator intervention or assistance.

The program makes its initial guesses by first searching through the profile data to determine the maximum peak data point employing a simple bubble sort algorithm. The position of this point is used as an initial guess for the z_o value, while its intensity is used as an initial guess for the quantity $C_o(4Dt+\Delta z_R)$. Equation 6.8 is then linearized by taking the logarithm of both sides and fitting the resultant equation to a second order polynomial using the data points in the peak region. As a first approximation, the value for D is held fixed at zero, yielding a symmetric Gaussian equation. The values of the coefficients of the linearized fit together with the initial guess values determined from the maximum peak point to provide initial guesses for the four parameters C_o, z_o, z_R, and

t_o, an offset parameter to adjust the time scale for each profile separately. The value of S is calculated from known layer depths and sputtering times and is entered as an input to the program. These initial guesses are then used as starting values for the specialized Gaussian fitting routine which performs a linear least squares symmetric fit, eliminating severe outliers and reperforming the fit until convergence is obtained.

This program employs the subroutine ORTHO, described in Chapter IV, to perform a Gram-Schmidt orthonormalization procedure on the corrections to the coefficients. To provide these corrections, derivatives of equation 6.8 with respect to each of its parameters were taken by hand and coded directly into the program. When convergence is reached for the symmetric fit of a given profile, the resultant parameters are then used as inputs to a second cycle of the program which allows D to vary, producing, after further outlier elimination and convergence, a set of values, with uncertainties, for each of the seven parameters used in the asymmetric Gaussian equation, including a linear background region.

The interface broadening due to surface roughness, Δz_r is then obtained from equation 6.5. Here l_e = 0.8 nm (Ag at 375 eV [123]) was used for all measurements. Values of Δz_c for various sputtering ions and energies are available from calculations based on Monte-Carlo methods[81]. The values used

here are 2 nm for E_p = 1 keV and 4 nm for E_p = 4 keV bombardment. The thermal interdiffusion in the Ag/Ni system is probably very small due to the low solubility of silver in nickel [124]. Thus Δz_d is neglected in the present calculations.

The full interface widths obtained in our measurements includes a part due to RED. This part can be characterized by the quantity

$$\Delta z_D = (8Dz_o/S)^{1/2} \qquad (6.9)$$

the "diffusion interface width" which plays an analogous role with Δz_R in equation 6.8 for $t = z_o/S$, i.e. for the time when the measurement approaches the silver layer.

D. Results and Discussion

i. The interface broadening

Examples of measurement results obtained for Ag/Ni samples using 1-keV and 4-keV bombarding ion energies are summarized in Table 6.1. The surface roughness contribution to the interface broadening is given both as results of calculations outlined in the previous section (under the label "from AES") and as obtained from light scattering measurements. The diffusion contribution to broadening is included also in

Table 6.1.

Profile Broadening as a Function of Depth

Energy	layer/depth		Δz_r [nm]		Δz_D
$[nm]=(8Dz_o/S)^{1/2}$					
[keV]		[nm]	from AES	from light scattering	
1	1	50	7.4	4.9	6.0
	2	100	-	9.7	-
	3	150	9.3	11.8	7.3
	4	200	11.0	12.9	7.7
	5	250	13.6	13.8	7.3
4	1	50	11.9	10.1	14.8
	2	100	14.8	15.1	15.6
	3	150	18.0	17.4	13.2
	4	200	15.5	18.8	13.1
	5	250	19.8	19.4	9.8

the last column of this table. While the broadening ascribed to surface roughness increases with depth, the broadening due to diffusion remains constant (with a considerable scatter of data), as expected. While it is clear that values calculated from AES depth profiles as well as those obtained from the light scattering measurement are subject to substantial scatter, the fine agreement of most of the Δz_r values is encouraging.

Depth profiles of Cr/Cr_2O_3 samples exhibit similar interface broadening with increased sputtered depth as can be seen in Figure 6.3. Though the asymmetry of these profiles appears to increase also as a function of depth, the absolute D values tended remain constant to within experimental uncertainty as successive layers were sputtered.

Examples of interface broadening at high temperatures are exhibited in Figs. 6.6-6.8. Figure 6.6 shows a depth profile of Ag/Ni at 4-kev ion bombardment performed at 102°C. This profile is very similar to the profile of Figure 6.1, taken at room temperature. The profile shown in Figure 6.7 taken at 171°C, however, is markedly different. As can be seen, the Ag profiles are very sharp in comparison to those taken at 102°C and at room temperature. Moreover, the asymmetry of these profiles is reversed, ie. the Gaussian shapes characterizing the Ag layer regions are skewed in the opposite direction, with the following edge of each profile now more abrupt than the leading

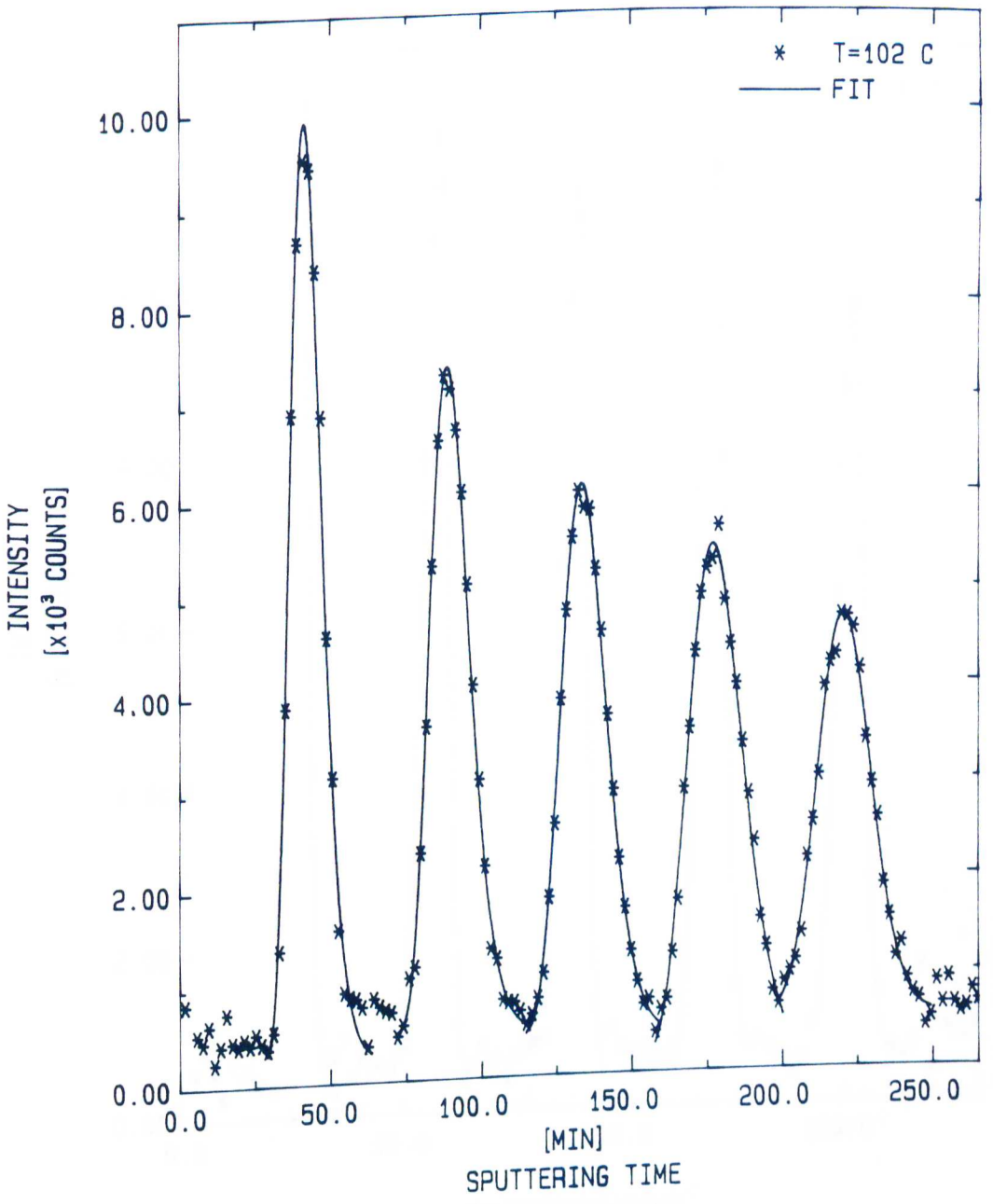

Figure 6.6 Auger sputter depth profile of Ag taken at 102°C. The axes are the same as in Fig. 6.1.

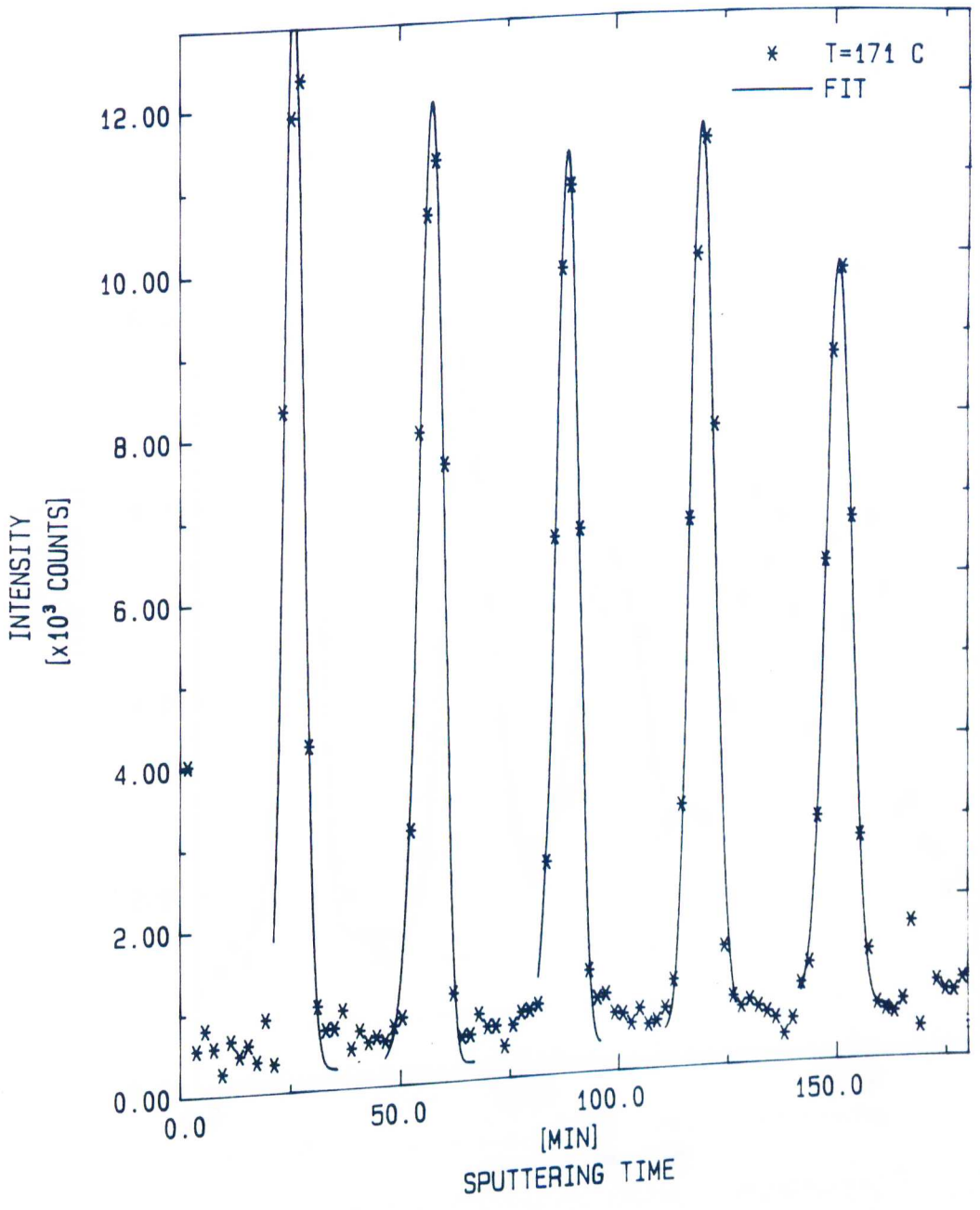

Figure 6.7 Auger sputter depth profile of Ag taken at 171°C. These interfaces are noticeably sharper than those taken at 102°C.

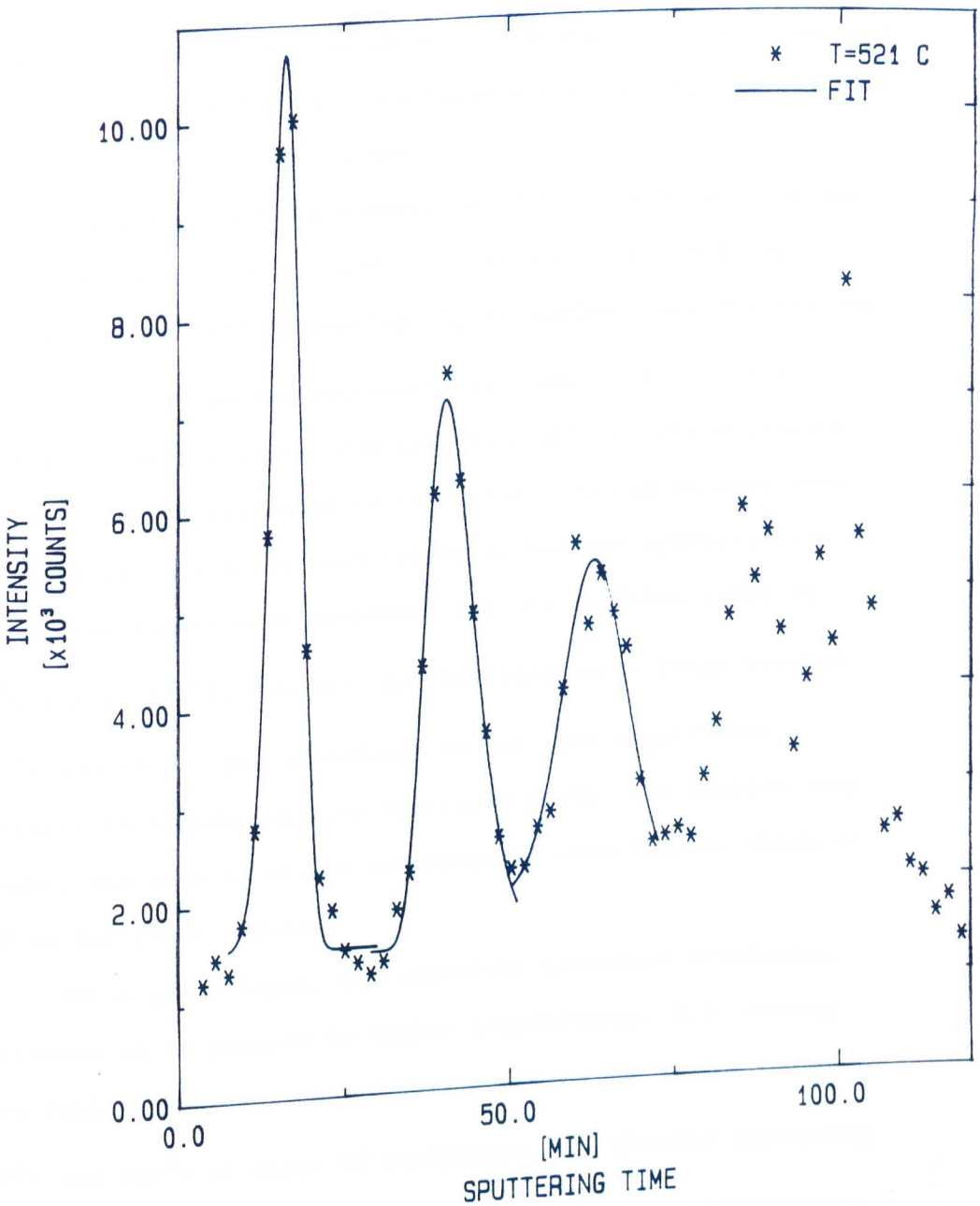

Figure 6.8 Auger sputter depth profile of Ag taken at 521°C. These profiles exhibit increased broadening compared to those of Fig. 6.7, and indicate the onset of pronounced thermal diffusion.

one. At 521°C, this situation again changes and the profiles start to exhibit more pronounced broadening as can be seen from Figure 6.8. The effect at this temperature is most probably due to a thermal diffusion process.

The results of the temperature dependent broadening are summarized in Tables 6.2 and 6.3. Table 6.2 displays the symmetric interface broadening, Z_R determined from the fitting analysis, obtained for successive Ag layer profiles, i.e. moving across the table from left to right, at the different temperatures investigated in this study. As can be seen from this figure, the interfaces tended to broaden symmetrically as successive layers were sputtered for the profiles taken at 26°C and at 102°C. However, in the temperature range between 120°C and 350°C, the interfaces do not show significant increase in broadening with sputtered depth, but instead stay roughly the same to within experimental uncertainty, which is 1 - 2 nm for these values.

For a given layer, the symmetric interface broadening decreases as we proceed to higher temperatures, i.e. moving down Table 6.2, eventually leveling off in the region between 120°C and 350°C at about 10 nanometers, and finally increasing again at 521°C. These results display an optimum temperature at which broadening is minimized, suggesting that two or more competing processes are at work, each acting to greater or

Table 6.2

Symmetric Interface Broadening with Temperature
Z_R (nm)

	Layer Number				
Temp	1	2	3	4	5
26°C	8.8	12.7	16.3	20.8	25.5
102°C	10.8	11.6	15.5	19.6	20.6
137°C	9.1	11.1	10.7	11.7	13.9
171°C	9.4	10.1	9.7	10.0	10.6
221°C	8.4	9.7	10.0	10.3	11.2
330°C	8.6	9.0	10.3	10.8	13.8
521°C	13.9	16.4	20.5		

Table 6.3

Diffusional Broadening with Temperature

$Z_D=(8Dz_o/S)^{1/2}$ (nm)

	Layer				
	1	2	3	4	5
Temp					
26°C	13.4	15.9	16.5	14.0	3.7
102°C	9.6	10.9	10.7	12.0	6.8
137°C	5.9	-4.0	-7.7	-9.0	-7.6
171°C	-0.9	-8.7	-6.6	0.0	-5.5
221°C	-6.9	-9.1	0.0	0.0	-7.9
330°C	-7.0	-5.7	-5.1	-8.7	-3.1
521°C	-9.3	13.4	0.4	-	-

lesser effect depending on the temperature regime.

Table 6.3 is a compilation of the diffusion interface widths, characterized by equation 6.9 and calculated by the fitting program, for the temperature dependent profiles arranged by layer and by temperature. Zero values for Δz_D in Table 6.3 indicate that an asymmetric Gaussian shape could not be fitted to these profiles; a symmetric fit was used instead holding D fixed at zero. Except for the fifth layer, the diffusional broadening remains constant to within experimental error for successive layers in each of the first two temperature profiles. Notice that as the temperature increases for a given layer, its diffusional broadening lessens , a surprising result for a diffusion related process. This phenomenon is exhibited in Figure 6.9, which shows plots of diffusional broadening (profile asymmetry) as a function of temperature for the first three Ag layers of the sample. As can be seen in this figure, there is a sharp transition region at $121^{o}C$ and above this temperature the broadening values are negative, i.e. the asymmetry of the profiles has reversed direction as mentioned above. The negative Δz_D values do not have physical meaning in the sense that they represent "negative diffusion broadening," but are instead artifacts of the fitting program indicative of unknown physical processes tending to skew the profiles shapes in temperature regimes

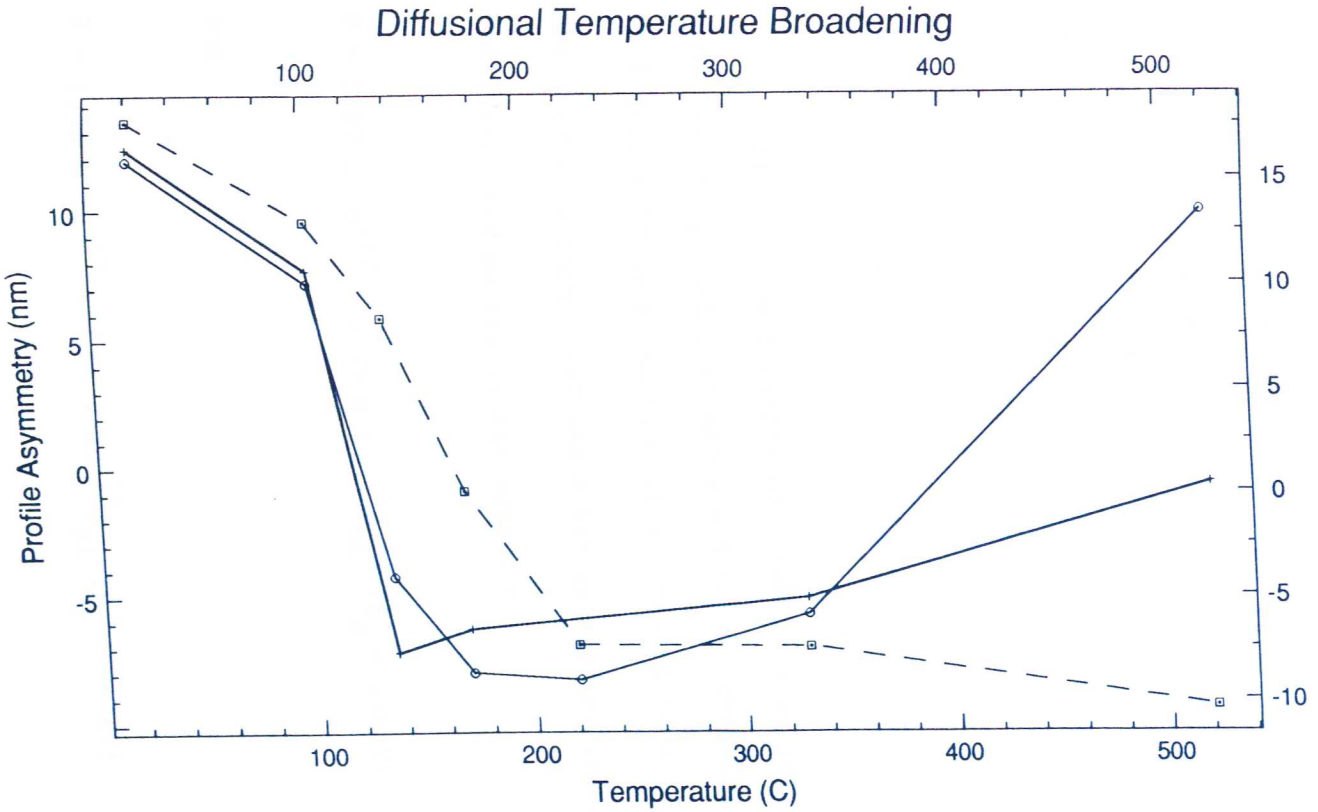

Figure 6.9 Temperature dependence of the profile asymmetry, corresponding to the diffusional broadening. The dashed line corresponds to the first Ag layer, the light solid line to the second Ag layer, and the bold solid line to the third Ag layer. There is a sharp transition region evident at 120°C, a minimum region between 120°C and 350°C, and an increased broadening region starting somewhere above 350°C.

where the radiation enhanced diffusion has subsided. One explanation for this effect, however, may be that lattice damage due to the incident radiation facilitates the diffusion of displaced Ag atoms preferentially towards the surface, an effect that is masked by RED at lower temperatures. At 521°C, the diffusional asymmetry of the profiles is observed to increase significantly, indicating the onset of substantial thermal diffusion in this region.

ii. Diffusion rates

Diffusion coefficients obtained from experimental depth profiles of Ag, using equation 6.8 to fit the data, are plotted in Figure 6.10 as a function of sputtering rates S_{Ni}. Results obtained with both 1-keV and 4-keV sputtering energies, E_p, are well described by the linear equations:

$$D = 1.22 \times 10^{-17} + 1.75 \times 10^{-15} S_{Ni} \quad (E_p = 1\text{-keV}) \qquad (6.10)$$

and

$$D = 1.35 \times 10^{-17} + 9.05 \times 10^{-15} S_{Ni} \quad (E_p = 4\text{-keV}) \qquad (6.11)$$

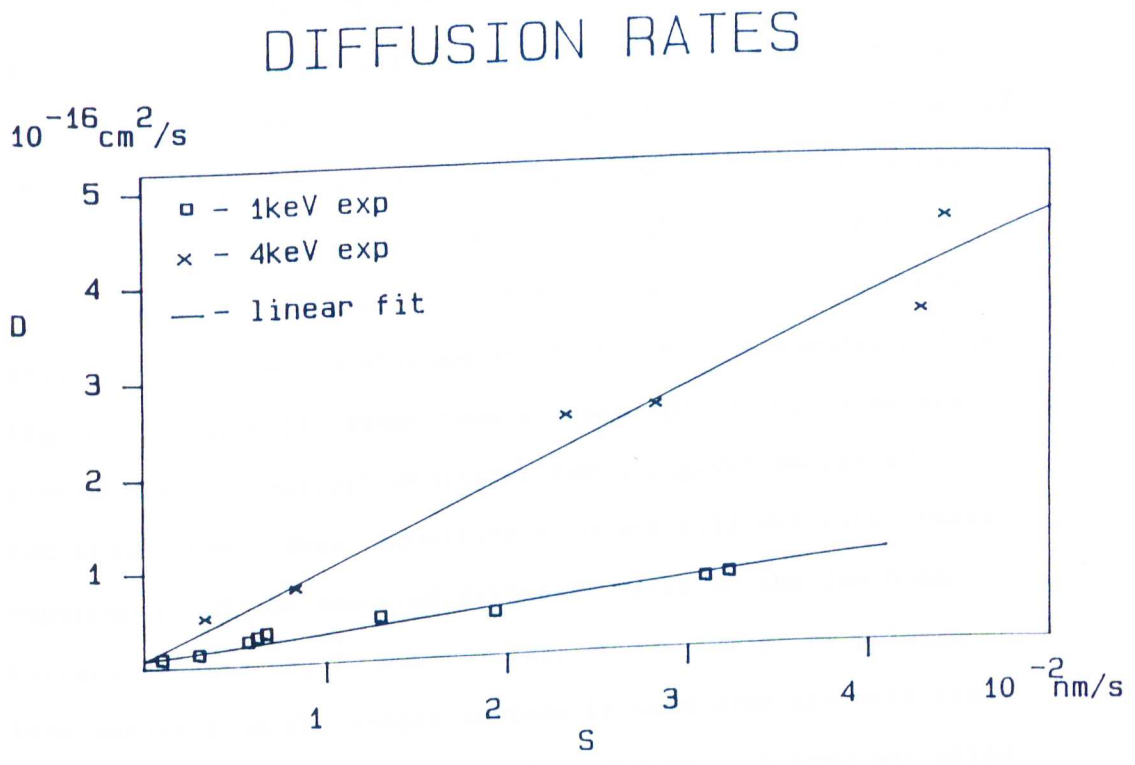

Figure 6.10 Plot of diffusion rate versus sputtering rate for both 1-keV and 4-keV incident ions. Each point corresponds to one profile, ie. five interface layers. The solid lines represent least squares fits to a linear equation.

where D is in cm^2/s and S_{Ni} is in nm/s. In Figure 6.10, data obtained in the same sputter profile (constant sputtering rate) from a number of Ag layers at different depths are shown as a single point, with an error bar corresponding to the scatter of the sputtering rate and diffusion rate of the various layers. The diffusion rates are plotted against the sputtering rates rather than against current densities, as the latter are not easily measurable. In discussion of the results summmarized in Figure 6.10 we will assume however that sputtering rates are proportional to current densities for any given energy of bombarding ions. Thus, equations 6.10 and 6.11 describe linear dependences of the measured diffusion rates on the ion beam current density or, in other words, on the number of primary ions incident on the sample surface in unit area and unit time. The quality of the data presented in Figure 6.10 does not allow us to tell unambiguously whether the small D(0) values (which correspond to a linear extrapolation of S_{Ni} to zero, about 1.3 x 10^{-17} cm^2/s) are real or are due to measurement errors. Nevertheless, we will assume that, within the accuracy of our model, the RED rates are essentially proportional to the sputtering rates. For comparison purposes, the diffusion coefficient of the grain boundary diffusion of Ag in Ni extrapolated from high temperature data[125] is about D_b = 3.3 x

10^{-19} cm^2/s at 300°K, a value considerably smaller than obtained here for the RED rate.

As mentioned in the introduction, RIS measurements have been carried out on similar Ag/Ni samples under similar sputtering conditions[99]. The RIS rates, k, determined in those experiments were found to be quite linear with the subsurface concentration of Ag and were found to be $k_1 = 2.8 \times 10^{-3}$ s^{-1} and $k_4 = 1.2 \times 10^{-2}$ s^{-1} for 5% Ag and for 1-keV and 4-keV bombardment, respectively. Assuming that RED is the rate determining factor in the segregation kinetics, one can determine the segregation rate from the diffusion rate according to a simple relation that expresses that the segregation rate as the number of atoms in the source of the diffusion multiplied by the diffusion coefficient:

$$k = cN_{ML}D \tag{6.12}$$

where c is the fractional concentration and N_{ML} is the number of atoms in a monolayer (for Ag, $N_{ML} = 1.2 \times 10^{15}$ cm^{-2}). With the above segregation rates we obtain $D_1 = 4.7 \times 10^{-17}$ cm^2/s and $D_4 = 1.9 \times 10^{-16}$ cm^2/s, respectively. (The sputtering rates were $S_{Ni} = 7 \times 10^{-3}$ nm/s and $S_{Ni} = 3.1 \times 10^{-2}$ nm/s for 1-keV

and 4-keV ions, respectively.) These diffusion coefficients, although obtained from a completely different experimental approach and measurement, are in reasonable agreement with those obtained in the present study; differences may stem from the fact that the segregation rates are determined with no ion sputtering during the diffusion.

Very little reliable data exists for the sputtering yield of Ni at 1-keV Ar^+ bombardment, and no data are available at 4-keV. Therefore, the following calculations are of limited accuracy but are probably good estimates. Taking $Y_{Ni,1} = 2.16$ atoms/ion[32], for 1-keV and assuming that $Y_{Ni,4} = 2Y_{Ni,1}$ for 4-keV, one can calculate the conversion factors between the sputtering rates and the current densities. This leads to the following expressions for the diffusion coefficients, based on equations 6.10 and 6.11:

$$D = 6.4 \times 10^{-31} v \qquad (E_p = 1\text{-keV}) \qquad (6.13)$$

and

$$D = 6.6 \times 10^{-30} v \qquad (E_p = 4\text{-keV}) \qquad (6.14)$$

where D is again in cm^2/s, and v is the ion impact density in ions/cm^2s.

A similar characterization of the temperature dependence of D is not straightforward. Typically, for a diffusion controlled process D varies with temperature according to the relation[110]

$$D = D_o \exp(-Q/kT) = D_o \exp((B - E_m))/kT) \qquad (6.15)$$

where Q is the activation energy, E_m is the migration energy of the Ag atoms responsible for the diffusion, and B is the binding energy of the defect complexes, discussed below. In the usual case, ln D is plotted against 1/T to provide a value for the slope -Q /k. Such a plot is shown in Figure 6.11. The value of slope Q/k, determined from a least squares fit (the dashedline in Figure 6.11), yields a value for the activation energy Q of 0.07 eV. However, it is not possible to further separate this energy into its component parts, i.e. the migration energy E_m , or the binding energy, B, of defect complexes. Instead, Q provides an upper limit on the value of the defect binding energy.

E. Theory and Discussion

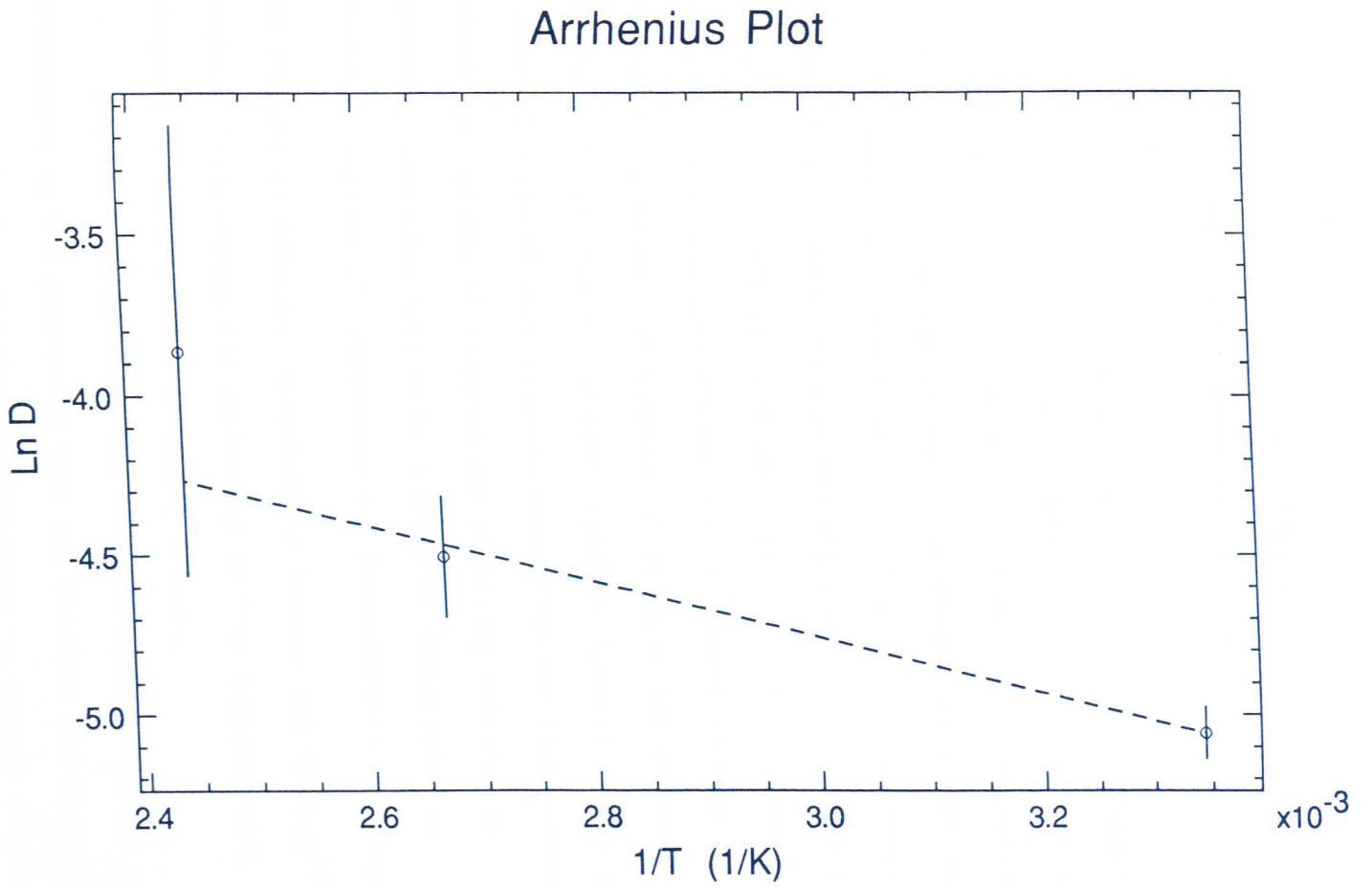

Figure 6.11 Arrhenius plot of Ln D versus 1/T. The dashed line represents a linear least squares fit to the data. The negative slope of this line is indicative of a process that is deactivated with increasing temperature.

The microscopic theory of radiation enhanced diffusion in solids has been described by Dienes and Damask[110]. According to this theory, the mechanism for diffusion is the migration of defects created by ion irradiation. Such defects may be either point defects, atomic crystal lattice vacancies or interstitials, or complex defects, combinations of homogeneous or inhomogeneous point defects. Defects can disappear or anneal through two primary mechanisms, recombination and migration to sinks. Simple recombination may occur between an atomic vacancy and its geminate interstitial, thus eliminating both defects, or an interstitial or vacancy may migrate until it finds a vacancy or interstitial with which it can anneal. Vacancies, interstitials, and clusters may also disappear through migration to sinks, the simplest of which is the external surface of the crystal. In real crystals, however, there exist internal surfaces such as grain boundaries and dislocations, which are capable of trapping and annealing defects. In general, vacancies tend to be trapped at dislocation or boundary regions of compression and interstitials are trapped at regions of dilation. According to Bardeen and Herring[126], crystal dislocations are equivalent to free surfaces with respect to their ability to anneal defects.

For the case in which the ion beam current density and consequent defect generation rate are constant and in which the primary mechanism of defect annihilation is through random walk migrations to sinks, the annealing process has a time

dependence equivalent to that of a first order chemical reaction,

$$dn/dt = -Kn \tag{6.16}$$

where n is the number of defects remaining in the metal and K is a constant rate of defect concentration production. The rate of the radiation enhanced diffusion is then given by

$$D = \frac{Kf_{Ag}\lambda_{Ag}^2}{Rf_d\lambda_d^2} \tag{6.17}$$

where R is a geometrical constant that depends on the location and shape of the sinks where defects annihilate, f_{Ag} and f_d are the jump frequencies of Ag atoms and defects, respectively, and λ_{Ag} and λ_d are the jump distances. This expression for the diffusion rate does not include any contribution from thermal processes which, at room temperature, are known to be quite small.

The defect production rate for a given ion bombardment energy should be proportional to the bombarding ion current density, assuming the defects are produced by ion bombardment and each ion impact can be considered as an individual event. In the present experiments, sufficiently low current densities were used ($<<1$ mA/cm^2) so that this requirement was fulfilled

and indeed a linear relationship has been found to exist between the diffusion rate observed and the incident ion beam current density. If Y_d is the number of defects produced per impinging ion, then

$$K = Y_d v V_{at} / z_o \tag{6.18}$$

where V_{at} is the atomic volume of the target atom and z_o is the total depth altered by defects as defined in context with equation 6.6. The following considerations will be aimed at the assessment of Y_d, the number of defects produced per primary ion, because there are some data available concerning this quantity. Combining equations 6.17 and 6.18 one obtains

$$Y_d = \frac{D z_o R f_V \lambda_V^2}{v V_{at} f_{Ag} \lambda_{Ag}^2}, \tag{6.19}$$

where D/v, z_o, and V_{at} are now known quantities.

The defect annihilation mechanism is not expected to depend on the energy and/or density of the primary ions, provided that it does not involve the recombination of defects with each other which would require the annealing process to be described by a second-order differential equation. The linear relationship between the sputtering rates and the RED rates

makes it possible to exclude this recombination mechanism. Since there are no data available for f and λ values, it is reasonable to initially assume that $f_{Ag}=f_V$ and $\lambda_{Ag}=\lambda_V$. There is wide latitude in estimating R. Let us assume as described by the theory of Dienes and Damask, that defects are annihilated at grain boundaries, and that grain boundaries can be represented simply by spheres, each with a radius of r≃4nm. Then it is clear that by diffusion point defects should not be able to migrate beyond 4-5 nm from the point of their production by Ar ions. Yet ranges of up to 15 nm have been observed in this experiment. Furthermore, the above estimates for the metallic grain boundary size and structure can be used to calculate the geometrical constant R in the Damask theory which is given by $R = \pi^2/r^2 \simeq 6.2 \times 10^{13}$ cm^{-2}. Using these values, a time constant of

$$t_o = (RD)^{-1} \simeq 60 \text{ s} \qquad (6.20)$$

would follow for $D = 2.5 \times 10^{-16}$ cm^2/s. This value agrees well with a previous measurement on Ag/Ni multilayers[99], in which processes generated by ion bombardment were observed to result in segregation time constants on the order of minutes. If indeed the defect annihilation time, t_o, were approximately equal to the segregation time constant, then one would expect

to see deviations from first order kinetic behavior. Such deviations are not observed, indicating that the defects involved in RED, described here, are annealed more slowly. These considerations lead to the postulation that the observed radiation enhanced diffusion is not in fact due to the migration of point defects, i.e. simple vacancies or interstitials, but rather to defect complexes, possibly associated with trapped Ar atoms. Ar atoms are a likely source mechanism for the long range diffusion observed here since, due to their inertness, they tend to be unaffected by the lattice structure of the crystal and are known to diffuse over long ranges in metallic crystalline structures. Simple point defects are likely to encounter implanted Ar impurity atoms during their random migrations and can become bound to these impurities to form complexes provided there is a positive binding energy between them. Such complexes would probably not easily be annealed due to their large size and higher activation energies of motion. The primary mechanism for annealing of such clusters would likely be through their dispersion into simpler and more mobile point defects followed by subsequent annealing of the point defects themselves.

As it appears that segregation time constants are significantly shorter than reasonable defect annihilation times, it is not unreasonable to assume that defects are migrating to sinks more slowly than silver atoms, implying that $f_d \ll f_{Ag}$. In order to obtain a numerical assessment of the

number of defects produced by an impinging ion (Y_d), it is necessary to make an assumption concerning the above jump frequency ratio and as a first estimate one may suppose the frequencies to differ by an order of magnitude, i.e. $f_{Ag} = 10 \times f_d$, while retaining the belief that the jump distances are equivalent. From the experimental data, the following values for Y_d are obtained: $Y_{1d} = 0.38$ defect/ion (1-keV) and $Y_{4d} = 4.8$ defect/ion (4-keV). These estimated Y_d are based on the assumption that the Ag diffusion is related to the production of complex defects whose annealing time constants are long compared to that of the point defects; consequently these point defects do not contribute to the observed diffusion rates. Athough no experimental values exist for Y_d in Ag/Ni, results obtained by computer simulation techniques do exist for solids bombarded by keV ions and indicate that our values of Y_d are considerably lower, generally speaking, by an order of magnitude[114,127]. These simulations, however, are concerned primarily with the generation of point defects, which would be expected to be produced in greater numbers than cluster defects, which are themselves composed of several or many point defects. Furthermore, our experimental values for the range of radiation damage playing role in RED (z_o) far exceed the mean values of the depth distribution of defects obtained in computer simulation calculations, lending further support to

the view that complex rather than point defects are responsible for the observed enhanced diffusion.

The experimental investigation into the temperature dependence of diffusion in the Ag/Ni system also is consistent with the model described above. First, it allows us to exclude simple thermal diffusion as the primary mechansim for the observed interface broadening since thermal diffusion would be expected to increase with increasing temperature according to equation 6.15. However, the interface widths decrease sharply as the temperature is increased over 120°C. This phenomenon indicates that thermal diffusion is not the primary diffusion mechanism at or slightly above room temperature. Thermal diffusion does, however, become significant as the samples are heated to higher temperatures in the region near 520°C, as can be seen in Figure 6.8.

Thermodynamically, the equilibrium point defect concentration in a crystal follows a simple relation derived from entropical considerations[110]

$$n/N = e^{-Q/kT} \tag{6.21}$$

where n is the number of defects, N is the number of lattice sites in the crystal, and Q is the activation energy for a single point defect. Therefore, as the temperature rises, the atomic fraction of point defects in the crystal should

increase. Further, as the temperature increases, it becomes slightly easier for a bombarding Ar ion to displace an atom from its lattice site since the atom posseses a higher vibrational energy, consequently creating a larger number of defects for a given ion impact energy. Lastly, it is known that the range of defects tends to increase with increasing temperature[110]. It is therefore surprising that the interface widths become sharper as the sample is heated, considering that we expect more defects to be created and for them to have a longer range.

Competing with defect generation effects, however, are temperature dependent annealing effects as well as topographical reduction effects associated with enhanced surface diffusion at higher temperatures. Many point defects created by ion bombardment are actually closely separated geminate vacancy-interstitial pairs. The recombination of such pairs is determined by a first order kinetic equation since the defects do not have to migrate or interact with other separately generated defects to recombine. As the temperature increases, interstitals combine with their near neighbor geminate vacancies as the activation energy for this process is reached. Clearly, geminate defect pairs that recombine quickly enough are not able to form complexes with Ar atoms encountered through migration. Furthermore, higher temperatures may provide sufficient energy to disperse the Ar atom anchored defect complexes responsible for the observed RED. At present, it is

not possible to distinguish between these two annealing processes at elevated temperatures.

An alternative model for the radiation enhanced diffusion process would involve the migration of Ag atoms over pathways formed by complex defects generated through ion bombardment. In this model, complex defects themselves do not diffuse, but instead act as channels or conveyors for diffusing silver atoms. RED would still be expected to disappear in this model when the activation energy for complex defect dispersal has been reached at elevated temperatures..

As described earlier, topographical development is known to contribute to the interface broadening observed in our profiles. As the temperature is increased, the rate of surface diffusion is likewise increased. This diffusion could well be responsible for the erosion of the surface microstructures observed at room temperatures, consequently causing lower symmetric broadening values to be observed in our depth profiles at high temperatures. The phenomenon of enhanced surface diffusion leading to reduced surface microstructure at elevated temperatures has in fact previously been reported by Kuhlen and Jager[128] in a study of silver layers evaporated onto polycrystalline copper substrates. Together, the dual effects of increased defect annealing and of enhanced surface diffusion causing microstructure attenuation are probably responsible for the observed sharpening of interface profiles at elevated temperatures.

The sharp drop in diffusion coefficients occuring between 102°C and 137°C is indicative of a transition. If this transition is taken to occur at 120°C, it would correspond to an energy of 3kT, or about 0.1 eV, imparted to each atom in the crystal. It may be that this energy, per point defect, is sufficient to disperse the defect complexes likely responsible for RED. At any rate, this observed transition behaviour can be described mathematically using Maxwell-Boltzmann statistics, as is shown in equation 6.15. This mathematical model takes into account the various competing processes of ion induced defect annealing and of enhanced thermal diffusion as the temperature is varied, assuming that these processes are sufficient in themselves to account for the observed temperature dependence.

F. Summary

Radiation enhanced diffusion measurements have been carried out by Auger sputter depth profiling of Ni/Ag multilayered thin-film structures in order to determine the effect of room temperature RED on the interface broadening in sputter depth profile measurements. The interface broadening observed is determined by a number of factors, the main two being roughening and RED in the case of this system. These two factors were found to be separable using the assumption that

roughness leads to symmetric profile shape, while asymmetry is caused by diffusion. This concept is confirmed by interface broadening results which increase with depth (for subsequent Ag layers) for surface roughness, but remain independent of depth for diffusion (c.f. Table I). The fact that depth profiles of Cr/Cr_2O_3 multilayered thin film structures exhibit similar broadening effects, demonstrates that the observed processes are not unique to the sputtering of the Ag/Ni system.

Effective diffusion rates were determined for primary ion energies 1-keV and 4-keV as $1.22 \times 10^{-17} + 1.75 \times 10^{-15} S_{Ni}$ $[cm^2/s]$ and $1.35 \times 10^{-17} + 9.75 \times 10^{-15} S_{Ni} [cm^2/s]$, respectively, where S_{Ni} is the sputtering rate [nm/s]. These values are substantially higher than the grain boundary diffusivity of Ag in Ni at room temperature and are in acceptable agreement with RIS rates determined in previous experiments. Defect complexes, rather than point defects are likely to play important role in RED. It is important to note that the range of the RED process (i.e. the range of the defects responsible for it) is considerably higher than the range of the ion mixing.

Temperature dependence experiments demonstrate that thermal diffusion was clearly not the primary mechansim for the diffusion at low temperatures. Further, the fact that interfaces became sharper as the temperature was raised indicated that defects responsible for the RED process tended

to be dispersed or annealed out at relatively low temperatures, about 120 ^{o}C.

Beyond the particular findings concerning the Ni/Ag and Cr/Cr_2O_3 systems, our study suggests that RED may contribute substantially to interface broadening in some multicomponent systems with relatively low activation energies of diffusion. It is likely that radiation enhanced diffusion generally takes place in many other systems, especially when high current densities are used for depth profiling, being more like a rule, than an exception.

VII. CUMULATIVE SUMMARY

A summary of results is presented here along with possible avenues for future research stemming from this work.

The first chapters presented results of Monte Carlo code simulations of the sputtering process using the program EVOLVE, developed at the University of Maryland. Contours of constant recoil production density were observed to depend in shape on both the angle of incidence and energy of the bombarding ion beam. The generation method of segregating recoil groups was applied to demonstrate a number of significant features of the collision cascade. It is concluded from this study that the recoil activity grows in size and tends to move away from the target surface with increasing time. It is further concluded that the majority of sputtered atoms originate from early generations and are produced from sites in relative close proximity to the entry point of the incident bombarding ion. This study raises the possibility of a drop in the local potential binding energy, a parameter of well known importance to the sputtering yield.

The results of computer code simulations of ion bombardment of a Ga-In eutectic alloy were presented in Chapter II. A depth dependent displacement energy model was introduced and shown to produce results in good agreement with experimentally measured sputtering yields. It is noted from

this study that angular distributions of sputtered particles tend to exhibit increasingly peaked angular exit directions with increasing depth of origin. A future direction of investigation would be to evaluate angular sputtering yield distributions as a function of the incident angle of the bombarding ion beam for comparison to experimental results for varying angles of incidence. This information would be useful to researchers performing laser induced ionization studies of velocity distributions of sputtered atoms.

Chapter IV described the use of the program LOGIT for the parameterization of the sputter depth profile interface region of thin film multilayered structures. The LOGIT program was shown to be both accurate and reliable in the characterization of real experimental depth profiles. Use of the logistic function to parameterize an error function demonstrates that it is not possible to distinguish between the logistic function and the error function at our current level of experimental accuracy. The statistics assocciated with the fits returned by this program have permitted the verifiable identification of trends associated with the data for a given multilayered depth profile structure. These trends are the exhibition of increasing interface broadening with sputtered depth and the constancy of profile asymmetry as deeper interface regions are profiled. Use of the LOGIT program has allowed the successful intercomparison on sputter depth profile data made under varying experimental conditions.

A future area of investigation for LOGIT would be the comparison of profiles done under the same experimental conditions, but employing different materials. Another avenue for future research would be the comparison of the degree of profile asymmetry under varying experimental conditions on a uniform target sample. A uniform, consistent set of such measurements might help to relate the asymmetry parameters given by LOGIT to possible causitive physical processes such as radiation induced diffusion or cascade mixing. LOGIT may also be successfully employed in the comparison of experimental depth profiles to Monte Carlo computer simulations of ion bombardment of multilayered thin film structures.

In Chapter V, a systematic evaluation of the effect of ion bombardment parameters on the interface resolution versus depth of sputter profiles has been presented. This evaluation was performed in a consistent manner on a uniform set of multilayered thin film structures using the same materials under varying experimental conditions. Parameters investigated included: ion energy, angle of incidence, and current density. This study demonstrates that the extent of interface broadening depends not only on the elemental composition of the sample used, but also on the experimental conditions under which sputtering is conducted. An explanation for the broadening is given in terms of physical processes believed to occur during the sputtering process. This study concludes that optimization

of interface depth resolution can be achieved through variance of the conditions of profiling.

It would be of interest in a future experiment to vary the experimental conditions of the sample itself during the sputtering process. The generation of a consistent set of metal/metal interface profiles performed while rotating the target or heating it to elevated temperatures would be of considerable use in elucidating the mechanisms and processes which occur during sputtering.

A study of radiation enhanced diffusion (RED) in a Ag/Ni multilayered system was introduced in Chapter VI. This study employed the use of an asymmetric Gaussian equation to model the broadening of the Ag marker layer during the ion bombardment process. The quality of the fit of this equation to the experimental depth profile data demonstrates the accuracy of this model. Fits to this equation allow the deconvolution of the symmetric interface broadening from the asymmetric interface broadening. Through comparison to light scattering experiments it was demonstrated that the symmetric broadening is due to the development of surface topography. Plots of the diffusion coefficient obtained from the fits versus the ion current density under which the samples were bombarded demonstrate a linear relationship between defect production rate and diffusion coefficient as expected from the theory of microscopic diffusion.

Chapter VI also includes a study of the effect of sample temperature on the interface profile width. This investigation attests to a significant decrease in the profile broadening at elevated sample temperatures, indicating that the processes contributing to this broadening are either limited or deactivated at high temperatures. This is an important discovery as use of this technique will likely allow future improvement in the ability to resolve interface regions during sputter depth profiling.

It would be of interest to perform low temperature sputering of the Ag/Ni samples as a further check on the accuracy of the microscopic model of Dienes and Damask. At low temperatures, defects would not be expected to diffuse rapidly to sinks. On the other hand, activation energies for the migration of Ag atoms may not be reached in this regime leading to the lessening or elimination of RED. It would be of interest to observe which of these effects predominates, and whether other effects come into play under these new conditions. Thus, low temperature experiments would not only help to corraborate old theories, but may help to provide new insights as well.

BIBLIOGRAPHY

1. J. K. Hirvonen, J. Vac. Sci. Tech. 15 (1978) 1662
2. M. L. Roush, O. F. Goktepe, T. D. Andreadis, G. A. Pertmer, and F. Davarya, Transactions American Nucl. Soc. Winter Meeting, 1981.
3. D. G. Swartzfager, S. B. Ziemecki, and M. J. Kelley, J. Vac. Sci. Tech., 19, (1981) 185
4. R. S. Li and T. Koshikawa, Surface Science, 151, (1985) 459
5. D. Marton and J. Fine, Thin Solid Films, 151 (1987) 433-439
6. G. Falcone and P. Sigmond, Appl. Phys. 25 (1981) 307.
7. H. Oechsner. Appl. Phys. 8 (1975) 185.
8. R. Shimizu, Proc. 7th Intn. Vac. Congr. and 3rd Intn. Conf. on Solid surfaces, Vienna (1977) p. 1417.
9. T. Okutani, M. Shikata, S. Ichimura and R. Shimizu, J. Appl. Phys. 51 (5) (1980).
10. H. Oechsneer, Z. Phys. 238 (1970) 433.
11. M. L. Roush, T. D. Andreadis and O. F. Goktepe. Rad. Eff. 55 (1981) 119.
12. M. L. Roush, F. Davarya, O. F. Goktepe and T. D. Andreadis, Nuclear Inst. Meth. 209/210 (1983) 67.
13. D. E. Harrison Jr., N. S. Levy, J. P. Johnson III, and H. M. Effron, J. Appl. Phys. 39 (1968) 3742
14. D. E. Harrison Jr., W. L. Moore Jr., and H. T. Holcombe, Rad. Eff. 17 (1973) 167.

15. M. T. Robinson, K. Rossler, and I. M. Torrens, J. Chem. Phys. 60 (1974) 680

16. M. T. Robinson and I. M. Torrens, Phys. Rev, 9 (1974) 5008

17. G. Betz, R. Dobrojensky, and F. P. Vichbock, Int. J. Mass. Spectrom. Ion Phys. 6 (1971) 451

18. T. Ishitani and R. Shimuzu, Appl. Phys. 6 (1974) 241

19. L. G. Haggmark and W. D. Wilson, J. Nucl. Mater., 76 & 77 (1978) 149

20. J. P. Biersack and L. G. Haggmark, Nucl. Inst. Meth. 174 (1980) 257

21. T. Ishitani, R. Shimuzu, and K. Murata, Phys. Stat. Sol. (b) 50 (1972) 681

22. S. T. Kang, R. Shimuzu, and T. Okutani, Jap. Appl. Phys. 18 (1979) 1987

23. M. L. Roush, T. D. Andreadis, F.Davarya and O. F. Goktepe, Appl. Surf. Sci. 11/12 (1982) 235.

24. M. L. Roush, O. F. Goktepe, T. D. Andreadis and F. Davarya, Nucl. Instr. and Meth. 194 (1982) 611.

25. H. H. Andeersen, in. Proc. 10th Yugoslavian Summer School and Aymp. on Ionized Gases, ed. M. Matic (Boris Kidric Inst. Nucl. Sci. Belgrade, 1980) p. 421.

26. M. Hou and M. T. Robinson, Appl. Phys. 18 (1979(381.

27. J. Lindhard and M. Scharff. Phys. Rev. 124 (1961) ;28.

28. H. H. Andersen, Appl. Phys. 18 (1979) 131.

29. P. Sigmund, Appl. Phys. Lett. 25 (1974) 169.

30. G. Carter, Rad. Effects Lett 50 (1980) 105.

31. D. A. Thompson, Rad. Effects 56 (1981) 105.

32. G. Carter, Nucl. Instr. Meth. 209/210 (1983) 1.

33. D. A. Thompson, J. Appl. Phys. 52 (1981) 982.

34. F. Falcone and P. Sigmund, Appl. Phys. 25 (1981) 307

35. C. J. Maggiore, Nucl. Instr. Meth. 191 (1981) 199.

36. D. S. Kyser, N. S. Viswanathan, J. Vac. Sci. Technol. 12 (1975) 1305.

37. P. Sigmund, Phys. Rev. 184 (1969) 383

38. P. Sigmund, A. Oliva, and G. Falcone, Nucl. Instr. Methods 194 (1982) 541.

39. M. F. Dumke, T. A. Tombrello, R. A. Weller, R. M. Housley and E. Cirlin, Surf. Sci. 124 (1983) 407

40. H. H. Anderson, V. Chernyash, B. Stenum, T. Sorenson and H. J. Whitlow, Surf. Sci. 123 (1982) 39.

41. K. Besocke, S. Berger, W. O. Hofer and V. Littmark, Rad. Effects 66 (1982) 35.

42. J. M. Lambert, IEEE Transactions on Nuclear Science NS-120 (1983) 1285.

43. M. T. Robinson and I. M. Torrens, Phys. Rev. B9 (1974) 5010

44. W. Eckstein and J. Biersack, Nucl. Instr. Meth. B2 (1984) 550.

45. M. L. Roush, T. D. Andreadis, F. Davarya, And O. F. Goktepe, Rad. Effects 55 (1981) 119.

46. M. L. Roush, T. D. Andreadis, F. Davarya and O. F. Goktepe, Nucl. Instrum. Meth. 191 (1981) 135.

47. H. H. Andersen, in: Ion Implantation and Beam Processing, eds., J. S. Williams and J. M. Poate (Academic Press, Sydney, Australia) (1984).

48. O. F. Goktepe and M. L. Roush, Nucl. Inst. Meth. B7/B8 (1985) 803.

49. R. Kelly, Nucl. Instr. Meth. Phys. Res. B18 (1987) 388.

50. J. Biersack, W. Eckstein, Appl. Phys. A (1984) 73.

51. H. H. Andersen, Appl. Phys. 18 (1979) 131.

52. M. T. Robinson in: Topics in Applied Physics, Sputtering by Particle Bombardment I, ed., R. Behrich (New York, 1981) 78

53. H. H. Andersen, H. L. Bay in: Topics in Applied Physics, Sputtering by Particle Bombardment I, ed., R. Behrich (New York, 1981) 145.

54. K. B. Cheney and E. T. Pitkin, J. Apl. Phys. 36 No. 11 (1965) 3542.

55. R. Kelly, Nucl. Instrum. Meth. Phys. Res. B14 (1986) 421

56. S. Hoffmann, in Practical Surface Analysis by Auger and X-ray Photoelectron Spectroscopy, edited by D. Briggs and M. P. Seah (Wiley, Chichester, 1983), p. 141.

57. M. P. Seah and C. P. Hunt, Surf. Interface Anal. 5, 33 (1983).

58. M. P. Seah and M. E. Jones, Thin Solid Films 115, 203 (1984).

59. S. Hofman and J. M. Sanz, in Thin Film and Depth Profile Analysis, edited by H. Oechsner (Springer, Berlin, 1984). p. 141.

60. J. Fine, P. A. Lindfors, M. E. Gorman, R. L. Gerlach, B. Navinsek, D. F. Mitchell, and G. P. Chambers, J. Vac. Sci. Technol. A 3, 1413 (1985).

61. P. S. Ho and J. E. Lewis, Surface Science 55 (1976) 335.

62. J. M. Sanz and S. Hofmann, Surface and Interface Analysis, Vol. 5, No. 5 (1983) 210.

63. M. P. Seah and C. Lea, Thin Solid Films, 81 (1981) 257.

64. M. P. Seah, H. J. Mathieu, and C.P. Hunt, Surface Science 139 (1984) 549.

65. D. Marton, J. Laszlo, J. Giber and F. G. Rudenauer, Vacuum, 35 (1985) 523

66. J. Giber, D. Marton, and J.Laszlo, Nucl. Instr. and Meth. Phys Res. B18 (1987) 433

67. P. J. Walsh, Algorithm 127, ORTHO, Communications of the ACM 5, 511 (1962).

68. R. H. Wampler, J. Res. Natl. Bur. Stand. 73B 59 (1969).

69. H. H. Andersen, Appl. Phys. 18, 131 (1979).

70. S. Hofmann, Surf, Inteerface Anal. 2, 148 (1980).

71. P. H. Holloway and R. S. Battacharya, Surf. Interface Anal. 3, 118 (1982).

72. C. W. Magee and R. E. honig, Surf. Interface Anal. 4, 35 (1982).

73. G. Carter , A. Gras-Marti, and M. J. Nobes, Radiat. Eff. 62,119 (1982).

74. M. P. Seah and C. P. Hunt, Surf. Interface Anal. 5, 33 (1983).

75. M. P. Seah, Vacum 34, 463 (1984).

76. H. J. Mathieu, D. E. McClure, and D. Landolt, Thin Solid Films 38, 281 (1976).

77. S. Hoffmann, J. Erlewein, And A. Zalar, Thin Solid Films 43, 275 (1977).

78. S. Hofmann and S. Zalar, Thin Solid Films 60, 201 (1979).

79. C. F. Cook, Jr., C. R. Helms, and D. C. Fox, J. Vac. Sci. Technol. 17,44 (1980).

80. J. Fine, B. Navinsek, F. Davarya, and T. D. Andreadis, J. Vac. Sci. Technol. 20, 449 (1982).

81. F. Davarya, M,. L. Roush, J. Fine, T. D. Andreadis, and O. F. Gokrwpw, J. Vac. Sci. Technol. A 1,467 (1,983).

82. C. P. Hunt and M. P. Seah, Surf. Interface Anal. 5, 199 (1983).

83. M. P. Seah, H. J. Mathieu, and C. P. Hunt, Surf. Sci. 139, 549 (1984).

84. R. E. Honig and C. W. Magee, Proceedings of the 26th Annual Conference on Mass Spectrometry, St. Louis, MO. 1978, p.207.

85. G. K. Wehner and P. W. Czandera, Methods of Surface Analysis, Elsevier, Amsterdam (1975) p. 5.

86. S. Hofmann, Appl. Phys. 9 (1976) 59.

87. J. Ferron and R. Vidal, Appl. Surface Science 27 (1986) 329.

88. D. Marton and J. Fine, Thin Solid Films 151 (1987) 433.

89. J. Fine and B. Navinsek, J. Vac. Sci. Technol. A (1985) 1408.

90. J. Fine and R. Gordon, J. Appl. Phys. 49 (1978) 1236.

91. K. Roll, W. Losch, and C. Achete, J. Appl. Phys. 50, 4422 (1979).

92. S. Hofmann and A. Zalar, Thin Solid Films 56, 337 (1979).

93. K. Roll, Appl. Surf. Sci 5, 388 (1980).

94. L. E. Rehn, S. Dannyluk, and H. Wiedersich, Phys. Rev. Lett. 43, 1437 (1979).

95. M. Shikata and R. Shimizu, Surf. Sci. 97, L363 (1980).

96. H. Shimizu, M. Ono, N. Koyama, and Y. Ishida, Jpn. J. Appl. Phys. 19, L567(1980).

97. P. S. Ho, Surf. Sci. 72, 253 (1978).

98. A. H. Eltoukhy and J. E. Greene, J. Appl. Phys. 51,444 (1980).

99. J. Fine, T. D. Andreadis, and F. Davarya, Nucl. Instrum. Methods 209/210, 521 (1983).

100. L. Tanovic, The Physics of Ionized Gases, Invited Lectures and Progress Reports, edited by M. Matic(Boris Kidric Institute, Belgrade, Yugoslavia, 1980), p. 485.

101. P. H. Holloway, R. S. Bhattacharya, Surface & Interf. Anal., 3 (1981) 119

102. P. Sigmund: Sputtering by Ion Bombardment: Theoretical Concepts, in Sputtering by Particle Bombardment, I., ed. R. Behrisch, Springer, Berlin, 1981

103. Thin Film and Depth Profile Analysis, ed. H. Oechsner, Springer, Berlin, 1984.

104. J. Kirschner, H. W. Etzkorn, Top. Curr. Phys. 37 (1984) 103.

105. G. Ayrault, R. S. Averback, D. N. Seidman, Scripta Metallurgica, 12 (1978) 119

106. D. S. Karpuzov, J. S. Colligon, H. Kheyrandish, A. E. Hill, Nucl. Instr. & Meth. in Phys. Res., B6 (1985) 474

107. S. Matteson, Appl. Surface Sci., 9 (1981) 335

108. R. Collins, 3d Conf. on Radiation Effects in Insulators, Guilford, Surrey, England, July, 1985.

109. G. Carter, R. Collins, D. A. Thompson, Radiation Eff., 55 (1981) 99

110. G. J. Dienes, A. C. Damask, J. of Appl. Phys. , 29 (1958) 1713)

111. L. Winters and J. Coburn, Appl. Phys. Lett. 28, (1976) 176.

112. Chou and Shafer, Surface Science, 92 (1980) 601.

113. Y. T. Cheng, X. A. Zhao, T. Banwell, T. W. Workman, M. A. Nicolet, and W. L. Johnson, J. Appl. Phys. 60 (7), 1986 2615.

114. D. S. Karpuzov, D. G. Armour, J. Phys. D17 (1984) 853 (31)

115. R. R. Hart, H. L. Dunlap, O. J. Marsh, J. Appl. Phys., 46 (1975) 1947

116. J. E. Hobbs, A. D. Marwick, Radiation Eff. Lett., 58 (1981) 83

117. J. E. Hobbs, A. D. Marwick, Nucl. Instr. & Meth. in Phys. Res., B9 (1985)

118. L. Kornbilt, A. R. Zomorrodian, S. Tougaard, A. Ignatiev, Rad. Effects 91 (1985) 97

119. W. Vandervorst, F. R. Shepherd, M. L. Swanson, H. H. Plattner, O. M. Westcott, I. V. Mitchell, Nucl. Instr. & Meth. in Phys. Res., B15 (1986) 183

120. E. L. Church, H. A. Jenkinson , J. M. Zavada, Optical Eng. 16 (1977) 360

121. H.H. Andersen, H. L. Bay: Sputtering Yield Measurements, in Sputtering by Particle Bombardment, I., ed. R. Behrisch, Springer, Berlin, 1981, pp. 175, 182

122. P.G. Shewmon, Diffusion in Solids, McGraw-Hill, New York, 1963.

123. J. C. Ashley, C.J. Tung, Surface & Interf. Anal, 4 (1982) 52

124. Constitution of Binary Alloys, ed. M. Hansen, 2nd ed. K. Anderkok, McGraw-Hill, New York, 1958

125. A. B. Vladimirov, V. N. Kaygorodov, S. M. Klotsman, I. Sh.

Trakhtenberg, Fiz. Metal. Metalloved. 45 (1978) 1015
(English Transl.: Phys. Met. Metall. 45 (1979) 100)

126. J. Bardeen and C. Herring, Atom Movements, pp. 87-111
American Society for Metals, Cleveland, 1951.

127. A. Vehanen, J. Makinen, P. Hautojarvi, H. Huomo, J.
Lahtinen, R. M. Nieminen, S. Valkealahti, Phys. Res. B32
(1985) 7561

128. M. Kuhlein and I. Jaegar, Surface and Interface Analysis, 6
(1984) 129.